
Performance of Grouted Connections for Prefabricated Bridge Deck Elements

Publication FHWA-HIF-19-003

November 2018

Research, Development, and Technology
Turner-Fairbank Highway Research Center
6300 Georgetown Pike
McLean, VA 22101-2296



U.S. Department
of Transportation

**Federal Highway
Administration**

FOREWARD

Transportation agencies face a number of challenges when it comes to the design, construction, and maintenance of highway infrastructure networks. Thus, solutions that reduce the impact of new and replacement bridge construction on the owner, traveling public, and environment are greatly sought after. This is especially true for those solutions that also enhanced durability and resiliency of bridge structure. A recent paradigm shift in bridge construction, termed “accelerated bridge construction” or “ABC,” utilizes innovative strategies, technologies, and design concepts to reduce the impact of bridge construction. Many of these ABC projects use prefabricated bridge elements and systems (PBES) to realize of the aforementioned benefits. These modular systems are manufactured off-site with high-quality material and are rapidly assembled on-site to form structural systems. Although these systems provide numerous benefits, connecting elements together poses a challenge. The goal of the research presented in this report was to advance the body of knowledge on behavior of connections between prefabricated bridge elements and systems. The research team executed an extensive study, investigating many different variable combinations. The information and findings presented aim to enhance the understanding of these systems such that bridge owners and design consultants can better implement PBES-based solutions.

Cheryl Allen Richter, P.E., Ph.D.
Director, Office of Infrastructure
Research and Development

Notice

This document is disseminated under the sponsorship of the U.S. Department of Transportation in the interest of information exchange. The U.S. Government assumes no liability for the use of the information contained in this document.

The U.S. Government does not endorse products or manufacturers. Trademarks or manufacturers’ names appear in this report only because they are considered essential to the objective of the document.

Quality Assurance Statement

The FHWA provides high-quality information to serve Government, industry, and the public in a manner that promotes public understanding. Standards and policies are used to ensure and maximize the quality, objectivity, utility, and integrity of its information. FHWA periodically reviews quality issues and adjusts its programs and processes to ensure continuous quality improvement.

TECHNICAL REPORT DOCUMENTATION PAGE

1. Report No. FHWA-HIF-19-003	2. Government Accession No.	3. Recipient's Catalog No.	
4. Title and Subtitle Performance of Grouted Connections for Prefabricated Bridge Deck Elements		5. Report Date November 2018	
		6. Performing Organization Code:	
7. Author(s) Zachary B. Haber and Benjamin A. Graybeal		8. Performing Organization Report No.	
9. Performing Organization Name and Address Office of Infrastructure Research and Development Federal Highway Administration 6300 Georgetown Pike McLean, VA 22101-2296		10. Work Unit No.	
		11. Contract or Grant No.	
12. Sponsoring Agency Name and Address Office of Infrastructure Research and Development Federal Highway Administration 6300 Georgetown Pike McLean, VA 22101-2296		13. Type of Report and Period Covered January 2011 – December 2016	
		14. Sponsoring Agency Code HRDI-40	
15. Supplementary Notes The completion of the research discussed herein was supported by laboratory support contract DTFH61-10-D-00017 at the Turner-Fairbank Highway Research Center.			
16. Abstract Prefabricated bridge elements and systems (PBES) are integral to many accelerated bridge construction projects, and prefabricated deck panels are one of many PBES types that have gained popularity in such projects. Laboratory research and field studies have indicated the primary challenge for these systems is the design and construction of the connections, which are typically made using interlaced connector elements and field-cast grout. Poor detailing and design considerations have been shown to pose problems with deck durability, serviceability, and ultimate capacity. The objective of the research presented herein was to advance the understanding of deck-level connections between adjacent prefabricated bridge deck elements for use in accelerated bridge construction projects. Two series of experiments were conducted. The first, referred to as "Bond Characterization Testing," utilized specimens with geometric details and loading protocols based on current ASTM standard test methods. These tests were used to study the bond behavior between precast concrete and different connection grouts. In the second set of experiments, referred to as "Deck-Level Connection Testing," 75 large-scale deck-level connection assemblies were tested in four-point bending and subjected to three different loading protocols; namely, low-level cyclic loading meant to induce cracking, post-cracking fatigue loading, and monotonic ultimate loading. Several parameters frequently considered during the design of these connections were investigated: shear key shape, reinforcement type, connection grout material type, and precast surface preparation. Results indicate the performance of these connections is heavily influenced by the grout type, precast concrete surface preparation, and reinforcement detailing.			
17. Key Words Ultra-high performance concrete, Non-shrink grout, epoxy grout, rapid-set grout, connections, precast bridge deck, accelerated bridge construction		18. Distribution Statement No restrictions.	
19. Security Classif. (of this report) Unclassified	20. Security Classif. (of this page) Unclassified	21. No. of Pages 156	22. Price N/A

SI* (MODERN METRIC) CONVERSION FACTORS

APPROXIMATE CONVERSIONS TO SI UNITS

Symbol	When You Know	Multiply By	To Find	Symbol
LENGTH				
in	inches	25.4	millimeters	mm
ft	feet	0.305	meters	m
yd	yards	0.914	meters	m
mi	miles	1.61	kilometers	km
AREA				
in ²	square inches	645.2	square millimeters	mm ²
ft ²	square feet	0.093	square meters	m ²
yd ²	square yard	0.836	square meters	m ²
ac	acres	0.405	hectares	ha
mi ²	square miles	2.59	square kilometers	km ²
VOLUME				
fl oz	fluid ounces	29.57	milliliters	mL
gal	gallons	3.785	liters	L
ft ³	cubic feet	0.028	cubic meters	m ³
yd ³	cubic yards	0.765	cubic meters	m ³
NOTE: volumes greater than 1000 L shall be shown in m ³				
MASS				
oz	ounces	28.35	grams	g
lb	pounds	0.454	kilograms	kg
T	short tons (2000 lb)	0.907	megagrams (or "metric ton")	Mg (or "t")
TEMPERATURE (exact degrees)				
°F	Fahrenheit	5 (F-32)/9 or (F-32)/1.8	Celsius	°C
ILLUMINATION				
fc	foot-candles	10.76	lux	lx
fl	foot-Lamberts	3.426	candela/m ²	cd/m ²
FORCE and PRESSURE or STRESS				
lbf	poundforce	4.45	newtons	N
lbf/in ²	poundforce per square inch	6.89	kilopascals	kPa

APPROXIMATE CONVERSIONS FROM SI UNITS

Symbol	When You Know	Multiply By	To Find	Symbol
LENGTH				
mm	millimeters	0.039	inches	in
m	meters	3.28	feet	ft
m	meters	1.09	yards	yd
km	kilometers	0.621	miles	mi
AREA				
mm ²	square millimeters	0.0016	square inches	in ²
m ²	square meters	10.764	square feet	ft ²
m ²	square meters	1.195	square yards	yd ²
ha	hectares	2.47	acres	ac
km ²	square kilometers	0.386	square miles	mi ²
VOLUME				
mL	milliliters	0.034	fluid ounces	fl oz
L	liters	0.264	gallons	gal
m ³	cubic meters	35.314	cubic feet	ft ³
m ³	cubic meters	1.307	cubic yards	yd ³
MASS				
g	grams	0.035	ounces	oz
kg	kilograms	2.202	pounds	lb
Mg (or "t")	megagrams (or "metric ton")	1.103	short tons (2000 lb)	T
TEMPERATURE (exact degrees)				
°C	Celsius	1.8C+32	Fahrenheit	°F
ILLUMINATION				
lx	lux	0.0929	foot-candles	fc
cd/m ²	candela/m ²	0.2919	foot-Lamberts	fl
FORCE and PRESSURE or STRESS				
N	newtons	0.225	poundforce	lbf
kPa	kilopascals	0.145	poundforce per square inch	lbf/in ²

*SI is the symbol for the International System of Units. Appropriate rounding should be made to comply with Section 4 of ASTM E380. (Revised March 2003)

TABLE OF CONTENTS

CHAPTER 1. INTRODUCTION	1
INTRODUCTION.....	1
OBJECTIVE.....	2
SUMMARY OF APPROACH.....	2
OUTLINE OF REPORT	3
CHAPTER 2. BACKGROUND AND PREVIOUS RESEARCH	4
INTRODUCTION.....	4
BACKGROUND ON PREFABRICATED DECK PANEL SYSTEMS.....	4
PREVIOUS RESEARCH	7
Reinforcement Configurations	7
Grout Material Selection	10
Shear Key Geometry	11
Precast Panel Surface Preparation	12
SUMMARY	13
CHAPTER 3. EXPERIMENTAL PROGRAM	14
INTRODUCTION.....	14
OVERVIEW OF TEST SPECIMENS AND VARIABLES.....	14
TEST VARIABLES	16
Field-Cast Grouts.....	16
Reinforcement Types and Detailing.....	19
Shear Key Surface Preparation.....	22
Shear Key Geometry	26
Transverse Reinforcement.....	26
SUMMARY OF TEST VARIABLE NOMENCLATURE	27
DECK-LEVEL CONNECTION SPECIMENS	29
Test Matrices	29
Design Details	32
Construction	35
Instrumentation.....	38
BOND CHARACTERIZATION TEST SPECIMENS.....	40

Test Matrix	40
Specimen Details	41
Construction	42
Instrumentation.....	44
CHAPTER 4. BOND CHARACTERIZATION TESTING.....	45
INTRODUCTION.....	45
TEST PROCEDURES	45
Flexure Beam Tests	45
Splitting Cylinder Tests.....	46
Slant Shear Tests	48
COMPRESSIVE PROPERTIES OF CONCRETE AND GROUT	48
TEST RESULTS	50
Flexure Tests	50
Splitting Cylinder Tests.....	56
Slant Shear Test.....	62
Comparison of Test Methods	68
Comparison of Test Methods	68
Overall Assessment and Key Observations.....	73
CHAPTER 5. DECK-LEVEL CONNECTION TEST RESULTS.....	75
INTRODUCTION.....	75
TEST PROCEDURES	75
Test Setup.....	75
Pre-Crack Cyclic Loading	76
Post-Cracking Fatigue Loading.....	78
Monotonic Ultimate Loading.....	79
PRE-TEST OBSERVATIONS	79
TEST RESULTS	82
Pre-Crack Cyclic Loading	82
Post-Cracking Fatigue Loading.....	98
Monotonic Ultimate Loading	111
CHAPTER 6. SUMMARY AND CONCLUSIONS.....	132

SUMMARY	132
KEY OBSERVATIONS	132
Bond Characterization Tests.....	132
Deck Panel Connection Tests.....	133
CONCLUSIONS.....	135
RECOMMENDATIONS	136
ACKNOWLEDGMENTS	137
REFERENCES.....	138

LIST OF FIGURES

Figure 1. Illustration. Typical section view of prefabricated, pre-tensioned concrete girders with integral bridge deck.	5
Figure 2. Illustration. Plan view of a bridge using prefabricated, pre-tensioned concrete girders with integral bridge deck.	6
Figure 3. Illustration. Prefabricated bridge element with integral bridge deck.	6
Figure 4. Illustration. Concrete girders with prefabricated full-depth deck panels.	7
Figure 5. Illustration. U-Bar connection tested by Zhu, Ma and French (2012).	9
Figure 6. Illustration. One-layer headed bar connection tested by Li et al. (2010).	9
Figure 7. Illustration. Two-layer headed bar connection tested by Graybeal (2010).	9
Figure 8. Illustration. Straight bar connection tested by Graybeal (2010).	10
Figure 9. Illustration. 90-degree hooked bar connection tested by Azizinamini et al. (2014).	10
Figure 10. Illustration. Shear key configurations.	11
Figure 11. Illustration. Common female-to-female shear key shapes.	12
Figure 12. Illustration. Deck-level connection specimens and test variables.	15
Figure 13. Illustration. Bond characterization specimens and test variables.	16
Figure 14. Photo. Black reinforcing bar; Denoted by “B.”	19
Figure 15. Photo. Epoxy-coated reinforcing bar; Denoted by “E.”	19
Figure 16. Photo. GFRP reinforcing bar; Denoted by “G.”	19
Figure 17. Photo. Headed reinforcing bar; Denoted by “H.”	20
Figure 18. Photo. Black U-shaped reinforcing bar; Denoted by “UB.”	20
Figure 19. Photos. Non-contact lap splice details investigated.	21
Figure 20. Graph. Measured axial stress-strain behavior of reinforcing bars.	22
Figure 21. Photo. Pressure washing procedure.	23
Figure 22. Photo. Final pressure wash surface preparation.	23
Figure 23. Photo. Sand blasting procedure.	24
Figure 24. Photo. Final sand blasted surface preparation.	24
Figure 25. Photo. In-form retarder used on specimen formwork.	25
Figure 26. Photo. Final exposed aggregate surface preparation.	25
Figure 27. Illustration. Shear key details.	26
Figure 28. Photos. Examples of transverse reinforcement used in the connection region.	27
Figure 29. Illustration. Details of monolithic specimens with continuous bars.	33
Figure 30. Illustration. Details of monolithic specimens with lap spliced bars.	34
Figure 31. Illustration. Details of precast specimens with lap spliced bars.	35
Figure 32. Photo. Deck panel formwork ready for concrete.	36
Figure 33. Photo. Placement of individual deck panels.	37
Figure 34. Photo. Connection region ready for grouting.	37
Figure 35. Photo. Grout placement into a connection region.	38
Figure 36. Photo. Specimens with completed connections.	38
Figure 37. Illustration. Instrumentation plan for deck-level connection tests (excluding U-bar tests).	39

Figure 38. Illustration. Instrumentation plan for deck-level connection specimens employing U-bars.....	40
Figure 39. Illustration. Flexural beam bond test specimen details.....	41
Figure 40. Illustration. Splitting cylinder bond test specimen details.....	42
Figure 41. Illustration. Slant shear bond test specimen details.....	42
Figure 42. Photo. Formwork for flexural beam bond test specimens.....	43
Figure 43. Photo. Formwork for splitting cylinder bond test specimens.....	43
Figure 44. Photo. Formwork for slant shear bond test specimens.....	44
Figure 45. Photo. Bond characterization specimens prepared for grout placement.....	44
Figure 46. Photo. Flexural beam bond testing (based on ASTM C78).....	46
Figure 47. Equation. Loading rate equation for flexural beam bond testing.....	46
Figure 48. Photo. Splitting cylinder bond testing (based on ASTM C496) prior to specimen alignment.....	47
Figure 49. Equation. Loading rate equation for splitting cylinder tests.....	47
Figure 50. Photo. Slant shear bond testing (Based on ASTM C882).....	48
Figure 51. Photo. Failure of flexural beam bond test specimens: Mode 1 – bond failure.....	51
Figure 52. Photo. Failure of flexural beam bond test specimens: Mode 2 – partial substrate failure.....	51
Figure 53. Photo. Failure of flexural beam bond test specimens: Mode 3 – substrate/grout failure.....	52
Figure 54. Equation. Flexural tension strength as determined by third-point loading.....	53
Figure 55. Graph. Average tensile strength flexural beam bond tests with G1 grout.....	54
Figure 56. Graph. Average tensile strength flexural beam bond tests with M1 grout.....	54
Figure 57. Graph. Average tensile strength flexural beam bond tests with E1 grout.....	55
Figure 58. Graph. Average tensile strength flexural beam bond tests with U2 grout.....	55
Figure 59. Graph. Average tensile strength from flexural beam bond tests with epoxy bonding agents using U2 grout.....	56
Figure 60. Photo. Failure of splitting cylinder bond test specimens: Mode 1 – bond failure.....	57
Figure 61. Photo. Failure of splitting cylinder bond test specimens: Mode 2 – partial substrate failure.....	57
Figure 62. Photo. Failure of splitting cylinder bond test specimens: Mode 3 – substrate/grout failure.....	58
Figure 63. Equation. Splitting tensile strength.....	59
Figure 64. Graph. Average tensile strength from splitting cylinder bond tests with G1 grout.....	59
Figure 65. Graph. Average tensile strength from splitting cylinder bond tests with M1 grout.....	60
Figure 66. Graph. Average tensile strength from splitting cylinder bond tests with E1 grout.....	60
Figure 67. Graph. Average tensile strength from splitting cylinder bond tests with U2 grout.....	61
Figure 68. Graph. Average splitting tensile strength from splitting cylinder bond tests with epoxy bonding agents.....	62
Figure 69. Photo. Failure of slant shear bond test specimens: Mode 1 – bond failure.....	62
Figure 70. Photo. Failure of slant shear bond test specimens: Mode 2 – partial substrate failure.....	63
Figure 71. Photo. Failure of slant shear bond test specimens: Mode 3 – substrate failure.....	63

Figure 72. Photo. Failure of slant shear bond test specimens: Mode 4 – concrete crushing.	64
Figure 73. Equation. Slant shear bond strength.	65
Figure 74. Graph. Average shear stress at failure for slant shear bond tests with G1 grout.	65
Figure 75. Graph. Average shear stress at failure for slant shear bond tests with M1 grout.	66
Figure 76. Graph. Average shear stress at failure for slant shear bond tests with E1 grout.	66
Figure 77. Graph. Average shear stress at failure for slant shear bond tests with U2 grout.	67
Figure 78. Graph. Average shear strength from slant shear bond tests with epoxy bonding agents.	67
Figure 79. Graph. Coefficient of variation for flexural beam bond tests.	68
Figure 80. Graph. Coefficient of variation for splitting cylinder bond tests.	69
Figure 81. Graph. Coefficient of variation for slant shear bond tests.	69
Figure 82. Illustration. Splitting cylinder bond test finite-element model and material properties.	70
Figure 83. Illustration. Finite-element results for splitting cylinder test with different material properties.	71
Figure 84. Illustration. Shear friction effects in slant shear bond testing.	72
Figure 85. Graph. Comparison between splitting cylinder and flexural beam tensile bond tests.	73
Figure 86. Illustration. Deck panel test set-up.	75
Figure 87. Photo. Deck panel specimen during loading.	76
Figure 88. Illustration. Pre-cracking cyclic loading protocol (1 kip = 4.448 kN).	77
Figure 89. Equation. Cracking moment as define by AASHTO (2010).	77
Figure 90. Equation. Modulus of rupture for normal-weight concrete as defined by AASTHO (2010).	77
Figure 91. Illustration. Post-cracking fatigue loading protocol.	79
Figure 92. Equation. Constant amplitude fatigue threshold defined by AASHTO (2014).	79
Figure 93. Graph. Observed shrinkage cracking in connection grout.	80
Figure 94. Photo. Representative photo of shrinkage cracking in specimens with G1 grout; specimen G1-8.5-UB-EA-Tr-T-73 shown.	81
Figure 95. Photo. Representative photo of the specimens with G1 grout and internal curing; specimen G1IC-8.5-UB-EA-Tr-T-74 shown.	81
Figure 96. Photo. Representative photo of shrinkage cracking in specimens with U2 grout.	82
Figure 97. Graph. Observed interface cracking at different cracking cycle load levels for specimens with the pressure washed surface preparation.	83
Figure 98. Graph. Observed interface cracking at different cracking cycle load levels for specimens with the sand blasted surface preparation.	84
Figure 99. Graph. Observed interface cracking at different cracking cycle load levels for specimens with the exposed aggregate surface preparation.	84
Figure 100. Graph. Observed interface cracking at different cracking cycle load levels for specimens with PW or SB preparation and epoxy bonding agents.	85
Figure 101. Illustration. Damage progression during pre-cracking cyclic loading for specimen G1-8.5-UB-EA-Tr-T-73.	86

Figure 102. Illustration. Damage progression during pre-cracking cyclic loading for specimen G1IC-8.5-UB-EA-Tr-T-74.	87
Figure 103. Illustration. Damage progression during pre-cracking cyclic loading for specimen U2-5.5-B-EA-Tr-75.	88
Figure 104. Photos. Representative photos of deck-level connection regions pre-cracking cyclic loading.	89
Figure 105. Photo. Specimen U2-5.5-B-EA-Tr-75 after cyclic crack loading.	90
Figure 106. Photos. Comparison between specimens with and without IC.	90
Figure 107. Equation. Change in tensile strain.	91
Figure 108. Graph. Example of early cracking behavior in specimen G1-12-B-PW-Tp (50).	92
Figure 109. Graph. Example of late cracking behavior in specimen U2-5.5-B-EA-Tr (16).	93
Figure 110. Equation. Normalized interface strain.	94
Figure 111. Graph. Normalized tensile strain response at the concrete-grout interface at $0.3M_{cr}$	95
Figure 112. Graph. Normalized tensile strain response at the concrete-grout interface at $0.5M_{cr}$	96
Figure 113. Graph. Normalized tensile strain response at the concrete-grout interface at $1.0M_{cr}$	97
Figure 114. Photos. Representative photos of fatigue failure of specimens with G1 grout.	100
Figure 115. Photo. Representative photo of deck-level connection specimen with G1 grout after completion of cyclic crack loading (Specimen G1-12-B-SB-Tp-34 shown).	101
Figure 116. Photo. Representative photo of deck-level connection specimen with G1 grout during fatigue loading (Specimen G1-12-B-SB-Tp-34 shown after 794,744 cycles). .	101
Figure 117. Photo. Representative photo of deck-level connection specimen with G1 grout after completion of fatigue loading (Specimen G1-12-B-SB-Tp-34 shown).	102
Figure 118. Graph. Relationship between number of overload cycles sustained and $f'c$ for specimen with G1 grout and 12-inch (305-mm) lap splice lengths.	103
Figure 119. Graph. Relationship between flexural stiffness and cycle number for specimens with U-bars; the graph only reflects data recorded during low-level cycles.	104
Figure 120. Photo. Representative photos of fatigue failure of specimens with M1 grout.	105
Figure 121. Graph. Relationship between number of overload cycles sustained and $f'c$ for specimen with M1 grout and 12-inch (305-mm) lap splice lengths.	106
Figure 122. Photo. Representative photo of deck-level connection specimen with E1 grout after completion of cyclic crack loading (Specimen E1-12-B-SB-Tr-36 shown).	107
Figure 123. Photo. Representative photo of deck-level connection specimen with E1 grout during fatigue loading (Specimen E1-12-B-SB-Tr-36 shown after 263,943 cycles).	107
Figure 124. Photo. Representative photo of deck-level connection specimen with E1 grout after completion of fatigue loading (Specimen E1-12-B-SB-Tr-36 shown).	108
Figure 125. Photo. Representative photo of deck-level connection specimen with U2 grout after completion of cyclic crack loading (Specimen U2-5.5-B-SB+E1-Tr-12 shown).	109

Figure 126. Photo. Representative photo of deck-level connection specimen with U2 grout during fatigue loading (Specimen U2-5.5-B-SB+E1-Tr-12 shown after 1,291,897 cycles).	110
Figure 127. Photo. Representative photo of deck-level connection specimen with U2 grout after completion of fatigue loading (Specimen U2-5.5-B-SB+E1-Tr-12 shown).	110
Figure 128. Graph. Relationship between flexural stiffness and cycle number for U2-5.5-B-EA-Tr-75 compared with specimens with U-bars; the graph only reflects data recorded during low-level cycles.	111
Figure 129. Equation. Definition of displacement ductility.	111
Figure 130. Graph. Force-displacement behavior of monolithic deck panels with mild steel bars.	113
Figure 131. Photos. Observed failure modes of monolithic deck panels with mild steel bars. ...	114
Figure 132. Graph. Force-displacement relationships from specimens with G1 grout and straight black bars.	115
Figure 133. Photo. Representative photo of the observed failure of specimens with G1 grout and straight black bars after ultimate loading.	116
Figure 134. Graph. Force-displacement relationships from specimens with G1 grout and headed bars.	117
Figure 135. Graph. Force-displacement relationships from specimens with G1 grout and U-bars.	118
Figure 136. Photo. Specimen G1-8.5-UB-EA-Tr-T-73 after ultimate loading.	118
Figure 137. Photo. Specimen G1IC-8.5-UB-EA-Tr-T-74 after ultimate loading.	119
Figure 138. Graph. Force-displacement relationships from specimens with E1 grout and black and epoxy-coated bars.	120
Figure 139. Photo. Observed failure of specimens with E1 grout and 5.5-inch (140-mm) splice lengths (Specimen E1-5.5-B-SB-Tp-63 shown).	121
Figure 140. Photo. Observed failure of specimens with E1 grout and 12-inch (305-mm) splice lengths.	121
Figure 141. Graph. Force-displacement relationships from specimens with E1 grout and headed bars.	122
Figure 142. Graph. Force-displacement relationships from specimens with U2 grout and black or epoxy-coated bars.	123
Figure 143. Photo. Representative photo of the observed failure of specimens with U2 grout after ultimate loading.	123
Figure 144. Graph. Force-displacement relationships from specimens with GFRP bars.	125
Figure 145. Photo. Failure of Monolithic-Continuous-G-67.	125
Figure 146. Photo. Failure of E1-12-G-SB-Tp-65.	126
Figure 147. Photos. Failure of U2-12-G-SB-Tp-61.	126
Figure 148. Equation. Normalized ultimate load.	127
Figure 149. Graph. Ultimate loads of deck-level connection specimens with G1 grout.	127
Figure 150. Graph. Ultimate loads of deck-level connection specimens with E1 grout.	128
Figure 151. Graph. Ultimate loads of deck-level connection specimens with U2 grout.	128

Figure 152. Equation. Normalized ultimate load. 129

Figure 153. Graph. Estimated displacement ductility of deck-level connection specimens with
G1 grout. 130

Figure 154. Graph. Estimated displacement ductility of deck-level connection specimens with E1
grout. 130

Figure 155. Graph. Estimated displacement ductility of deck-level connection specimens with
U2 grout. 131

LIST OF TABLES

Table 1. Selected manufacturer-reported properties.	18
Table 2. Batching details for cementitious grouts G1 and M1.	18
Table 3. Batching details for epoxy grout E1.	18
Table 4. Batching details for ultra-high performance concrete grout U2.	18
Table 5. Measured material properties of reinforcing bars.	22
Table 6. Summary of test variable nomenclature.	28
Table 7. Test matrix for monolithic specimens.	29
Table 8. Test matrix for specimens with G1 grout connections.	30
Table 9. Test matrix for specimens with M1 grout connections.	31
Table 10. Test matrix for specimens with E1 grout connections.	31
Table 11. Test matrix for specimens with U2 grout connections.	32
Table 12. Concrete mix design used for deck panel specimens.	36
Table 13. Specimen matrix for bond characterization tests.	41
Table 14. Measured compressive strength of concrete.	49
Table 15. Measured compressive strength of G1 grout.	49
Table 16. Measured compressive strength of M1 grout.	49
Table 17. Measured compressive strength of E1 grout.	50
Table 18. Measured compressive strength of U2 grout.	50
Table 19. Observed failure modes in flexural beam bond tests.	53
Table 20. Observed failure modes in splitting cylinder bond tests.	58
Table 21. Observed failure modes in slant-shear bond tests.	64
Table 22. Summary of specimens with G1 grout that failed during fatigue loading.	99
Table 23. Summary of specimens with M1 grout that failed during fatigue loading.	105

LIST OF ABBREVIATIONS

AASHTO	American Association of State Highway and Transportation Officials
ABC	Accelerated bridge construction
COV	Coefficient of variation
DBT	Deck bulb tee
DOT	Department of transportation
FHWA	Federal Highway Administration
GFRP	Glass fiber-reinforced polymer
IC	Internal curing
LVDT	Linear variable differential transducers
LWA	Lightweight aggregate
MOR	Modulus of rupture
PBE	Prefabricated bridge element
PBES	Prefabricated bridge elements and systems
w/s	Water-to-solids ratio
w/c	Water-to-cement ratio

CHAPTER 1. INTRODUCTION

INTRODUCTION

Accelerated bridge construction (ABC) has become increasingly popular for new bridges and for replacement/rehabilitation projects. ABC has numerous advantages, which include reduced traffic disruption, expedited project delivery, and increased work zone safety. In order to realize some of these advantages, prefabricated bridge elements and systems (PBES) are typically employed. Prefabricated reinforced concrete elements can be manufactured off site, in parallel with on-site construction tasks, and can have superior quality compared with cast-in-place concrete elements. Once delivered to the site, prefabricated elements can be rapidly assembled to form the bridge structure.

The performance of prefabricated bridge systems is greatly dependent on the design and detailing of connections between elements. Typically, elements are joined using field-cast grout (or cast-in-place concrete) placed over interlaced reinforcing bars or into ducts used to embed bars into adjacent elements. The selection of the connection grout and the detailing of the connection can have a significant impact on both the structural performance and long-term durability of the system. Further, if the reinforcement or geometric details of the prefabricated element or its connection are too complex, element construction and field installation can become difficult. This might delay the project and could compromise the integrity of the prefabricated system and its connection, which could also result in poor performance. Thus, constructable robust connection details are desirable. Although prefabricated systems have been used for many different types of bridge components, bridge decks have emerged as one of the more popular applications. A number of different prefabricated deck panel systems have been evaluated experimentally and deployed in the field. There are three primary connection types associated with prefabricated deck systems. The first is the connection between the prefabricated deck element and the supporting girders, which is typically made using girder shear connectors grouted into pockets or seams. The second is the connection between adjacent prefabricated deck elements, which is commonly made using interlaced reinforcing bars and field-cast grout. Herein, this type of connection is referred to as a “deck-level” connection; it is the primary focus of this report. The third is a post-tensioned system, which utilizes post-tensioning tendons to connect and pre-compress precast panel elements to minimize cracking.

Deck-level connections commonly employ straight, hooked, or headed non-contact lap-spliced bars. These connections have become popular because they are easy to fabricate at the precasting yard and can be rapidly assembled with relatively minimal on-site detailing compared with conventional cast-in-place construction. Although fabrication and construction of this type of connection may be straightforward, there are a number of design considerations that can have a significant impact on the long-term performance of the connection. Some of these design considerations include selection of the reinforcement details between adjacent prefabricated deck

panels, selection of the field-cast grout that is used to fill the connection seam, and the geometry and detailing of precast concrete shear keys. Although a number of studies have been conducted to investigate how these different design considerations affect performance, most studies have considered only a limited number of variable combinations or have focused only on certain aspects of deck-level connection performance. Given the current demand for PBES technology, further investigation of these types of connections is warranted.

OBJECTIVE

The objective of this research was to advance the understanding of deck-level connections for prefabricated bridge decks. The research investigated deck-level connections employing interlaced reinforcing bars with different grout materials and different precast panel details for potential use in accelerated bridge construction projects.

SUMMARY OF APPROACH

The research discussed herein focused on assessing the structural performance of deck-level connections employing different closure grouts in combination with different connection details. Specific focus points included bond strength between precast concrete and the connection grout, the connection's resistance to cracking, behavior under fatigue loading, and behavior under monotonic ultimate loading.

The research team began by reviewing relevant literature to determine promising grout materials for field-cast connections as well as different precast panel details currently being deployed in precast deck systems. The research team then created test matrix of grout materials and different connection detail combinations. To achieve the objective, the experimental program was separated into two different phases that were conducted concurrently.

The first phase, Bond Characterization Testing, utilized small-scale specimens with geometric details and loading protocols based on currently available ASTM standard test methods. Three different test methods were used to study the bond behavior between precast concrete and connection grout: a flexural beam (modified from ASTM C78), a splitting cylinder (modified from ASTM C496), and a slant shear cylinder (modified from ASTM C882). Bond characterization tests investigated how bond behavior was affected by different combinations of grout materials and precast concrete surface preparations. A secondary objective of these tests was to investigate the applicability of each test method for evaluating the tensile strength of the grout-to-precast concrete bond.

In the second phase of the program, Deck-Level Connection Testing, 75 large-scale deck-level connection assemblies were tested in four-point bending and subjected to three different loading protocols. Deck panel specimens were 28 inches (711 mm) wide and 6 inches (152 mm) thick and were designed to simulate a portion of a bridge deck. The length of specimens varied slightly

depending on connection detailing. The average specimen length was 107 inches (2718 mm). Panels were first subjected to low-level cyclic loading to evaluate the crack resistance of the connection region. Panels were subsequently subjected to at least two million cycles of fatigue loading at a higher stress range to evaluate the potential for crack propagation, damage accumulation, or premature failure in the connection. Finally, after completion of fatigue loading, specimens were loaded monotonically to failure. The three loading protocols enabled assessment of the connection parameters as they related to durability, serviceability, and ultimate strength.

OUTLINE OF REPORT

This report is divided into six chapters. Chapters 1 and 2 provide an introduction and literature review, respectively. Chapter 3 presents the details of the experimental program. Chapters 4 and 5 present analysis and discussion of the results from bond characterization tests and large-scale deck panel testing, respectively. Chapter 6 presents a summary of the work conducted, the key observations, and the conclusions. Supplemental information related to specific test results can be obtained by contacting the research team.

CHAPTER 2. BACKGROUND AND PREVIOUS RESEARCH

INTRODUCTION

This chapter provides background information relevant to the focus of the research effort. The first section presents a brief background on prefabricated deck panel systems. The next section describes early applications of prefabricated deck panel systems and provides a general overview of the prefabricated deck panel system types that are relevant to the study presented herein; namely, those that employ deck-level connections. In the context of this report, a deck-level connection is defined as a connection between two adjacent prefabricated bridge deck elements that does not occur over a girder element; that is, there are no shear connectors present within the connection region. A deck-level connection is typically found between girders in integral deck girder systems and in longitudinal and transverse seams between prefabricated deck panels. The final section presents a review of relevant research studies. The review focuses on aspects of deck-to-deck connections that are considered in this research effort.

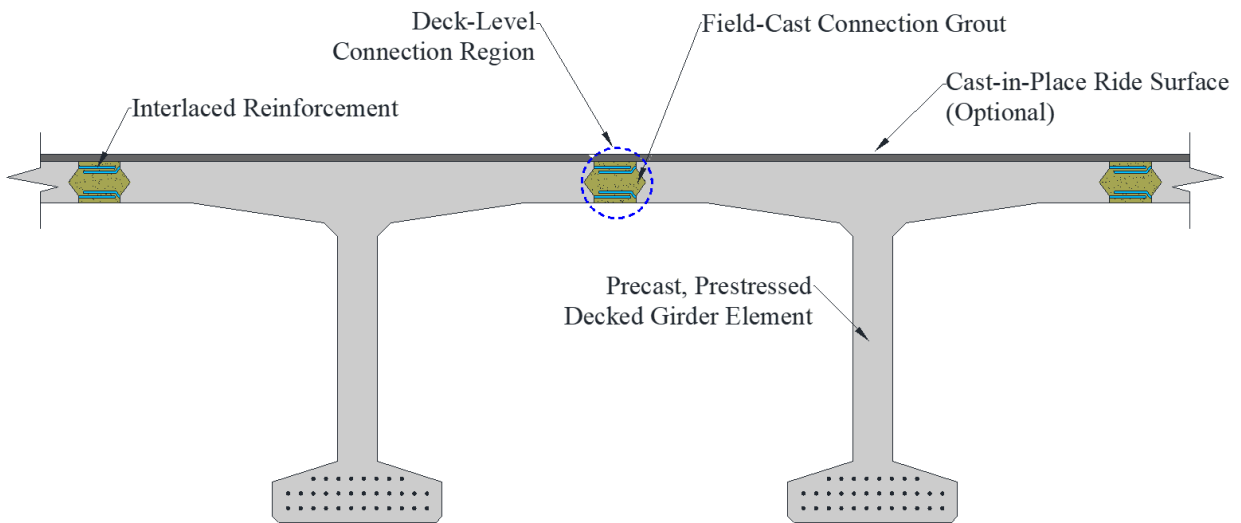
BACKGROUND ON PREFABRICATED DECK PANEL SYSTEMS

Prefabricated bridge deck elements have been used to accelerate construction since the 1970s. (Biswas 1986) Early deployments were predominately used in deck replacement projects when expedited project delivery was required to reduce interference with local traffic in densely populated regions. (Biswas 1986) Prefabricated bridge deck systems have since been studied extensively in both laboratory investigations and field inspection studies. The literature indicates that there are three primary types of prefabricated bridge deck systems: integral deck girder systems, partial-depth deck panel systems, and full-depth deck panel systems. Integral deck girder systems and full-depth deck panel systems are briefly described herein because they commonly employ the deck-level connection, which is the focus of this report.

Integral deck girders systems, which can include steel or concrete girders, typically have single or double T-shaped or box-shaped cross sections. In any case, the top flange of the girder provides resistance against compression forces generated when the superstructure is bending, and it also serves as the bridge deck. Although not required, a cast-in-place wearing surface is sometimes applied to provide a smoother riding surface and/or to profile the superstructure. An example of a prefabricated T-shaped concrete girder with an integral deck is shown in figure 1; this is otherwise referred to as a deck bulb tee (DBT) girder. Adjacent girders are typically connected using grout filled shear keys (shown in figure 1), mechanical fasteners, and/or transverse post-tensioning depending on the design. This type of construction is advantageous because it eliminates the need to erect the girders and place the bridge deck separately. Longitudinal connections between adjacent elements are typically continuous along the length of the span. This is illustrated in the plan-view drawing shown in figure 2.

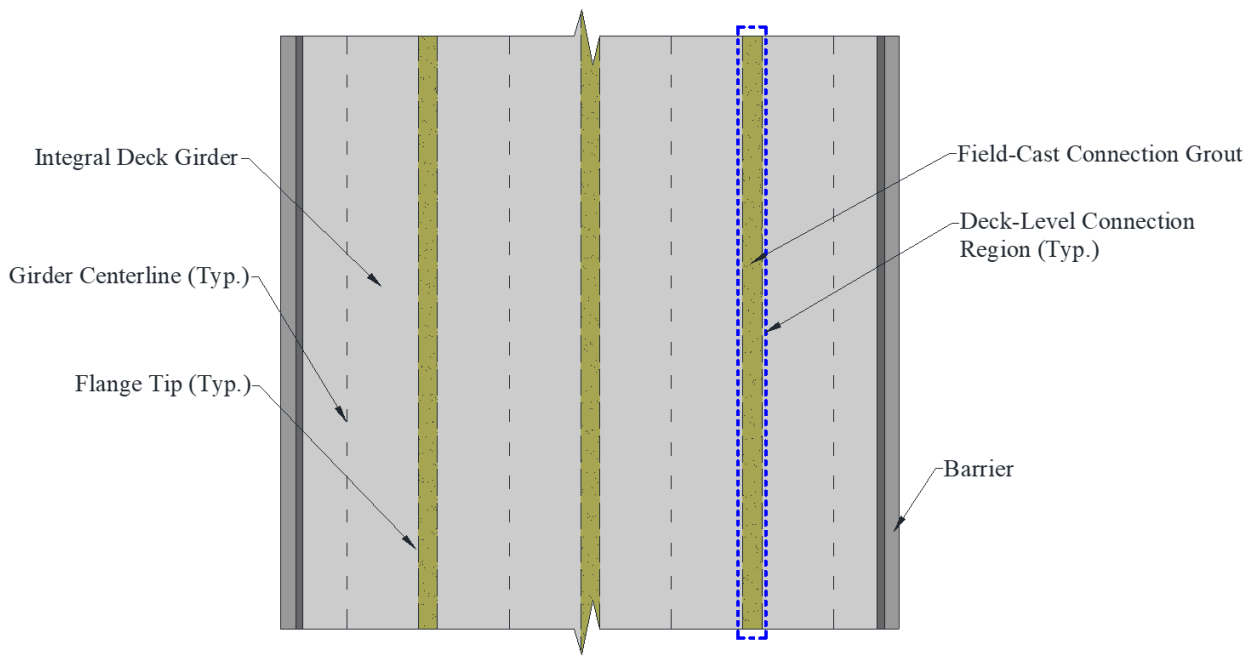
Another example of an integral deck system is shown in figure 3. In this case, the deck has been cast atop two steel I-shaped plate girders. The deck and girder assembly comprise a single prefabricated bridge element (PBE); this system is otherwise referred to as a modular superstructure unit. Similar to the example shown in figure 1, adjacent elements can be connected using grout-filled shear keys, mechanical fasteners, and/or transverse post-tensioning depending on the design. Furthermore, longitudinal connections between adjacent elements are typically continuous along the length of the span (similar to that shown in figure 2). In this case, the elements are shown to be connected using interlaced reinforcing bars and field-cast grout.

Full-depth deck panels are a type of prefabricated deck system where the entire depth of the bridge deck is precast. An example of this type of system is shown in figure 4. The most common type of connection between adjacent panels is a grouted, female-female shear key connection that is post-tensioned or reinforced with mild steel. (Sullivan 2007) Panels are typically connected to the girders using grouted pockets or longitudinal seam connections to develop composite action. Leveling bolts or shims are typically used to level the panels and provide proper haunch height. Full-depth panels do not require a wearing surface, but one can be applied to provide a smoother riding surface if the surface is rough due to the grouted connections, shear pockets, and misalignment between panels.



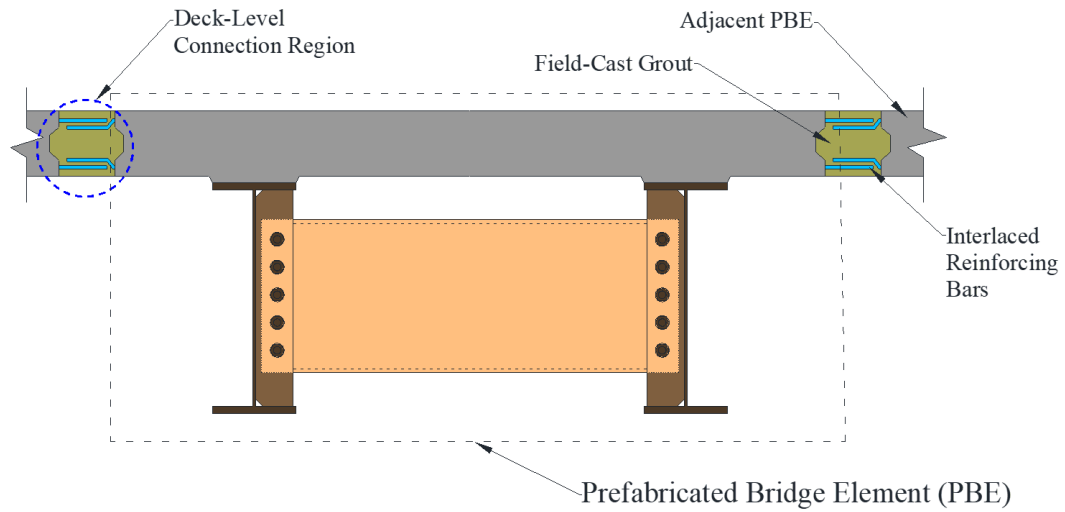
Source: FHWA

Figure 1. Illustration. Typical section view of prefabricated, pre-tensioned concrete girders with integral bridge deck.



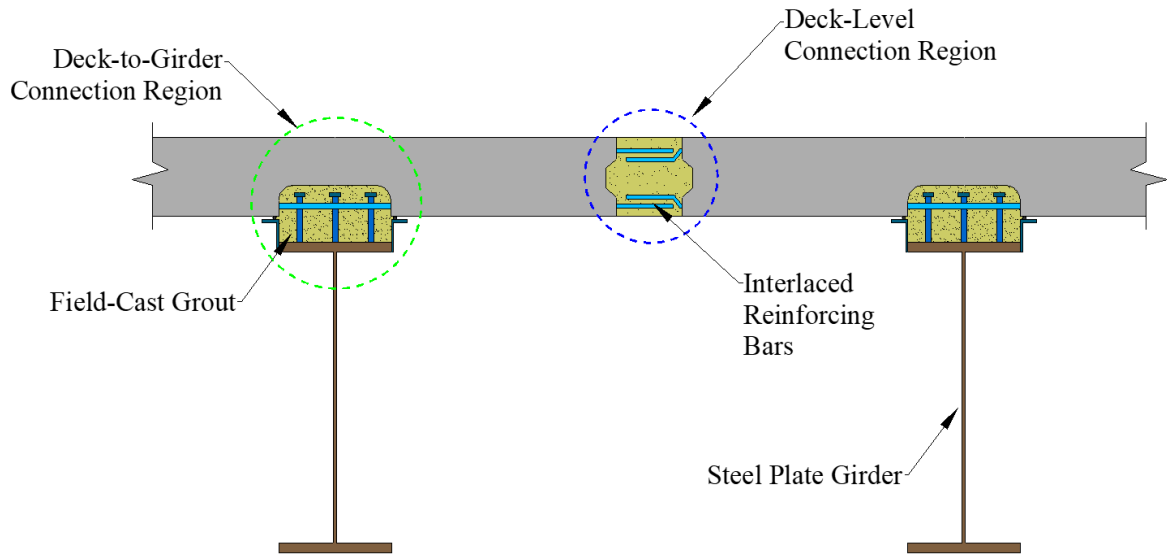
Source: FHWA

Figure 2. Illustration. Plan view of a bridge using prefabricated, pre-tensioned concrete girders with integral bridge deck.



Source: FHWA

Figure 3. Illustration. Prefabricated bridge element with integral bridge deck.



Source: FHWA

Figure 4. Illustration. Concrete girders with prefabricated full-depth deck panels.

PREVIOUS RESEARCH

Although a number of different deck-level connection schemes exist, there is some commonality among the designs. These connections typically have the following design considerations: selection of a reinforcement scheme for resisting applied loads, selection of a field-cast grout material for protecting the reinforcement and load-path continuity, and selection of a shear keyway shape and surface preparation. The following sections discuss previous research about these different aspects of deck-level connections for prefabricated bridge deck systems. Each section represents a test variable category that will be investigated in this study.

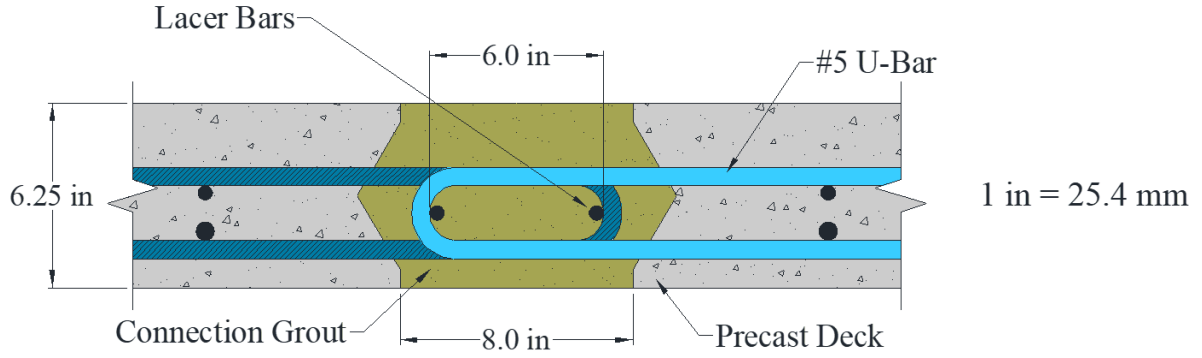
Reinforcement Configurations

The reinforcement in deck-level connections provides structural continuity between prefabricated elements, but it also must resist or arrest cracking due to shrinkage and temperature effects. The ideal connection would be simple to fabricate, constructible in the field, and able to provide durability and strength comparable to, if not better than, a monolithically-cast concrete deck.

Some early connection details did not employ reinforcing bars or post-tensioning tendons across the joint. Instead, connections used non-grouted, match-cast male-to-female shear keys, grouted female-to-female shear keys, or intermittent welded steel plates. (Badie and Tadros 2008; Li et al. 2010) Although some of these systems performed well, there have been accounts of joint cracking and leakage. (Martin and Osborn 1983; Stanton and Mattock 1986) Thus, providing reinforcement or intermittent post-tensioning across the joint has become common practice.

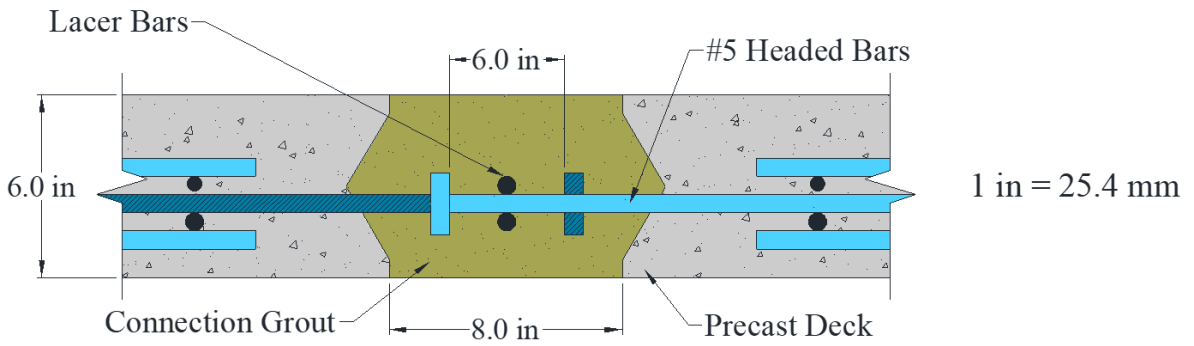
There have been a number of different reinforcement schemes devised, tested, and implemented for deck-level connections. Figure 5 through figure 9 illustrate some deck-level connections that have been previously investigated and/or deployed in the field. Each of the connection details shown were successful in developing the full moment capacity of the deck depending on the spacing of the bars, lap-splice length (or anchorage mechanism), and grout material selection. The primary differences among the connections are related to meeting reinforcement spacing and cover requirements, ease of fabrication, and constructability. For example, the detail tested by Zhu, Ma, and French (2012) shown in figure 5 was proposed for bridges with DBT superstructures. Typically, in DBT systems, the thickness of the deck is limited to 6 inches (152 mm) to reduce element weight. To meet cover requirements, a tighter, non-standard bend diameter was used. Li et al. (2010) reported that a survey of bridge engineering professionals indicated some concern with this approach. Furthermore, constructability becomes challenging when hooked bars are used in combination with reinforcement running the length of the connection (these are referred to as “lacer” bars).

A non-contact lap splice using straight bars is an advantageous connection detail from a fabrication, installation, and cost standpoint. However, a long lap splice length may be required to fully develop the tensile capacity of the reinforcement. Furthermore, the required lap splice length is highly dependent on the mechanical properties of the connection grout. To minimize the connection width, Graybeal (2010) used ultra-high performance concrete (UHPC) as a closure grout (detail shown in figure 8). UHPC is a relatively new class of fiber-reinforced cementitious composite materials that exhibit superior compressive, tensile, and durability behaviors compared with regular and high performance concretes. The tensile capacity of mild steel reinforcing bars embedded in UHPC can be fully developed over short lengths compared with bars embedded in conventional concrete. (Yuan and Graybeal 2015; Haber and Graybeal 2018) Other, more conventional grout materials have been shown to work if additional confinement over the lap-spliced region can be provided or if hooked or headed bars are used. (M. Keith Thompson et al. 2006; Badie and Tadros 2008; Li et al. 2010; Zhu et al. 2012; Zhu, Ma, and French 2012) It should be noted that depending on the configuration of the bars and the depth of the deck panel, headed or hooked bars might result in issues with cover requirements and can congest the connection region, resulting in fabrication challenges.



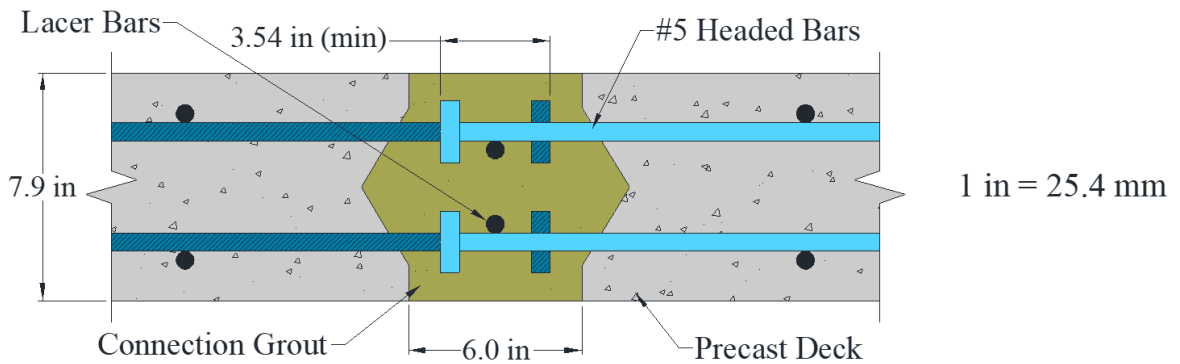
Source: FHWA

Figure 5. Illustration. U-Bar connection tested by Zhu, Ma and French (2012).



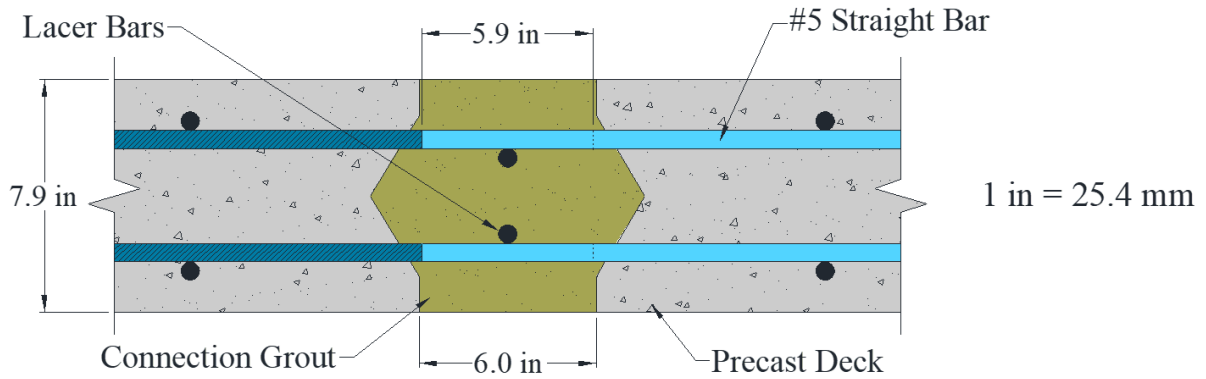
Source: FHWA

Figure 6. Illustration. One-layer headed bar connection tested by Li et al. (2010).



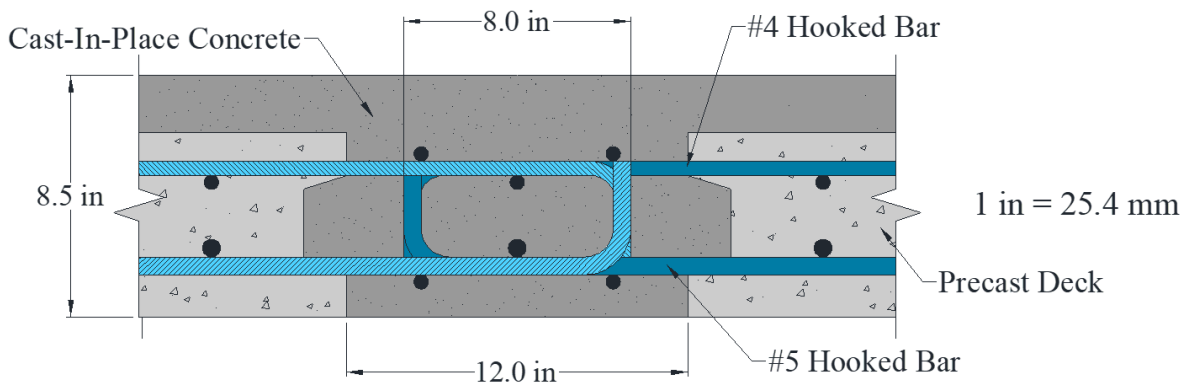
Source: FHWA

Figure 7. Illustration. Two-layer headed bar connection tested by Graybeal (2010).



Source: FHWA

Figure 8. Illustration. Straight bar connection tested by Graybeal (2010).



Source: FHWA

Figure 9. Illustration. 90-degree hooked bar connection tested by Azizinamini et al. (2014).

Grout Material Selection

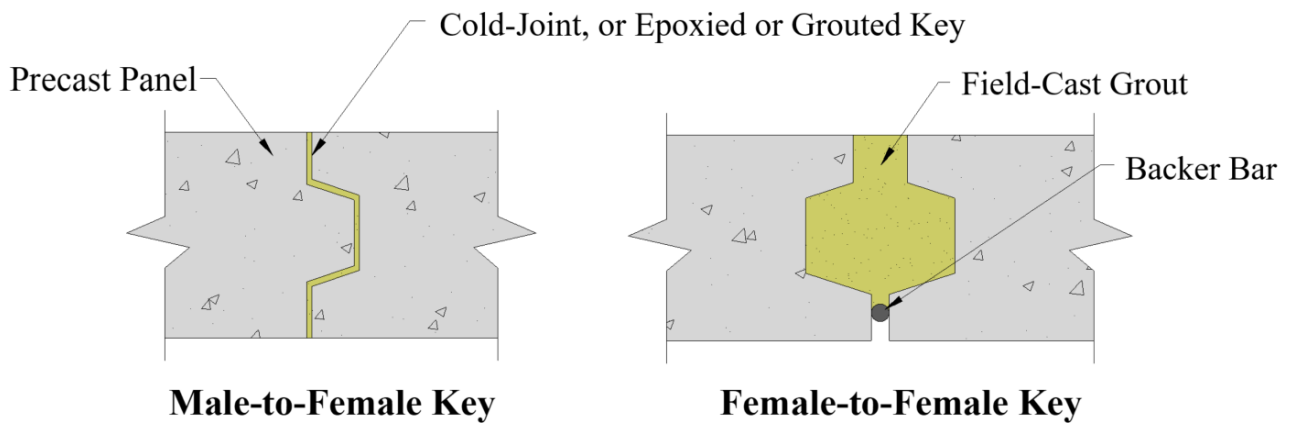
A wide variety of commercially available grouts have been tested for use in field-cast connections. The ideal material is dimensionally stable, gains strength quickly, has good workability, bonds well to precast concrete, and has good durability characteristics. The primary role of grout in the connection is to transfer loads between panels. Nevertheless, the secondary roles of the grout material are equally as important, which include protecting the connection reinforcement from contaminant ingress and providing a good bond with precast concrete. Common closure grout materials include non-shrink cementitious grouts, epoxy grouts, polymer modified grouts, fiber-reinforced grouts, magnesium phosphate grouts, ultra-high performance concrete, and others. One of the primary challenges associated with selecting a closure grout material is that there is no unified, industry-accepted performance criteria. (Zhu and Ma 2010) Previous research on grout materials for precast connection applications has focused mainly on bond strength to precast concrete, dimensional stability, fresh properties, constructability aspects,

and durability. (Gulyas, Wirthlin, and Champa 1995; Abu-Tair, Rigden, and Burley 1996; Issa et al. 2003; Swenty and Graybeal 2013; Igor De la Varga and Graybeal 2015) There has been very little research conducted on the effect of grout type on connection-level performance.

Shear Key Geometry

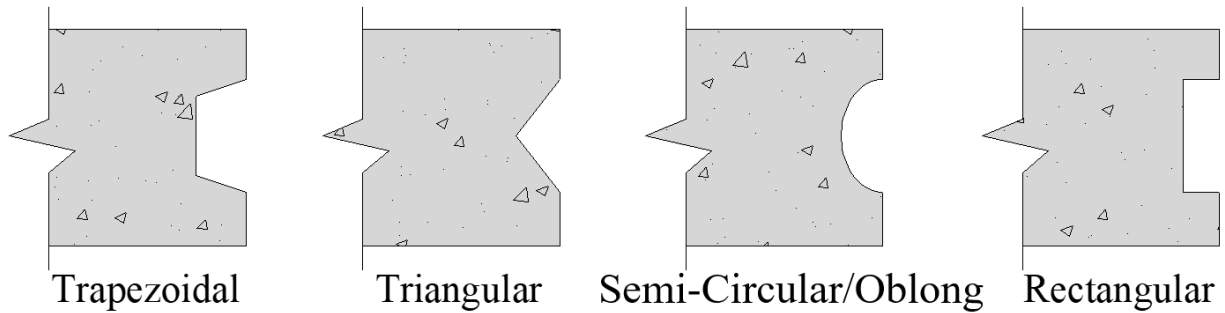
The shape of the shear key affects the shear transfer between panels and the cracking behavior of the connection. Male-to-female shear keys (shown in figure 10) were used in some early prefabricated deck systems, and most did not include reinforcement crossing the joint. (Badie and Tadros 2008) This type of shear key requires a minimal gap between the panels to transfer shear loads. The space between the key would be filled with a compressible seal, epoxy, or grout. This type of connection is not typically used in more recent deployments due to poor performance observed in some in-service bridges. These systems were observed to have fit-up issues which resulted in difficulty grouting and subsequent leakage through the connection. (Kropp, Milinski, and Gutzwiller 1975; Issa et al. 1995)

Female-female key shapes (shown in figure 10) have become preferred in recent deployments of prefabricated bridge deck systems given that wider construction tolerances can be used. (Culmo 2009; Sullivan 2007) found that grouted female-female connections were easier to construct and more durable than epoxied male-female connections. Typical shapes used for female-female shear keys are shown in figure 11 and include semi-circular, trapezoidal, triangular, and rectangular. (Badie and Tadros 2008)



Source: FHWA

Figure 10. Illustration. Shear key configurations.



Source: FHWA

Figure 11. Illustration. Common female-to-female shear key shapes.

Precast Panel Surface Preparation

A strong bond between the precast panel surface and the field-cast grout material is needed to prevent cracking at the interface between the two materials. Premature or unexpected cracking at the interface between the two materials can lead to moisture or contaminate ingress, which can promote corrosion of the reinforcing steel.

The bond of grout materials (or concrete) cast against precast (or existing) concrete has been shown to be greatly affected by the surface roughness of the precast concrete. (Abu-Tair, Rigden, and Burley 1996; Momayez et al. 2005; Santos, Júlio, and Silva 2007) A number of different surface preparations have been investigated including pressure washing, sandblasting, hand chiseling, and exposing the internal aggregate of the precast concrete. (Abu-Tair, Rigden, and Burley 1996; Momayez et al. 2005; Santos, Júlio, and Silva 2007; De La Varga, Haber, and Graybeal 2017; Harris et al. 2014; I. De la Varga, Haber, and Graybeal 2018) In general, research has shown that the bond strength between the grout cast against the precast concrete improves as the precast concrete surface becomes rougher. Santos, Júlio, and Silva (2007) used digital imaging to quantify the level of surface roughness in precast concrete with as-cast, wire-brushed, and sand blasted surface preparations. They found that bond between concrete cast against precast concrete improved significantly as the level of surface roughness of precast concrete increased. De La Varga, Haber, and Graybeal (2017) reported a similar result that pertained to exposed aggregate surface finishes. When non-shrink cementitious grouts are bonded to a concrete substrate, the aggregate exposure level increases, which increases the bond strength between the two materials when tested in direct tension. Additional research has shown that the properties of the grout material and the presence of moisture in the existing concrete can also impact the bond strength. (Abu-Tair, Rigden, and Burley 1996; De La Varga et al. 2017)

Researchers have developed and employed a number of different bond test methods for evaluating the bond strength between grout materials and precast concrete; these methods include direct tension pull-off tests, compressive slant shear cylinder (or cube) tests, splitting cylinder tests, and flexural beam tests, among others. (Harris et al. 2014; De La Varga, Haber,

and Graybeal 2017) Many of these test methods have been based on ASTM standard test methods or have been developed to study specific states of stress at the interface between two bonded materials. Research tends to indicate that different test methods can produce potentially conflicting or misleading results related to bond strength. (De La Varga, Haber, and Graybeal 2017)

SUMMARY

Although numerous laboratory studies have been conducted to investigate the performance and behavior of different connection details, these studies have had limited scope, focusing only on a small set of variables at a time. Furthermore, some aspects of deck-level connections have been investigated only from a single point of view. For example, the effect of precast concrete surface preparation on interface bond strength has been primarily investigated using small-scale specimens tested under monotonic static loading. Thus, although these tests provide valuable insights, they do not reflect realistic loading scenarios and therefore do not necessarily reflect the performance that may be anticipated during field deployments of these connection details.

CHAPTER 3. EXPERIMENTAL PROGRAM

INTRODUCTION

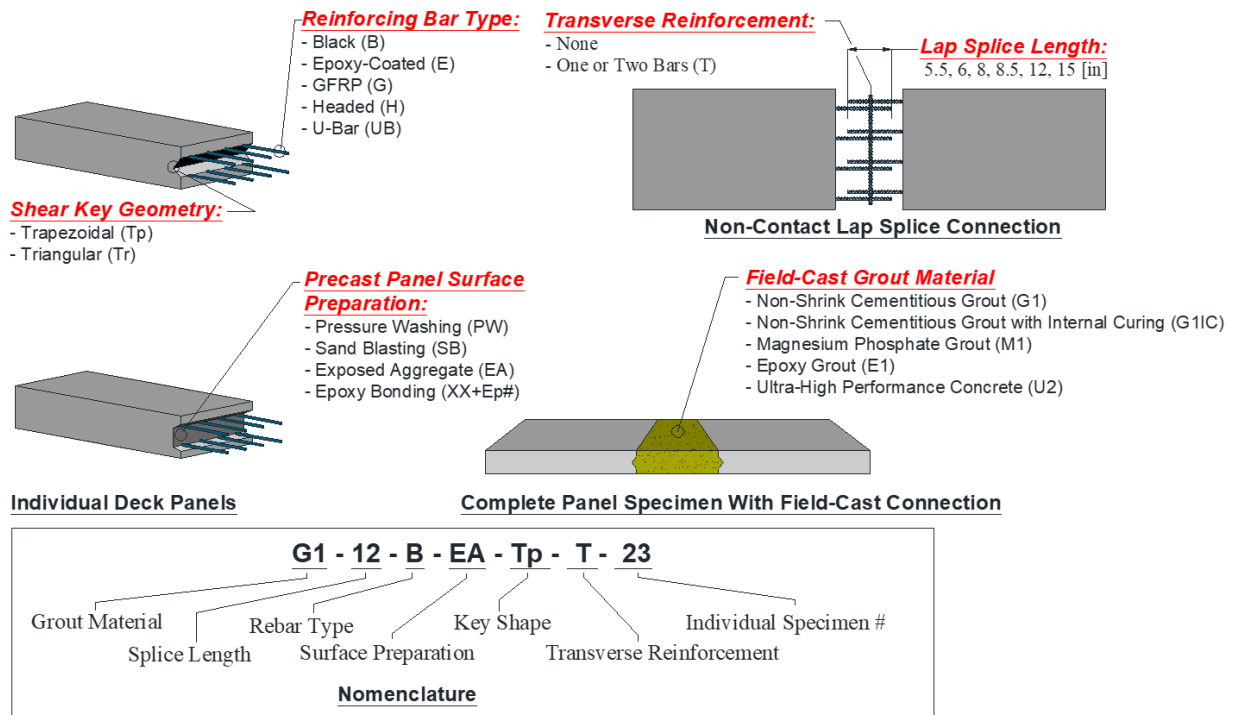
The research team developed an experimental program to investigate the performance of different field-cast grout materials and connection details for deck-level connections in prefabricated concrete bridge deck systems. The materials and details selected for investigation are either currently used in these connections or have the potential for such applications. Two different specimen types were used to evaluate the performance of different field-cast grouts and connection details: large-scale deck-level connection specimens and small-scale bond characterization specimens. The construction and testing of all specimens was carried out at the FHWA Turner-Fairbank Highway Research Center (TFHRC).

This chapter describes the experimental program. The six primary test variables included in the study are discussed first; each variable is discussed in a separate section. In subsequent sections, large-scale deck panel connection specimen details and small-scale bond characterization specimen details are discussed, respectively. The following two chapters present the test results for the deck panel specimens and bond characterization tests, respectively.

OVERVIEW OF TEST SPECIMENS AND VARIABLES

Figure 12 depicts the tests variables studied using large-scale deck-level connection specimens. Deck-level connection specimens were comprised of two prefabricated deck panel elements, each with protruding reinforcement. That reinforcement was interlaced to form a non-contact lap splice connection region, which was then filled with grout. These components are identified in figure 12 along with other relevant information related to the test variables. The test variables are shown in bold italics, and a list of the different variables is provided with the variable nomenclature, which is shown in parentheses.

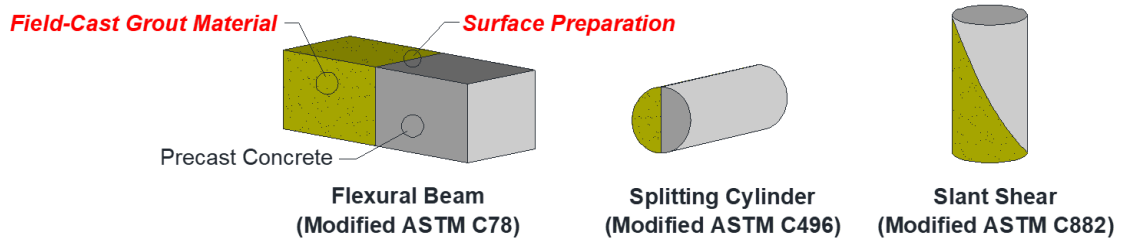
Deck-level connection specimens were identified by combining the test variable nomenclature into a single string. An example is shown at the bottom of figure 12, G1-12-B-EA-Tp-T-23, which denotes that the specimen employed non-shrink cementitious grout (G1) in the connection, a 12-inch lap splice, black rebars (B), exposed aggregate (EA) shear key surface preparation, trapezoidal (Tp) key geometry, and had transverse reinforcement (T) in the connection. The majority of specimens did not employ transverse reinforcement, commonly referred to as lacer bars, within the connection. Specimens with transverse bars are identified with a T at the end of the identification string. It should be noted that not all possible combinations of test variables were investigated. For example, specimens that employed ultra-high performance concrete grout (U2) were only studied using 5.5-inch (14-cm) lap splices. The number shown at the end of the string denotes the individual specimen number. In some cases, replicate specimens were tested. Thus, this number was used to uniquely identify specimens with similar parameters combinations.



Source: FHWA

Figure 12. Illustration. Deck-level connection specimens and test variables.

The small-scale bond characterization tests were used to investigate how the grout materials and precast concrete surface preparation affect the tensile bond behavior of the concrete-grout interface. A secondary objective of the bond characterization tests was to evaluate the applicability of each test method for determining the performance of different grout/surface preparation combinations. Thus, the research team investigated three different tests methods that were based on current ASTM standard test methods and that could be easy executed at most state department of transportation (DOT) material testing labs. Figure 13 shows an illustration of the three test methods and identifies the ASTM standard used as a starting point. The flexural beam bond test was based on ASTM C78, *Standard Test Method for Flexural Strength of Concrete (Using Simple Beam with Third-Point Loading)*. (ASTM C78/C78M-16, 2016). The splitting cylinder bond test was based on ASTM C496, *Standard Test Method for Splitting Tensile Strength of Cylindrical Concrete Specimens*. (ASTM C496/C496M-11, 2004) The slant shear bond test was based on ASTM C882, *Standard Test Method for Bond Strength of Epoxy-Resin Systems Used with Concrete by Slant Shear*. (ASTM C882/C882M-13a, 2013)



Source: FHWA

Figure 13. Illustration. Bond characterization specimens and test variables.

TEST VARIABLES

The following sections discuss the details of each test variable.

Field-Cast Grouts

Grout materials were selected based on previous research conducted at TFHRC, applicability to onsite construction processes, and suitable published material properties. (Swenty and Graybeal 2013) Four grouts available commercially in the North American market were investigated: a non-shrink cementitious grout denoted “G1,” a magnesium phosphate rapid-setting cementitious grout denoted “M1,” an epoxy grout denoted “E1,” and an ultra-high performance concrete grout denoted “U2.” Each grout was batched, mixed, and placed according to manufacturer specifications. Furthermore, each grout material was marketed by their respective manufacturers to have low shrinkage and high early strength. Table 1 provides some select manufacturer reported material properties. Previous works by Graybeal (2006), Swenty and Graybeal (2013), and De La Varga and Graybeal (2016) provide more detailed data related to the properties and characteristic of these materials. A fifth grout material, which was a modified version of grout G1, was also investigated. This material was denoted “G1IC” and employed light-weight aggregate (LWA) to provide internal curing (IC).

The non-shrink cementitious grout and magnesium phosphate grout were supplied by the manufacturer in bags containing the solid fraction (i.e., cementitious materials, additives, fine aggregates, and solid admixtures) that was mixed with the manufacturer’s recommended water content. G1 and M1 required maximum water-to-solids ratios (w/s) of 0.18 and 0.084, respectively. The batching and mixing details for G1 and M1 grouts are listed in table 2.

The epoxy grout was a three-component system comprised of an epoxy resin, liquid hardener, and pre-bagged aggregates. The material was mixed according to the manufacturer’s recommendations. The batching and mixing details for the E1 grout are listed in table 3.

The UHPC used in this study was a proprietary UHPC-class material supplied by a U.S.-based subsidiary of a multinational corporation. This product had five primary constituents that were supplied by the manufacturer: a pre-blended, pre-bagged powder mix containing all the solids

(cementitious and non-cementitious) except for fibers; a phosphonate plasticizer; a polycarboxylate high-range water-reducing admixture; a non-chloride accelerator; and steel fibers. The dry powder constituents were mixed with a measured amount of water, following the manufacturer's recommendations. The fibers had a nominal length of 0.5 inch (13 mm), a nominal diameter of 0.008 inch (0.2 mm), and tensile strengths greater than 290 ksi (2,000 MPa), as reported by the manufacturer. Table 1 lists the supplier-recommended mixture proportions, with a water-to-cementitious materials ratio (w/c) of about 0.18 and a recommended fiber volume fraction of 2 percent. The batching and mixing details for the U2 grout are listed in table 4.

Internal curing has been shown to reduce shrinkage in cement-based materials (Bentz and Weiss 2011; RILEM Report 41 2007). Cementitious grouts can undergo considerable autogenous and drying shrinkage. (De la Varga and Graybeal 2015) Dimensional incompatibilities between the grout and the substrate can cause the development of tensile stresses within the grout material or the substrate, leading to premature cracking, or they can cause stresses at the interface leading to loss of bond. IC would then be included to address both issues. Pre-packaged cementitious grouts can often be extended using an additional quantity of aggregate for volumetrically large pours. IC can be thought of as an extension of the grouts using fine LWA rather than normal weight aggregate. In other words, the LWA would be added on top of the ordinary mixture proportions. This is different than what is conventionally done in supplying IC for concrete, where the LWA replaces part of the normal-weight sand. (Bentz, Lura, and Roberts 2005) More information about the inclusion of IC in cementitious grouts can be found in the literature. (De la Varga and Graybeal 2016)

To create material G1IC, fine LWA was added to plain G1 grout. The fine LWA consisted of rotary kiln-expanded shale with a specific (dry) gravity of 1.56, a 24-h water absorption of 17 percent by dry mass, and a desorption value of 92 percent when exposed to a controlled relative humidity (RH) of about 94 percent at 23 °C, as per ASTM C1761. The amount of LWA needed for each of the grouts was based on the amount of chemical shrinkage in each system, as it is commonly done in IC mixture designs for conventional concretes. (Bentz, Lura, and Roberts 2005) For G1IC, the LWA represents approximately 25 percent of the total unit volume. More details on the inclusion of IC via LWA in cementitious grouts can be found in the literature. (De la Varga and Graybeal 2016)

Grouts were mixed using a large pan-style mixer with orbital mixing action and a 16 ft³ (0.45 m³) capacity. Because UHPC requires more mixing energy than conventional grouts, batches never exceeded 5 ft³ (0.14 m³).

Table 1. Selected manufacturer-reported properties.

Grout ID	Grout Type	24-hr Compressive Strength ^a , psi (MPa)	28-day Compressive Strength ^a , psi (MPa)	Flexural Strength, psi (MPa)
G1	Non-shrink cementitious	4,000 (27.6) ^b	8,000 (55.2) ^b	Not Reported
M1	Magnesium phosphate	6,000 (41.4) ^b	8,500 (58.6) ^b	550 (3.8) ^c
E1	Epoxy grout	14,000 (96.6) ^d	Not Reported	4,800 (33.1) ^e
U2	Ultra-high performance concrete	Not Reported	20,000 (140) ^f	4,300 (30) ^f

^a Minimum reported value tested at or around 72° F (22).

^b Measured using ASTM C109.

^c 1-day strength measured using ASTM C78.

^d Measured using ASTM C579.

^e Measured using ASTM C580.

^f Test methods not reported.

Table 2. Batching details for cementitious grouts G1 and M1.

Grout ID	Grout, lbs (kg)	Water, lbs (kg)	Mix Time, Minutes	Lab Temperature, °F (°C)
G1 ^a	121.9 (55.3)	21.9 (9.9)	5	68-78 (20-26)
M1 ^b	128.2 (58.1)	10.7 (4.8)	2	68-78 (20-26)

^a The water-to-grout ratio for G1 was 0.18 by weight.

^b The water-to-grout ratio for M1 was 0.084 by weight.

Table 3. Batching details for epoxy grout E1.

Grout ID	Dry Aggregate, lbs (kg)	Resin, lbs (kg)	Hardener, lbs (kg)	Mix Time ^b , Minutes	Lab Temperature, °F (°C)
E1 ^a	200.0 (90.7)	23.8 (10.8)	4.0 (1.8)	2	68-78 (20-26)

^a The polymer binder-to-aggregate ratio was 0.139 by weight. The resin-to-hardener ratio was 5.95 by weight.

^b Hardener and resin were mixed together for 1.5 minutes. Once the last bag of dry aggregate was placed in the mixer, additional 2 minutes of mixing (all components together).

Table 4. Batching details for ultra-high performance concrete grout U2.

Grout ID	Premix, lbs (kg)	Water, lbs (kg)	Plasticizer #1 ^a , lbs (kg)	Plasticizer #2 ^b , lbs (kg)	Steel Fibers, 2.0 percent, lbs (kg)	Mix Time ^c , Minutes	Lab Temperature, °F (°C)
U2	137.0 (62.1)	9.36 (4.24)	1.12 (0.51)	0.75 (0.34)	9.74 (4.42)	18-26	68-78 (20-26)

^a Modified phosphonate plasticizer.

^b Modified polycarboxylate high-range water-reducing admixture.

^c The total mix time was dependent on the time it took to obtain the paste consistency.

Reinforcement Types and Detailing

Three types of reinforcement popular for bridge deck construction were investigated in this research: black bars denoted by “B” (figure 14), epoxy coated bars denoted by “E” (figure 15), and pultruded glass fiber-reinforced polymer (GFRP) bars denoted by “G” (figure 16). All metallic bars were U.S. Grade 60 mild steel deformed reinforcing bars conforming to ASTM A615. (ASTM A615/A615M-16, 2016)



Source: FHWA

Figure 14. Photo. Black reinforcing bar; Denoted by “B.”



Source: FHWA

Figure 15. Photo. Epoxy-coated reinforcing bar; Denoted by “E.”



Source: FHWA

Figure 16. Photo. GFRP reinforcing bar; Denoted by “G.”

Reinforcement continuity between precast deck panel halves was achieved using non-contact lap splices. Three non-contact lap splice reinforcement details were studied: straight bars, headed bars (figure 17), and bars with a 180-degree hook (figure 18), which are otherwise referred to as “U-bars.” The headed bars and U-bars details used black steel. The notation used to identify these details are “H” and “UB,” respectively. U-bars had an internal bend diameter D equal to 2.75 inches (70 mm); this bend diameter is equal to 4.4 bar diameters. The AASHTO LRFD specifies that the minimum diameter of bend of 6 bar diameters for #5 bars and smaller. (American Association of State Highway and Transportation Officials 2016) Thus, this is a smaller bend diameter than allowed by the AASHTO LRFD.



Source: FHWA

Figure 17. Photo. Headed reinforcing bar; Denoted by “H.”



Source: FHWA

Figure 18. Photo. Black U-shaped reinforcing bar; Denoted by “UB.”

Examples of the three non-contact lap splice details investigated are shown in figure 19. The lap splice length is defined as the length over which two adjacent reinforcing bars overlap. This length is measured from end to end for straight bars, from the inside of the head for headed bars, and from inside the bend for U-bars. The lap splice length required to transfer stress between adjacent bars has been shown to be highly dependent on the tensile strength of the embedment

material. (Sagan, Gergely, and White 1991) Therefore, a variety of different lap splice lengths were investigated.



A. Straight bars

B. Headed bars

C. U-bars

Source: FHWA

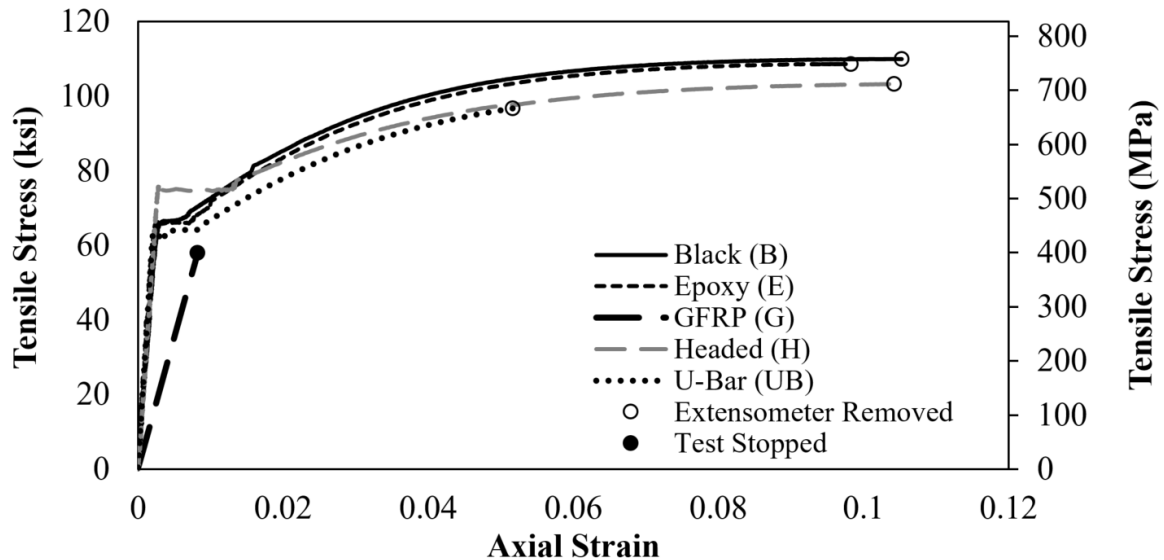
Figure 19. Photos. Non-contact lap splice details investigated.

Each bar type was subjected to tensile testing to determine actual mechanical properties. Metallic bar samples were tested according to ASTM A370, and GFRP bar samples were tested per ASTM D7205. Two specimens were tested for each bar type. During tensile loading, strain was measured from a digital extensometer, and load was measured from a load cell on board the loading frame. The measured material properties are listed in table 5, and a set of representative stress-strain curves are shown in figure 20. All steel reinforcing bars failed as a result of fracture. Prior to failure, the testing procedure was paused to remove the extensometer used to measure strain to prevent damage to the instrument. The point at which the extensometer was removed is noted in figure 20. Testing was resumed after the removal of the extensometer. It should be noted that tests on GFRP bars were stopped prior to reaching the ultimate tensile strength of the bar because of grip slippage, which is also noted in figure 20.

Table 5. Measured material properties of reinforcing bars.

Reinforcement Type	Elastic Modulus, ksi (GPa)	Yield Strength ^a , ksi (MPa)	Ultimate Tensile Strength, ksi (MPa)
Black “B”	27,800 (192)	67.6 (466)	110.3 (760)
Epoxy Coated “E”	28,300 (195)	66.6 (459)	108.8 (750)
GFRP “G”	7,100 (48.5)	-	105 (724) [†]
Headed “H”	27,600 (190)	74.9 (516)	103.4 (712)
U-Bar “UB”	30,300 (209)	62.7 (432)	102.7 (708)

[†] Manufacturer suggested material property



Source: FHWA

Figure 20. Graph. Measured axial stress-strain behavior of reinforcing bars.

Shear Key Surface Preparation

Previous laboratory studies have shown that the bond strength at a concrete cold joint can be enhanced by increasing the roughness of the existing (or otherwise precast) concrete surface. (Momayez et al. 2005) Three concrete surface preparation methods were investigated to promote the bond between the field-cast grout and precast concrete: pressure washing, sand blasting, and exposing the internal aggregate of the precast concrete. The application of epoxy bonding agents to the precast concrete surface prior to casting the grout material was also investigated. Each surface preparation method is discussed in the following sections.

Pressure Wash (PW)

Pressure washed surfaces, denoted by PW, were prepared using a pressure washer that provided a maximum 2,800 psi (19.3 MPa). Surfaces were subjected to washing for approximately ten

seconds at a distance of between 6 inches and 12 inches (152 mm and 305 mm) as shown in figure 21. The finished surfaces were free of any loose particles and were slightly rough to the touch. A representative photo of a PW surface is shown in figure 22.



Source: FHWA

Figure 21. Photo. Pressure washing procedure.



Source: FHWA

Figure 22. Photo. Final pressure wash surface preparation.

Sand Blast (SB)

Sand blasted surfaces, denoted by SB, were prepared using a commercially available portable sandblaster with a commercially available sand blast media. Surfaces were sand blasted at a distance of between 6 inches and 8 inches (152 mm to 203 mm) for different durations,

depending on the surface area, to achieve a uniform roughened surface. This procedure is shown in figure 23. Surfaces were pressured washed to remove any media from the surface after sand blasting was completed. A representative photo of a SB surface is shown in figure 24.



Source: FHWA

Figure 23. Photo. Sand blasting procedure.



Source: FHWA

Figure 24. Photo. Final sand blasted surface preparation.

Exposed Aggregate (EA)

The exposed aggregate surface, denoted by EA, was prepared using a combination of an in-form retarder and pressure washing. Prior to placing the concrete, relevant form surfaces (shown in figure 25) were covered with a thin layer of a commercially available in-form set retarder. The

retarder was applied with a brush 20-60 minutes prior to placing concrete to ensure the layer was dry. Within 24 hours after placement, specimens were removed from the formwork and the relevant surfaces were pressure washed to remove cement paste. Figure 26 shows a photo of the finished EA surface preparation.



Source: FHWA

Figure 25. Photo. In-form retarder used on specimen formwork.



Source: FHWA

Figure 26. Photo. Final exposed aggregate surface preparation.

Epoxy Bonding

Epoxy bonding agents were used to promote bonding between precast concrete and grout for selected specimens with PW or SB surface preparations. Two different commercially available

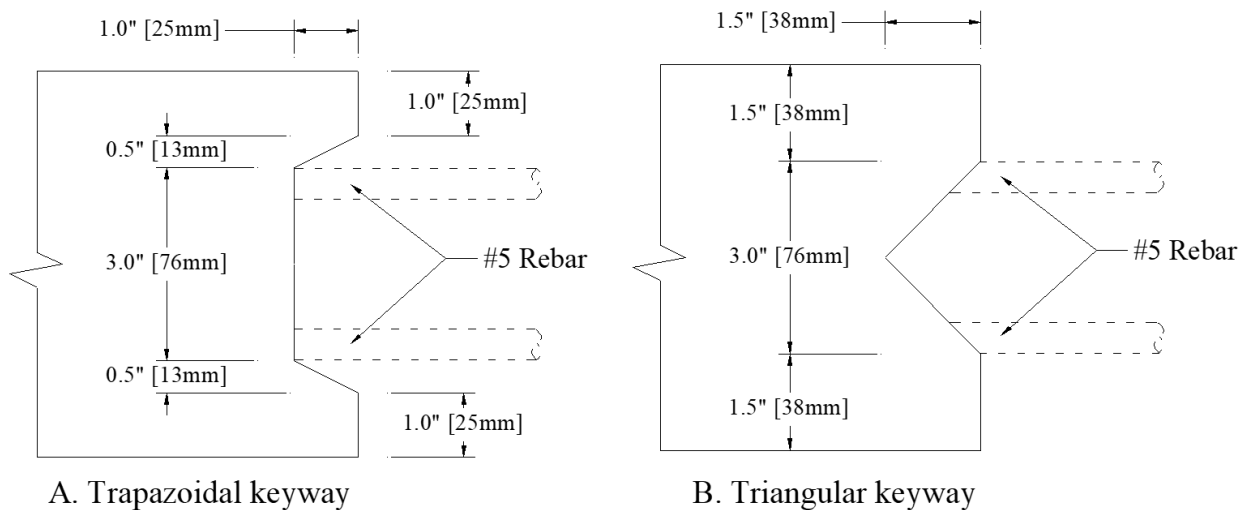
epoxies were tested. Epoxy #1, denoted Ep1, is a two-part, high modulus epoxy adhesive (1:1 resin-to-hardener ratio) with a pot life of approximately 20 to 30 minutes. Epoxy #2, denoted Ep2, is also a two-part epoxy adhesive (1:1 resin-to-hardener ratio) with a pot life of approximately 40 to 60 minutes.

Prior to applying the bonding agent to the concrete surface, the specimens were pressure washed and allowed to dry. Once dry, the epoxy adhesive was applied to the precast surface by brush and was allowed to set-up for approximately 20 minutes prior to casting grout. It should be noted that the application of epoxy by brush was relatively difficult due to the presence of reinforcing bars in the case of deck specimens and the lack of space in the molds of companion specimens.

The nomenclature used to identify a surface preparation with an epoxy bonding agent was the surface preparation identifier plus (“+”) the epoxy type. For example, a sand-blasted surface with epoxy type 1 would be identified as SB+Ep1.

Shear Key Geometry

Two different shear key geometries, which are typically used in precast deck panel construction, were investigated: a trapezoidal keyway, denoted by Tp, and a triangular keyway, denoted by Tr. The geometry of these keyways is shown in figure 27.



Source: FHWA

Figure 27. Illustration. Shear key details.

Transverse Reinforcement

Experimental studies have shown that providing confinement in the grouted connection region can improve performance of non-contact lap splice connection when using straight or headed bars. (M. Keith Thompson et al. 2006; ACI Committee 408 2003) The connection region for some specimens contained transverse bars, commonly referred to as lacer bars; the research team

investigated whether these bars resulted in better connection performance. Select specimens with straight or headed bars utilized either a single transverse bar or two transverse bars; these bars were either #4 or #5 black bars composed of U.S. Grade 60 ASTM A615 steel. On the other hand, each specimen with U-bars employed two U.S. Grade 60 ASTM A615 #4 bars. Examples of the transverse reinforcement used in the connection region are shown in figure 28. Transverse reinforcement was placed inside the longitudinal reinforcement on the tension-side of the connection in the specimens with straight or headed bar lap splices, and it was placed inside the 180-degree hook in the U-bar specimens.



A. Example of transverse reinforcement for straight lap spliced bars



B. Example of transverse reinforcement for lap spliced U-bars

Source: FHWA

Figure 28. Photos. Examples of transverse reinforcement used in the connection region.

SUMMARY OF TEST VARIABLE NOMENCLATURE

Table 6 provides a summary of the test variables and the associated nomenclature for a deck-level connection test.

Table 6. Summary of test variable nomenclature.

Variable Category	Variable	Nomenclature
Grout type	Non-shrink cementitious grout	G1
Grout type	Magnesium phosphate grout	M1
Grout type	Epoxy grout	E1
Grout type	Ultra-highway performance concrete	U2
Grout type	Non-shrink cementitious grout with internal curing	G1IC
Reinforcement type	Black bars	B
Reinforcement type	Epoxy-coated bars	E
Reinforcement type	Headed bars	H
Reinforcement type	U-shaped bars	UB
Reinforcement type	Glass fiber-reinforced bars	G
Shear key surface preparation	Pressure washed	PW
Shear key surface preparation	Sand blasted	SB
Shear key surface preparation	Exposed aggregate	EA
Shear key surface preparation	Epoxy bonding agent #1	Ep1
Shear key surface preparation	Epoxy bonding agent #2	Ep2
Shear key geometry	Trapezoidal shear key	Tp
Shear key geometry	Triangular shear key	Tr
Transverse reinforcement	No transverse reinforcement	“ _ “
Transverse reinforcement	Transverse reinforcement included	T

DECK-LEVEL CONNECTION SPECIMENS

Test Matrices

Deck-level connection specimens were intended to have details representative of prefabricated bridge deck systems currently being employed in the field. A total of 75 specimens were created; three specimens were used to configure loading protocols and the remaining 72 specimens were used in the experimental investigation. Of the 72 test specimens, four were cast monolithically to establish baseline behavior. The test matrix for monolithic specimens is presented in table 7.

Two of the monolithic specimens employed non-contact lap-spliced black bars, and two specimens had continuous longitudinal reinforcing bars. Specimen Monolithic-Continuous-B-25 was intended to serve as the primary control specimen for precast specimens with mild steel reinforcing bars, and specimen Monolithic-Continuous-G-67 was intended to serve as the primary control specimen for precast specimens with GFRP reinforcing bars.

Table 7. Test matrix for monolithic specimens.

Specimen ID	Joint Width, in (mm)	Splice Lap Length, in (mm)	Precast Concrete Surface Treatment	Shear Key	Rebar Type	Transverse Reinforcement
Monolithic-24-B-4	-	24 (610)	-	-	B	N/A
Monolithic-12-B-21	-	12 (305)	-	-	B	N/A
Monolithic-Continuous-B-25	-	-	-	-	B	N/A
Monolithic-Continuous-G-67	-	-	-	-	G	N/A

N/A = not applicable

A total of 32 deck-level specimens employed G1 grout in the connection. The test matrix for these specimens is presented in table 8. In some cases, repeat testing was conducted on a given combination of parameters. Thus, each test specimen was given a unique identification number, Specimen ID. This number is shown in each test matrix table. A total of five precast deck panel specimens employed M1 grout in the connection. The test matrix for these specimens is presented in table 9. A total of 15 deck-level connection specimens employed E1 grout in the connection. The test matrix for these specimens is presented in table 10. A total of 15 deck-level connection specimens employed U2 grout in the connection. The test matrix for these specimens is presented in table 11.

Table 8. Test matrix for specimens with G1 grout connections.

Specimen ID	Joint Width, in (mm)	Splice Lap Length, in (mm)	Precast Concrete Surface Treatment	Shear Key	Rebar Type	Transverse Reinforcement
G1-6-H-SB-Tp-54	8 (203)	6 (152)	SB	Tp	H	None
G1-6-H-SB-Tp-T-55	8 (203)	6 (152)	SB	Tp	H	1 - #4
G1-8.5-UB-EA-Tr-T-73	10 (254)	8.5 (216)	EA	Tr	UB	2 - #4
G1IC-8.5-UB-EA-Tr-T-74	10 (254)	8.5 (216)	EA	Tr	UB	2 - #4
G1-12-B-PW-Tp-48	14 (356)	12 (305)	PW	Tp	B	None
G1-12-B-PW-Tp-50	14 (356)	12 (305)	PW	Tp	B	None
G1-12-B-PW-Tp-58	14 (356)	12 (305)	PW	Tp	B	None
G1-12-B-PW-Tr-27	14 (356)	12 (305)	PW	Tr	B	None
G1-12-B-PW-Tr-29	14 (356)	12 (305)	PW	Tr	B	None
G1-12-B-PW+E1-Tp-24	14 (356)	12 (305)	PW+Ep1	Tp	B	None
G1-12-B-PW+E2-Tp-22	14 (356)	12 (305)	PW+Ep2	Tp	B	None
G1-12-B-PW+E1-Tr-30	14 (356)	12 (305)	PW+Ep1	Tr	B	None
G1-12-B-PW+E2-Tr-32	14 (356)	12 (305)	PW+Ep2	Tr	B	None
G1-12-B-SB-Tp-5	14 (356)	12 (305)	SB	Tp	B	None
G1-12-B-SB-Tp-34	14 (356)	12 (305)	SB	Tp	B	None
G1-12-B-SB-Tp-35	14 (356)	12 (305)	SB	Tp	B	None
G1-12-B-SB-Tp-49	14 (356)	12 (305)	SB	Tp	B	None
G1-12-B-SB-Tp-51	14 (356)	12 (305)	SB	Tp	B	None
G1-12-B-SB-Tp-57	14 (356)	12 (305)	SB	Tp	B	None
G1-12-B-SB-Tp-59	14 (356)	12 (305)	SB	Tp	B	None
G1-12-B-SB-Tr-26	14 (356)	12 (305)	SB	Tr	B	None
G1-12-B-SB-Tr-31	14 (356)	12 (305)	SB	Tr	B	None
G1-12-B-SB-Tp-T-52	14 (356)	12 (305)	SB	Tp	B	1 - #4
G1-12-B-SB-Tp-T-53	14 (356)	12 (305)	SB	Tp	B	2 - #5
G1-12-B-SB-Tp-T-56	14 (356)	12 (305)	SB	Tp	B	2 - #4
G1-12-B-EA-Tp-23	14 (356)	12 (305)	EA	Tp	B	None
G1-12-B-EA-Tr-33	14 (356)	12 (305)	EA	Tr	B	None
G1-12-E-SB-Tp-66	14 (356)	12 (305)	SB	Tp	E	None
G1-12-G-SB-Tp-64	14 (356)	12 (305)	SB	Tp	G	None
G1-12-H-SB-Tr-28	14 (356)	12 (305)	SB	Tr	B	None
G1-15-B-SB-Tp-6	17 (432)	15 (381)	SB	Tp	B	None
G1-12-E-SB-Tp-66	14 (356)	12 (305)	SB	Tp	E	None

Table 9. Test matrix for specimens with M1 grout connections.

Specimen ID	Joint Width, in (mm)	Splice Lap Length, in (mm)	Precast Concrete Surface Treatment	Shear Key	Rebar Type	Transverse Reinf.
M1-12-B-PW-Tp-68	14 (356)	12 (305)	PW	Tp	B	None
M1-12-B-PW-Tp-71	14 (356)	12 (305)	PW	Tp	B	None
M1-12-B-SB-Tp-69	14 (356)	12 (305)	SB	Tp	B	None
M1-12-B-EA-Tp-70	14 (356)	12 (305)	EA	Tp	B	None
M1-12-B-SB-Tp-T-72	14 (356)	12 (305)	SB	Tp	B	2 - #5

Table 10. Test matrix for specimens with E1 grout connections.

Specimen ID	Joint Width, in (mm)	Splice Lap Length, in (mm)	Precast Concrete Surface Treatment	Shear Key	Rebar Type	Transverse Reinf.
E1-5.5-B-SB-Tp-63	6 (152)	5.5 (140)	SB	Tp	B	None
E1-5.5-H-SB-Tp-44	6 (152)	5.5 (140)	SB	Tp	H	None
E1-12-B-PW-Tp-46	14 (356)	12 (305)	PW	Tp	B	None
E1-12-B-PW-Tp-47	14 (356)	12 (305)	PW	Tp	B	None
E1-12-B-SB-Tp-42	14 (356)	12 (305)	SB	Tp	B	None
E1-12-B-SB-Tp-43	14 (356)	12 (305)	SB	Tp	B	None
E1-12-B-PW-Tr-37	14 (356)	12 (305)	PW	Tr	B	None
E1-12-B-SB-Tr-36	14 (356)	12 (305)	SB	Tr	B	None
E1-12-B-SB-Tr-38	14 (356)	12 (305)	SB	Tr	B	None
E1-12-B-SB-Tr-39	14 (356)	12 (305)	SB	Tr	B	None
E1-12-B-EA-Tr-41	14 (356)	12 (305)	EA	Tr	B	None
E1-12-B-EA-Tr-45	14 (356)	12 (305)	EA	Tr	B	None
E1-12-E-SB-Tp-62	14 (356)	12 (305)	SB	Tp	E	None
E1-12-G-SB-Tp-65	14 (356)	12 (305)	SB	Tp	G	None
E1-12-H-SB-Tp-40	14 (356)	12 (305)	SB	Tp	H	None

Table 11. Test matrix for specimens with U2 grout connections.

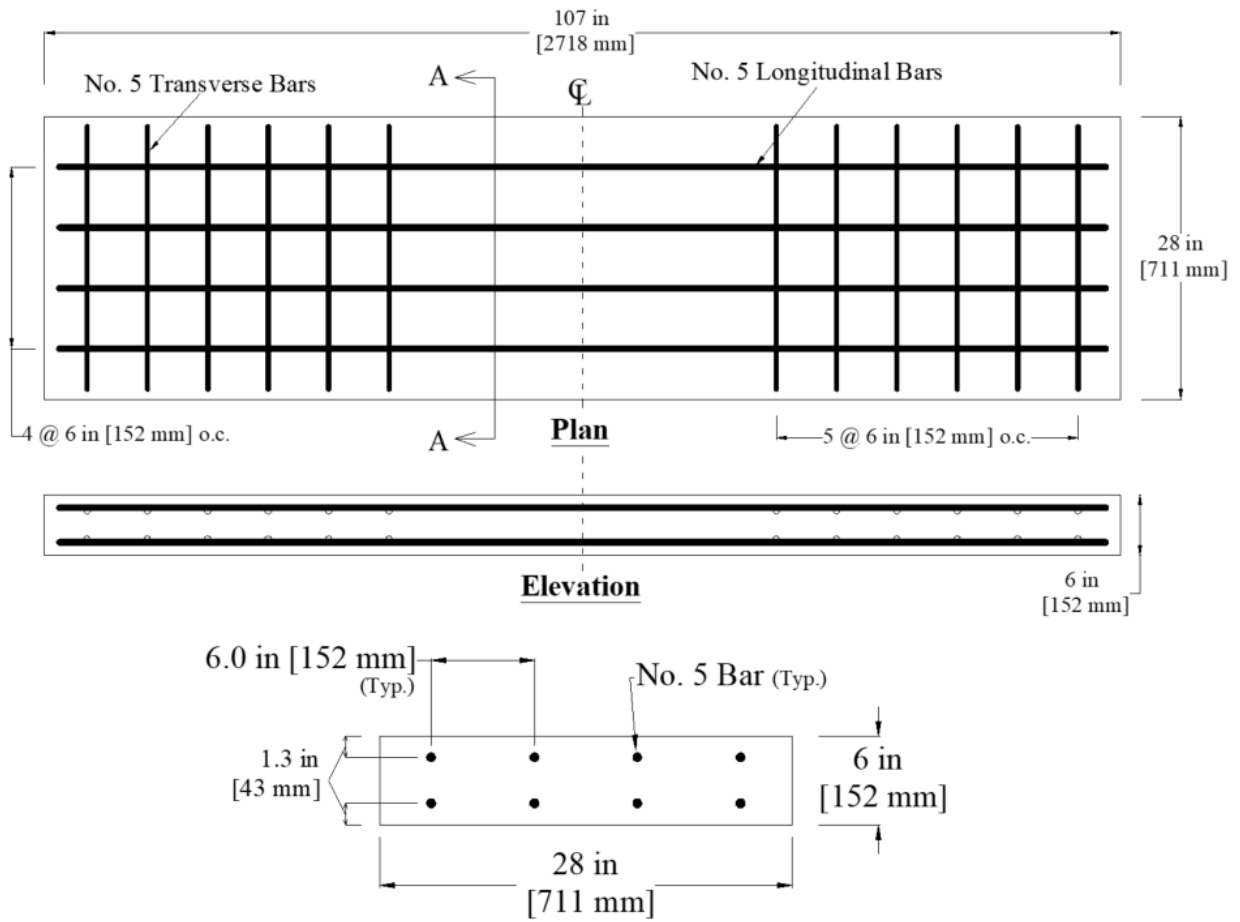
Specimen ID	Joint Width, in (mm)	Splice Lap Length, in (mm)	Precast Concrete Surface Treatment	Shear Key	Rebar Type	Transverse Reinf.
U2-5.5-B-PW+E1-Tp-10	6 (152)	5.5 (140)	PW+E1	Tp	B	None
U2-5.5-B-PW+E2-Tp-12	6 (152)	5.5 (140)	PW+E2	Tp	B	None
U2-5.5-B-SB-Tp-7	6 (152)	5.5 (140)	SB	Tp	B	None
U2-5.5-B-SB-Tp-60	6 (152)	5.5 (140)	SB	Tp	E	None
U2-5.5-B-SB-Tp-17	6 (152)	5.5 (140)	SB	Tp	B	None
U2-5.5-B-EA-Tp-8	6 (152)	5.5 (140)	EA	Tp	B	None
U2-5.5-B-PW-Tr-9	6 (152)	5.5 (140)	PW	Tr	B	None
U2-5.5-B-PW-Tr-15	6 (152)	5.5 (140)	PW	Tr	B	None
U2-5.5-B-PW-Tr-20	6 (152)	5.5 (140)	PW	Tr	B	None
U2-5.5-B-SB-Tr-11	6 (152)	5.5 (140)	SB	Tr	B	None
U2-5.5-B-SB-Tr-18	6 (152)	5.5 (140)	SB	Tr	B	None
U2-5.5-B-SB+E2-Tr-13	6 (152)	5.5 (140)	SB+E2	Tr	B	None
U2-5.5-B-SB+E1-Tr-14	6 (152)	5.5 (140)	SB+E1	Tr	B	None
U2-5.5-B-EA-Tr-16	6 (152)	5.5 (140)	EA	Tr	B	None
U2-5.5-B-EA-Tr-75	6 (152)	5.5 (140)	EA	Tr	B	None
U2-5.5-G-SB-Tp-61	6 (152)	5.5 (140)	SB	Tp	G	None

Design Details

The bending moment and shear capacities of the deck panel specimens were designed according to the provisions in the *AASHTO LRFD Bridge Design Specifications*; this calculation assumed the deck panels were monolithic. The research discussed herein began in 2011; therefore, the 5th Edition with 2010 Interim Revisions was originally used. (AASHTO 2010) Nevertheless, many of the provisions used to determine specimen capacities have not changed significantly in subsequent editions of the LRFD. It should be noted that some of the lap splice details tested herein do not adhere to the specification in the LRFD.

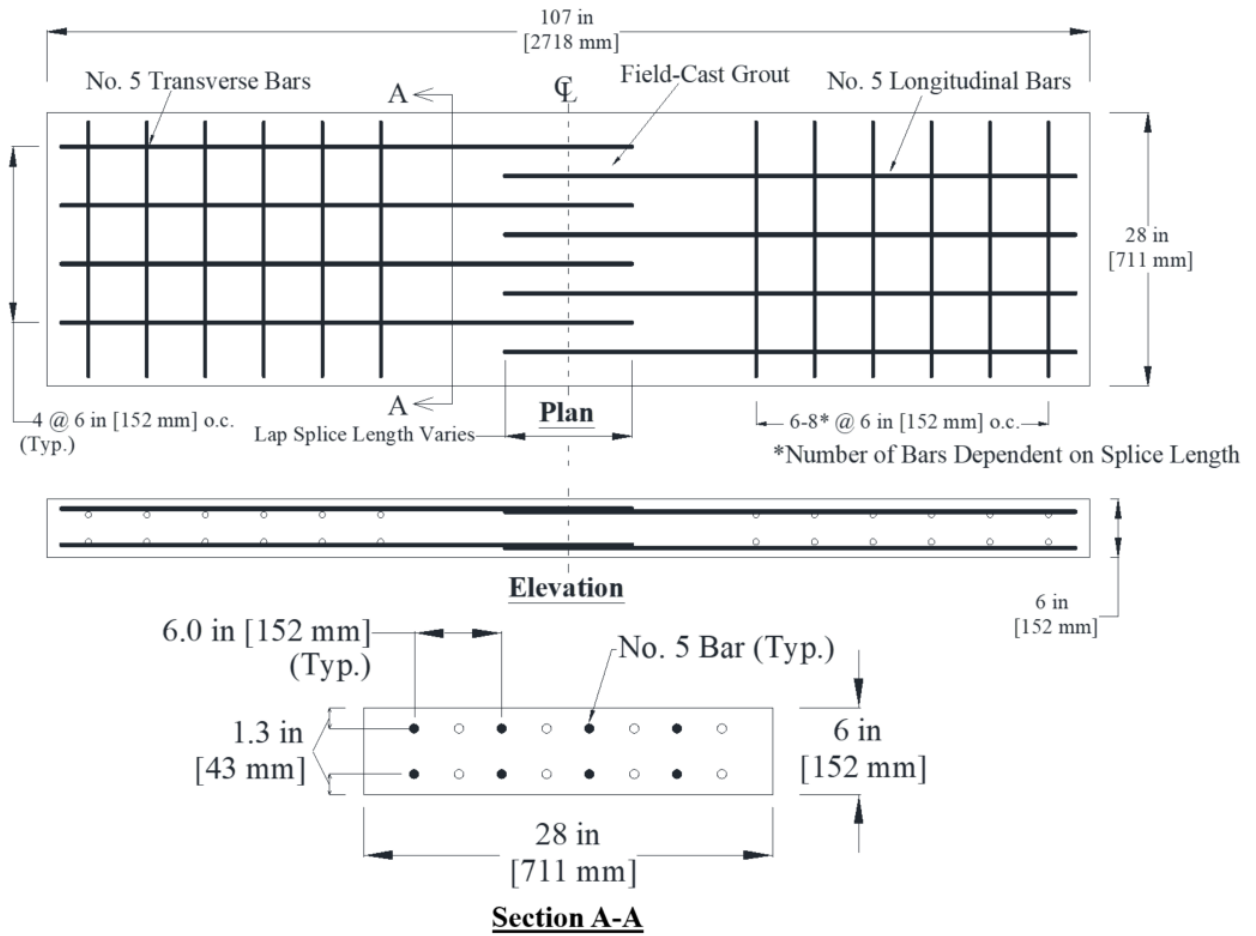
Concrete was assumed to have a compressive strength of 6 ksi (41 MPa), and steel reinforcement was assumed to have a yield strength of 60 ksi (413 MPa). The geometric and reinforcement details for monolithic specimens with continuous bars and lap-spliced bars are shown in figure 29 and figure 30, respectively. The geometric and reinforcement details for precast specimens with spliced bars are shown in figure 31. The baseline specimen with black rebars, Monolithic-Continuous-B-25, was designed to have nominal yield, M_y , and ultimate, M_n , strengths of 313.7 kip-in (35.4 kN-m) and 324.5 kip-in (36.6 kN-m), respectively. The baseline specimen with GFRP rebars, Monolithic-Continuous-G-67, was designed with the same reinforcement layout as

Monolithic-Continuous-B-25, which resulted in a nominal ultimate strength of 503 kip-in (56.8 kN-m); GFRP bars are assumed elastic until rupture, thus M_y is not calculated. Precast deck-level connection specimens were assumed to have same design strengths as baseline specimens with similar reinforcement.



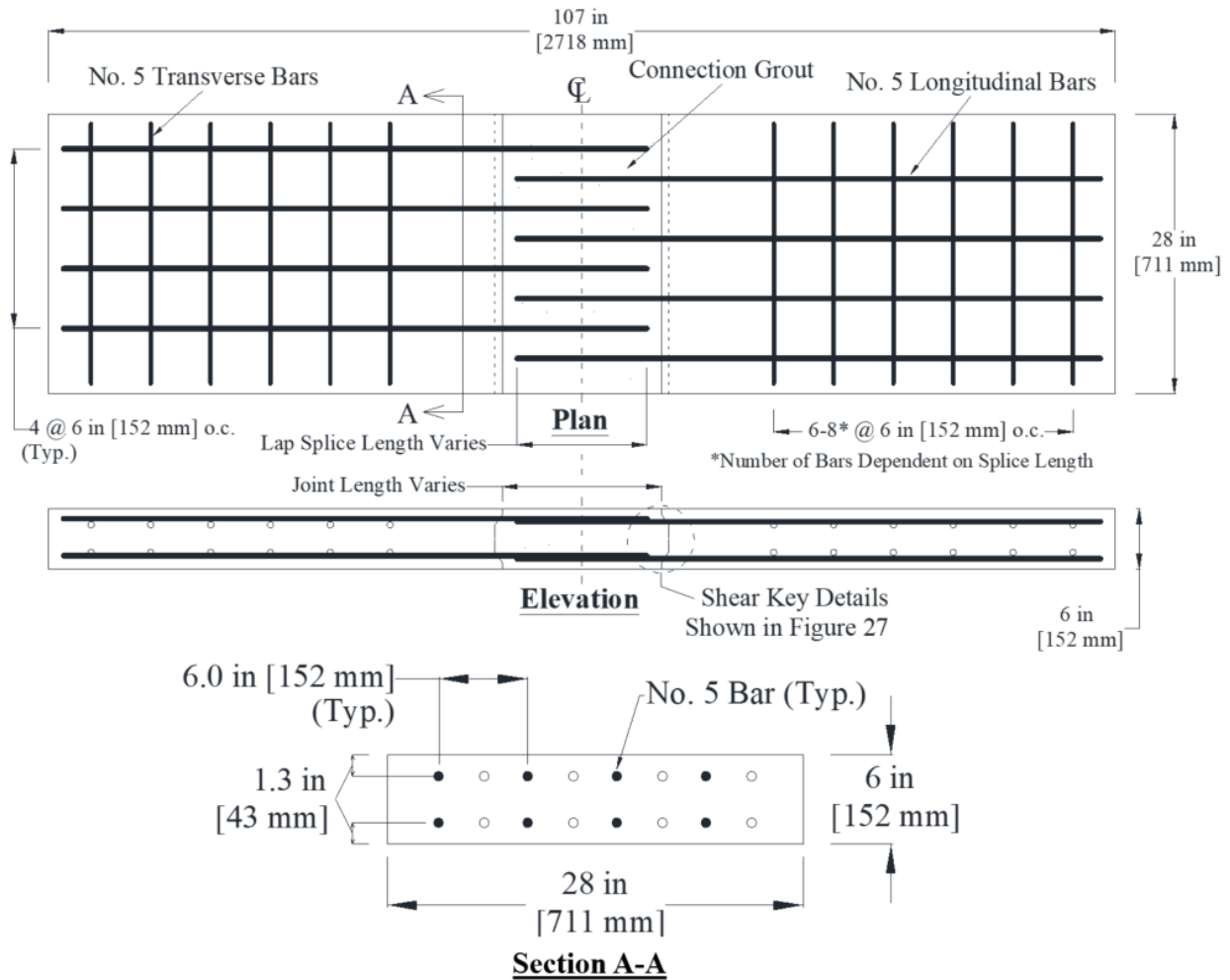
Source: FHWA

Figure 29. Illustration. Details of monolithic specimens with continuous bars.



Source: FHWA

Figure 30. Illustration. Details of monolithic specimens with lap spliced bars.



Source: FHWA

Figure 31. Illustration. Details of precast specimens with lap spliced bars.

Construction

The construction of precast deck panels and connection grouting was completed in the TFHRC Structures Lab. Figure 32 shows a photo of the deck panel specimens prior to placing concrete. Deck panels were cast in 12 batches with 6,000 psi (41.3 MPa) portland cement concrete. Table 12 lists the mix details for the concrete used in deck panel construction. Prior to placing concrete, the slump was measured in accordance with ASTM C143 and compression test cylinders were prepared according to ASTM C39. The average slump for all batches was 4.9 inches (12.4 cm), and the average 28-day strength was 6,700 psi (43.2 MPa). Once placed, concrete panels were allowed to cure in the laboratory for at least 24 hours prior to being removed from the formwork. Once removed, precast panels were stored until being prepped for constructing deck-level connections.



Source: FHWA

Figure 32. Photo. Deck panel formwork ready for concrete.

Table 12. Concrete mix design used for deck panel specimens.

Component	Quantity Per Cubic Yard	Quantity Per Cubic Meter
Fine Aggregate–Sand	1,018 lb	603.7 kg
Course Aggregate–No. 57 Stone	1,454 lb	862.2 kg
Portland Type I/II Cement	407 lb	241.4 kg
Slag Cement	163 lb	96.7 kg
Water	115 lb	68.2 kg
Air-Entrainer	2.25 oz	66.5 ml
Retarder	11.5 oz	340 ml
High-Range Water Reducer	22.8 oz	674 ml

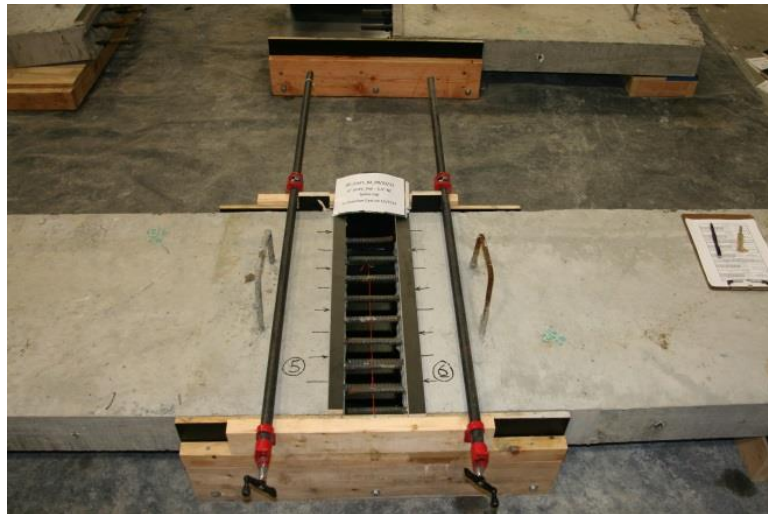
Deck specimens were constructed by placing two individual precast deck panels together to interlace the protruding rebar dowels between panels as shown in figure 33; the pocket shown is referred to as the “connection region.” The connection region was blocked off and sealed on the lower and side faces prior to grouting (shown in figure 34). Each grout material was mixed according to manufacturer specifications and placed using a bucket or wheel barrel as shown in figure 35. Grout materials were allowed to cure for at least 24 hours under controlled laboratory conditions prior to removal of forms. Figure 36 shows a photo of deck-level connection specimens after casting connection grout. During casting, 2-inch by 2-inch (50-mm by 50-mm) compression test cubes were cast according to ASTM C109 for G1, M1, and E1 grouts. The

compressive strength of UHPC grout (U2) was determined using 3-inch by 6-inch (75-mm x 150-mm) cylinders, which were also cast during the casting connections.



Source: FHWA

Figure 33. Photo. Placement of individual deck panels.



Source: FHWA

Figure 34. Photo. Connection region ready for grouting.



Source: FHWA

Figure 35. Photo. Grout placement into a connection region.



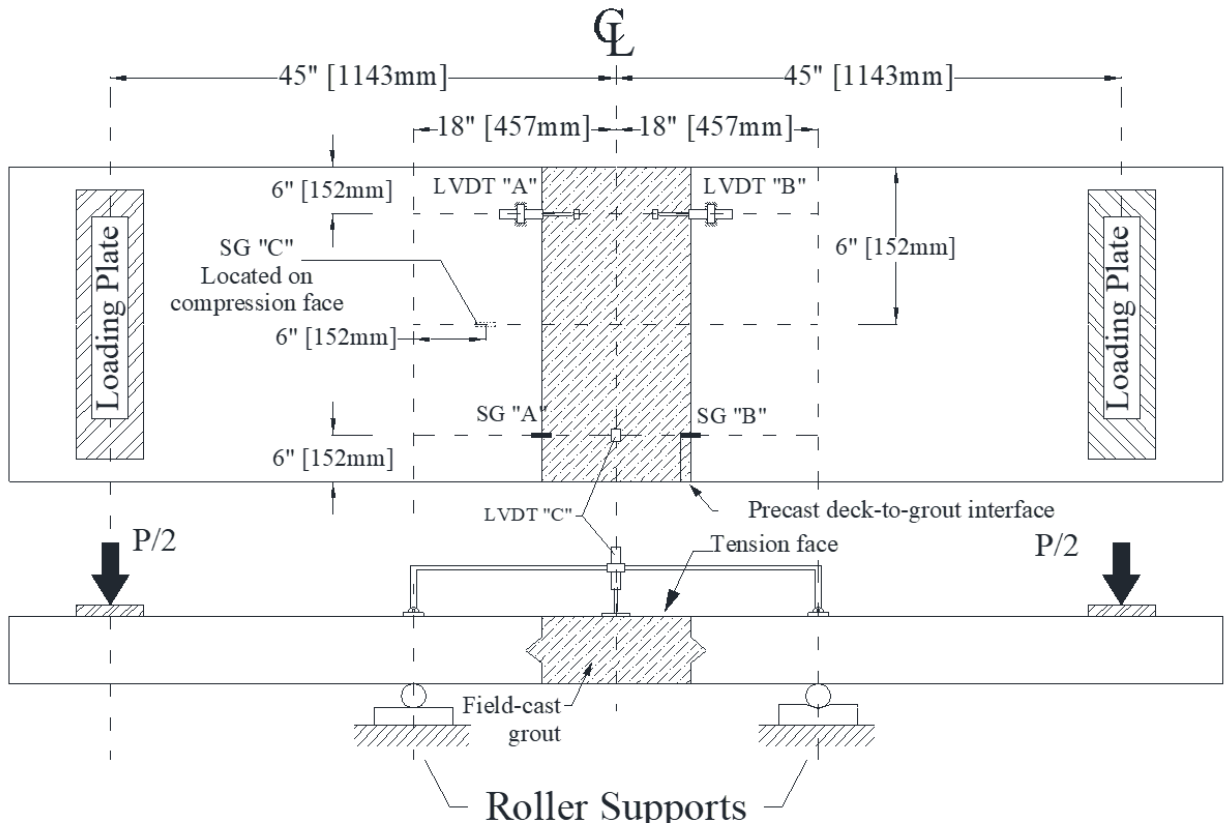
Source: FHWA

Figure 36. Photo. Specimens with completed connections.

Instrumentation

Specimens were instrumented with one of two similar instrumentation plans. The first is shown in figure 37 and was used for all specimens except those with U-bars. This instrumentation plan included three linear variable differential transducers (LVDT) and three foil-backed electrical resistance strain gages. A pair of LVDTs, denoted LVDT A and LVDT B, and a pair of strain gages, denoted SG A and SG B, were installed horizontally across the interface between the precast deck panel and the grout material to measure opening of the interface. The third LVDT, denoted LVDT C, was installed vertically at the mid-span of the constant moment region between the center supports. This sensor measured the deflection the constant moment region

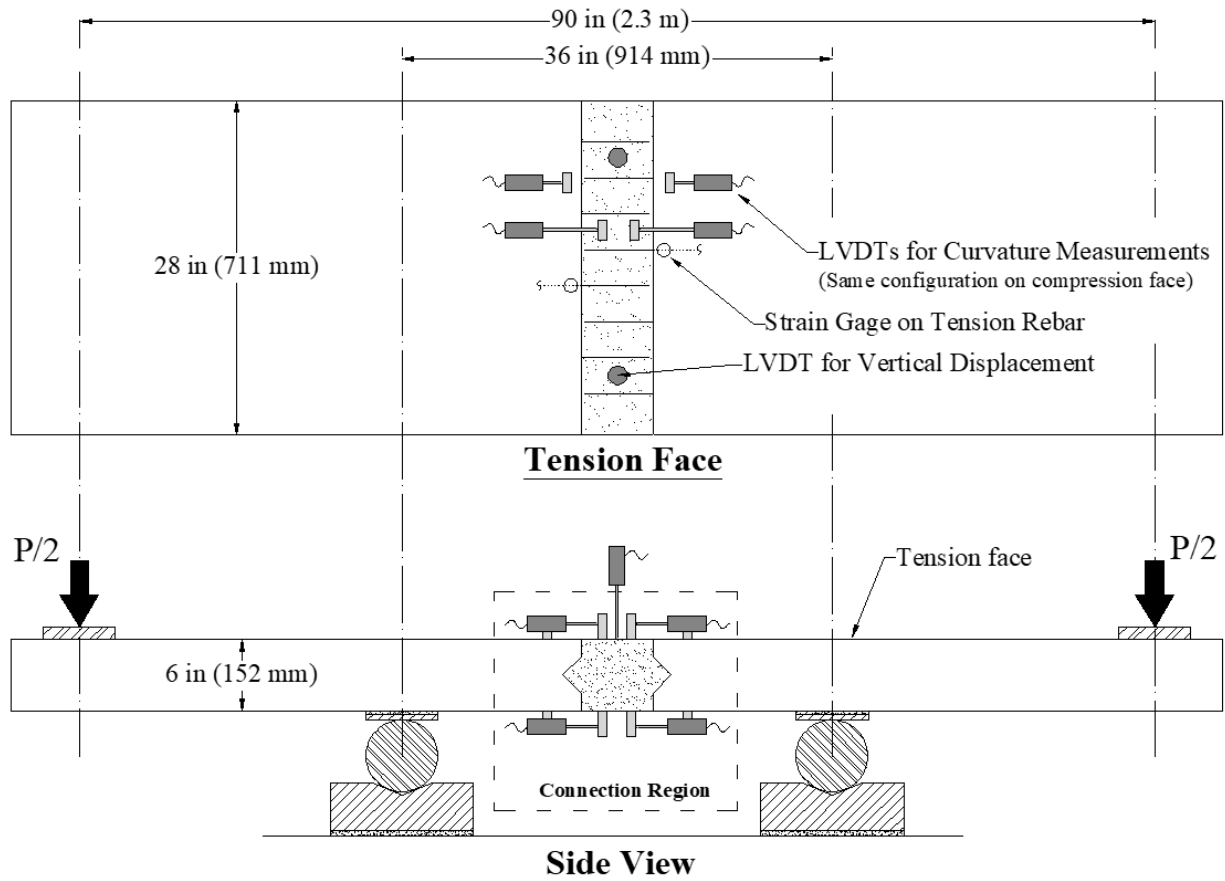
without measurement error from compliance of the test setup and load frame. The third strain gage, denoted “SG C,” was installed on the bottom face of the specimen (compression face as tested) to measure concrete strain.



Source: FHWA

Figure 37. Illustration. Instrumentation plan for deck-level connection tests (excluding U-bar tests).

The instrumentation plan used for the specimens with U-bars (G1-8.5-UB-EA-Tr-T-73 and G11C-8.5-UB-EA-Tr-T-74) and for the single specimen with U2 grout (U2-5.5-B-EA-Tr-75) is shown in figure 38. This instrument plan contains some slight differences from that shown in figure 37. These specimens were instrumented with ten LVDTs and two foil-backed electrical resistance strain gages. Each interface location was instrumented with four LVDTs to capture curvature over the interface and within the adjacent precast concrete deck panel. Two vertical LVDTs, mounted on a load spreader beam, were used to capture the vertical deflection of the specimen at mid-span. Strain gages were installed on a single tension reinforcing bar within each individual precast panel element.



Source: FHWA

Figure 38. Illustration. Instrumentation plan for deck-level connection specimens employing U-bars.

Both instrumentation plans included displacement and load measurements captured from the actuator used to load specimens.

BOND CHARACTERIZATION TEST SPECIMENS

Test Matrix

Bond characterization tests were primarily intended to complement deck-level connection testing to further investigate the tensile bonding strength of the concrete-grout interface. Thus, the test matrix for bond characterization specimens was developed to provide parameter combinations similar to those investigated in deck panel connection tests. The bond characterization test matrix is presented in table 13. Bond tests investigated how grout type and precast concrete surface preparation affected bond performance. Thus, table 13 identifies which tests were conducted for different grout and surface preparation combinations. Details regarding test methods and testing frequency are presented in Chapter 4.

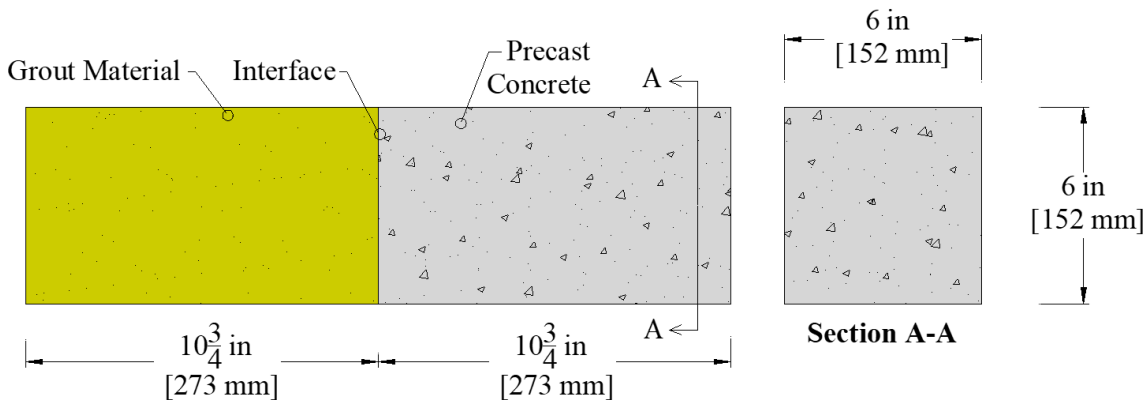
Table 13. Specimen matrix for bond characterization tests.

Surface Preparation	G1	M1	E1	U2
PW	F, C, S	F, C, S	F, C, S	F, C, S
PW+E1	-	-	-	-
PW+E2	F, C	-	-	-
SB	F, C, S	F, C, S	F, C, S	F, C, S
SB+E1	-	-	-	F, C, S
SB+E2	-	-	-	-
EA	F, C, S	F, C, S	F, C, S	F, C, S

F = Flexural Beam
 C = Splitting Cylinder
 S = Slant Shear
 - = Variable set not tested

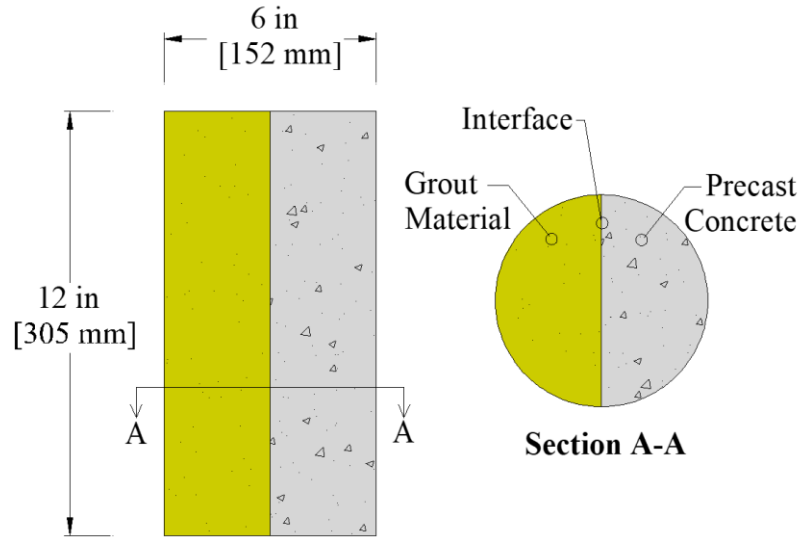
Specimen Details

As noted previously, the three different bond characterization tests were based on currently available ASTM standards: ASTM C78, *Standard Test Method for Flexural Strength of Concrete (Using Simple Beam with Third-Point Loading)* for the flexural beam test; ASTM C496, *Standard Test Method for Splitting Tensile Strength of Cylindrical Concrete Specimens* for the splitting cylinder bond test; and ASTM C882, *Standard Test Method for Bond Strength of Epoxy-Resin Systems Used with Concrete by Slant Shear* for the slant shear test. These standards were used as a reference for both specimen details and geometry as well as for loading protocols (described in Chapter 3). Figure 39 through figure 41 depict the specimen details for the flexural beam, splitting cylinder, and slant shear bond test specimens, respectively.



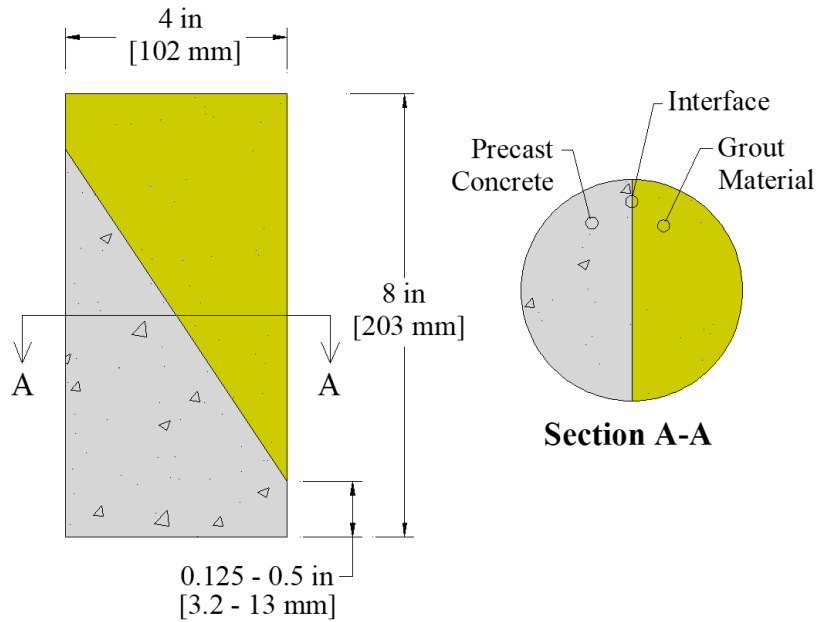
Source: FHWA

Figure 39. Illustration. Flexural beam bond test specimen details.



Source: FHWA

Figure 40. Illustration. Splitting cylinder bond test specimen details.



Source: FHWA

Figure 41. Illustration. Slant shear bond test specimen details.

Construction

The formwork for beam, splitting cylinder, and slant shear bond test specimens are shown in figure 42 through figure 44, respectively. Each specimen consisted of a precast concrete half and a grout half. The first step in the construction process of the bond test specimens was casting the concrete half using the same concrete mix that was used for deck panel specimens (table 12). For

the beam and split cylinder specimens, two concrete halves were cast simultaneously. For the slant shear specimens, each single half was cast at a time. The concrete was allowed to cure for at least 24 hours prior to removal of the molds.



Source: FHWA

Figure 42. Photo. Formwork for flexural beam bond test specimens.



Source: FHWA

Figure 43. Photo. Formwork for splitting cylinder bond test specimens.



Source: FHWA

Figure 44. Photo. Formwork for slant shear bond test specimens.

Prior to casting grout, surfaces that were to be in contact with grout were prepared using the precast concrete surface preparation techniques described previously. After surface preparation, specimen halves were placed back into molds in preparation for grout placement as shown in figure 45. Grouting of bond test specimens was concurrent with casting the connection grout in deck-level connection specimens.



Source: FHWA

Figure 45. Photo. Bond characterization specimens prepared for grout placement.

Instrumentation

There was no external instrumentation used on bond test specimens. All measurements taken during bond tests were either recorded directly from the load frame or were observed through visual indications.

CHAPTER 4. BOND CHARACTERIZATION TESTING

INTRODUCTION

The bond characterization test results are discussed in this chapter. Prior to discussing results, the testing procedure for each test is discussed along with relevant information from the ASTM standards used to determine the loading protocol for each test. Results are discussed individually for each test method, and include observed failure modes and relationships between bond strength, surface preparation, and grout material. An overall assessment of bond performance in relation to the test variables is provided at the end of the chapter along with an assessment of each of the three test methods.

TEST PROCEDURES

Bond tests were performed according to ASTM standard test methods C78, C496, and C882 for flexural beam, splitting cylinder, and slant shear bond tests, respectively. (ASTM C78/C78M-16, 2016; ASTM C496/C496M-11, 2004; ASTM C882/C882M-13a, 2013) Tests were completed after 1 and 7 days of grout curing, and a final test, which is denoted as the “28+ Day” test, was also completed prior to and after testing deck panel specimens with similar grout and surface preparation characteristics. It should be noted that the age of concrete at the time of testing was typically greater than 28 days. Three specimens were tested for each set of experimental variables. In some cases, multiple sets of specimens with the same variable configurations were tested. For such cases, the results presented are the minimum recorded strengths. After testing, photos were taken to document the failure modes exhibited by each specimen.

Flexure Beam Tests

Flexural beam bond tests were conducted according to ASTM C78, *Standard Test Method for Flexural Strength of Concrete (Using Simple Beam with Third-Point Loading)* as shown in figure 46. Prior to testing, cross-section dimensions were measured and recorded at the concrete-grout interface. Specimens were loaded in third-point bending with a shear span of 6 inches (153 mm). Load was applied at a rate that constantly increased the extreme fiber stress between 125 and 175 psi/min (0.86 and 1.21 MPa/min) until rupture occurred. The corresponding loading rate was determined using the equation shown in figure 47 and was approximately between 1,500 and 2,100 lb/min (20 and 28 kN/min). After failure, the maximum load and the crack distance from the concrete-grout interface (mid-span) were recorded.



Source: FHWA

Figure 46. Photo. Flexural beam bond testing (based on ASTM C78).

$$r = \frac{Sbd^2}{L}$$

Figure 47. Equation. Loading rate equation for flexural beam bond testing.

Where

r = loading rate, lb/min

S = rate of increase in extreme fiber stress, psi/min

b = average width of the specimen, in

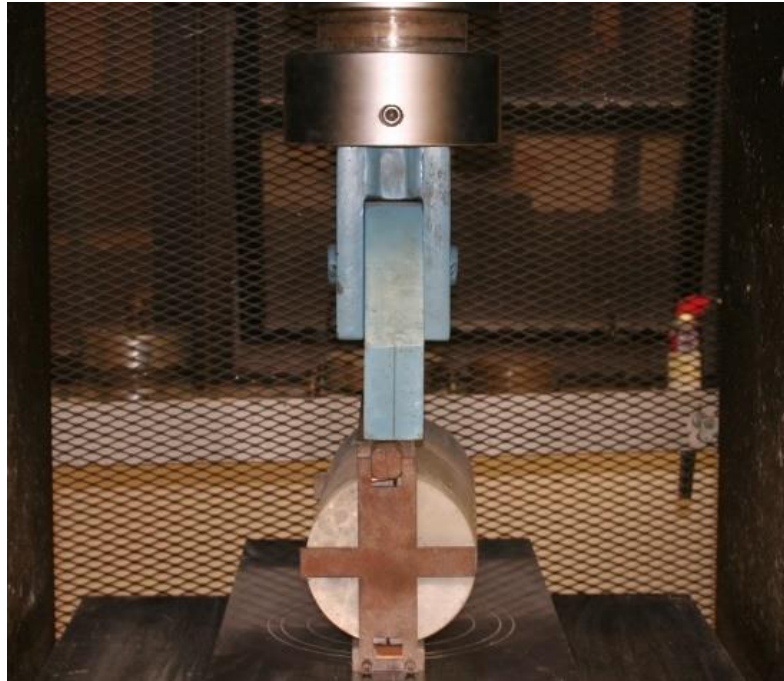
d = average depth of the specimen, in

L = span length, in

Splitting Cylinder Tests

Splitting cylinder bond tests were conducted according to ASTM C496, *Standard Test Method for Splitting Tensile Strength of Cylindrical Concrete Specimens* as shown in figure 48. Prior to testing, cross-section dimensions were measured and recorded at three locations along the length of the cylinder. Splitting cylinder specimens were loaded to increase the splitting tensile stress at a constant rate of 100 to 200 psi/min (0.7 to 1.4 MPa/min) until failure. The corresponding

loading rate was determined using the equation shown in figure 49 and was approximately between 190 and 380 lb/min (0.845 and 1.69 kN/min). After failure, the maximum load was recorded.



Source: FHWA

Figure 48. Photo. Splitting cylinder bond testing (based on ASTM C496) prior to specimen alignment.

$$r = \frac{f_{st}\pi ld}{2}$$

Figure 49. Equation. Loading rate equation for splitting cylinder tests.

Where

r = loading rate, lb/min

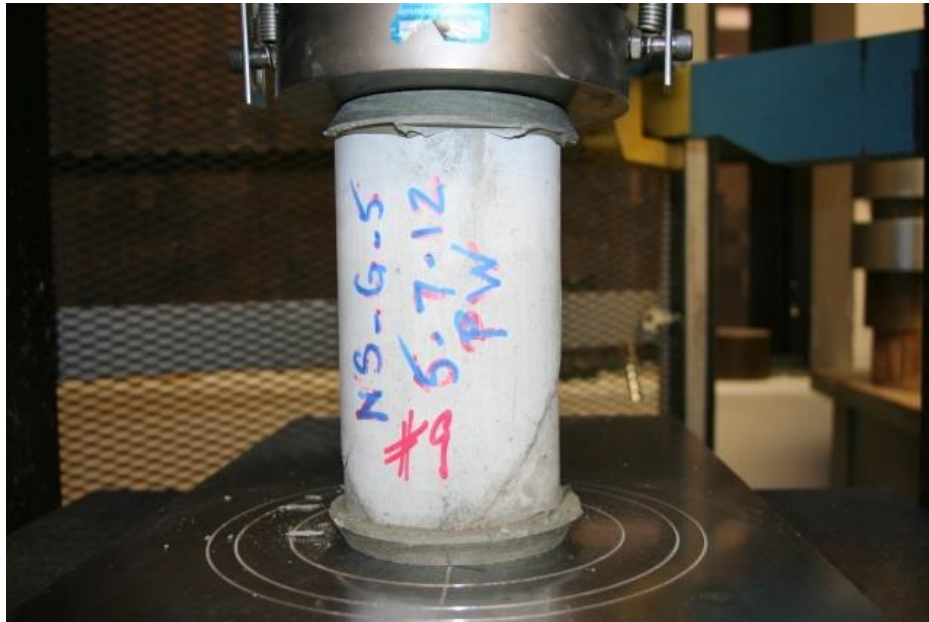
f_{st} = splitting tensile stress, psi

d = cylinder diameter, in

l = cylinder length, in

Slant Shear Tests

Slant shear bond tests were conducted according to ASTM C882, *Standard Test Method for Bond Strength of Epoxy-Resin Systems Used with Concrete by Slant Shear*, as shown in figure 50. Prior to testing, cross-section dimensions were measured and recorded at three locations along the length of the cylinder. Slant shear specimens, as stated in ASTM C882, were loaded according to ASTM C39, *Test Method for Compressive Strength of Cylindrical Concrete Specimen*. Load was applied such that the stress rate on the specimen was 35 ± 7 psi/sec [0.25 ± 0.05 MPa/sec]. The corresponding loading rate was between 350 and 530 lb/sec (1.56 and 2.36 kN/min). After failure, the maximum load was recorded.



Source: FHWA

Figure 50. Photo. Slant shear bond testing (Based on ASTM C882).

COMPRESSIVE PROPERTIES OF CONCRETE AND GROUT

Compressive strengths of concrete and grout were measured throughout the duration of the experimental program. Compression tests were typically conducted at 1, 7, and 28 days after casting, and tests were also completed prior to and after testing the deck-level connection (denoted “28+”). The compressive strength of the concrete was determined using 6-inch by 12-inch (152-mm by 305-mm) cylinders that were cast and tested in accordance with ASTM C39. The compressive strengths of the G1, M1, and E1 grouts were measured using 2-inch (50-mm) square cube specimens cast and tested in accordance with ASTM C109. The compressive strength of the U2 grout was measured using 3-inch by 6-inch (76-mm by 152-mm) cylinders tested in accordance with ASTM C39 with exception of the loading rate. Due to high compressive strength, U2 cylinders were loaded more rapidly than as specified in ASTM C39. The cylinders were loaded at a rate between 50–150 psi/sec (0.34–1.03 MPa/sec), which

corresponds to 353–1060 lb/sec (1.57–4.72 kN/sec). Research has indicated that the aforementioned loading rate range does not have a significant effect on the compressive properties of the U2 grout. (Graybeal 2014) ASTM has since published standard C1856, *Standard Practice for Fabricating and Testing Specimens of Ultra-High Performance Concrete*, which includes the faster loading rates mentioned above. (ASTM C1856/C1586-17, 2017, 18) The average compressive strengths of conventional concrete and G1, M1, E1, and U2 grouts are listed in table 14 through table 18, respectively.

Table 14. Measured compressive strength of concrete.

Age (Days)	Average Compressive Strength, psi (MPa)		Standard Deviation, psi (MPa)		Coefficient of Variation	Number of Cylinder Tests Included
1	2,417	(16.7)	711	(4.90)	0.294	42
7	3,580	(24.7)	46	(0.32)	0.013	3
28	6,700	(46.2)	953	(6.56)	0.142	45
28+	7,872	(54.2)	1,229	(8.47)	0.156	96

Table 15. Measured compressive strength of G1 grout.

Age (Days)	Average Compressive Strength, psi (MPa)		Standard Deviation, psi (MPa)		Coefficient of Variation	Number of Cube Tests Included
1	4,362	(30.1)	743	(5.12)	0.170	27
7	7,092	(48.9)	744	(5.12)	0.105	36
28	8,617	(59.4)	127	(0.87)	0.015	9
28+	9,958	(68.6)	1,518	(10.5)	0.152	66

Table 16. Measured compressive strength of M1 grout.

Age (Days)	Average Compressive Strength, psi (MPa)		Standard Deviation, psi (MPa)		Coefficient of Variation	Number of Cube Tests Included
1	4,812	(33.2)	343	(2.36)	0.071	15
7	5,940	(40.9)	754	(5.19)	0.127	18
28	6,392	(44.0)	562	(3.87)	0.088	18
28+	7,827	(53.9)	300	(2.06)	0.038	9

Table 17. Measured compressive strength of E1 grout.

Age (Days)	Average Compressive Strength, psi (MPa)	Standard Deviation, psi (MPa)	Coefficient of Variation	Number of Cube Tests Included
1	11,353 (78.2)	1,044 (7.19)	0.092	27
7	13,882 (95.6)	700 (4.82)	0.050	27
28	^a	^a	^a	^a
28+	14,236 (98.1)	789 (5.44)	0.055	54

^a 28-day testing not conducted

Table 18. Measured compressive strength of U2 grout.

Age (Days)	Average Compressive Strength, psi (MPa)	Standard Deviation, psi (MPa)	Coefficient of Variation	Number of Cylinder Tests Included
1	8,924 (61.5)	2,195 (15.1)	0.246	24
7	17,314 (119.3)	2,292 (15.8)	0.132	27
28	22,810 (157.2)	341 (2.35)	0.015	3
28+	22,454 (154.7)	1,694 (11.7)	0.075	39

TEST RESULTS

Flexure Tests

Flexural beam bond test specimens exhibited three distinct failure modes. Mode 1, shown in figure 51, represents the case where a poor bond existed between concrete and grout. Mode 1 failure was governed by bond failure at the interface of the two materials. Specimens that failed in this mode had little to no tensile bond resistance. Mode 2, shown in figure 52, was characterized by a failure surface that exhibited a combination of interface bond failure and tensile rupture of the bonded materials. This case indicates inconsistent bond across the interface but improved tensile resistance compared with specimens exhibiting Mode 1 failure. Mode 3, shown in figure 53, represents the case where the bond between the two materials was strong, and the tensile capacity of one material was reached.



Source: FHWA

Figure 51. Photo. Failure of flexural beam bond test specimens: Mode 1 – bond failure.



Source: FHWA

Figure 52. Photo. Failure of flexural beam bond test specimens: Mode 2 – partial substrate failure.



Source: FHWA

Figure 53. Photo. Failure of flexural beam bond test specimens: Mode 3 – substrate/grout failure.

Table 19 provides a list of the observed failure modes with respect to grout materials, grout material age, and surface preparation method. In some cases, the failure mode is denoted as HF, which indicates that failure occurred during handling, prior to loading, and exhibited Mode 1 failure. From a qualitative perspective, table 19 shows that using an exposed aggregate (EA) surface preparation can improve the bond between the concrete and the grout material. Other than the epoxy grout (E1) specimens, which exhibited good bond regardless of surface preparation, the pressure washing (PW) and sand blasting (SB) surface preparations did not improve bonding between the substrate concrete and the field-cast grout.

Table 19. Observed failure modes in flexural beam bond tests.

Bonded Material	Grout Age (Days)	PW	SB	PW+Ep	SB+Ep	EA
G1	1	NT	NT	NT	NT	NT
	7	HF	HF	NT	NT	Mode 2
	28+	HF	HF	Mode 1	NT	Mode 2
M1	1	Mode 1	Mode 1	NT	NT	Mode 2
	7	Mode 1	Mode 1	NT	NT	Mode 2
	28+	NT	HF	NT	NT	Mode 2
E1	1	Mode 2 & 3	Mode 2 & 3	NT	NT	Mode 3
	7	Mode 2 & 3	Mode 2 & 3	NT	NT	Mode 2 & 3
	28+	Mode 2	Mode 2 & 3	NT	NT	NT
U1	1	Mode 1	Mode 1	NT	Mode 1	Mode 3
	7	Mode 1	Mode 1	NT	NT	Mode 3
	28+	Mode 1	Mode 1	NT	NT	Mode 3

HF = Indicates failure occurred during handling.

NT = indicates a variable combination that was not tested.

The average flexural tension strength, f_{ft} , was determined in accordance with flexural beam bond tests using the equation shown in figure 54. The results for grouts G1, M1, E1, and U2 are presented in figure 55 through figure 58, respectively; the error bars indicate +/- one standard deviation from the mean.

In general, G1 and M1 grouts exhibited low bond strengths to concrete regardless of surface preparation and age. For PW and SB surface preparations, these grouts sustained less than 15 percent of the average tensile strength of plain concrete prior to failure, and in many cases, specimens broke apart during handling. The bond performance of epoxy grout (E1) was superior to that of the other grout materials investigated. The majority of E1 specimens failed within the precast concrete portion away from the bond line, which indicates a sound bond. Furthermore, bond strength did not appear to be significantly affected by surface preparation. Specimens cast with UHPC (U2) as the grout material exhibited good bond performance using the exposed aggregate (EA) surface preparation. Failure of these specimens typically occurred within the precast concrete with the exception of tests conducted after one day of grout curing, which typically failed within the U2 grout. The use of sand blasting showed improved bond performance in U2 specimens compared with pressure washing. However, the bond strength was still poor compared with the EA surface preparation.

$$f_{ft} = \frac{PL}{bd^2}$$

Figure 54. Equation. Flexural tension strength as determined by third-point loading.

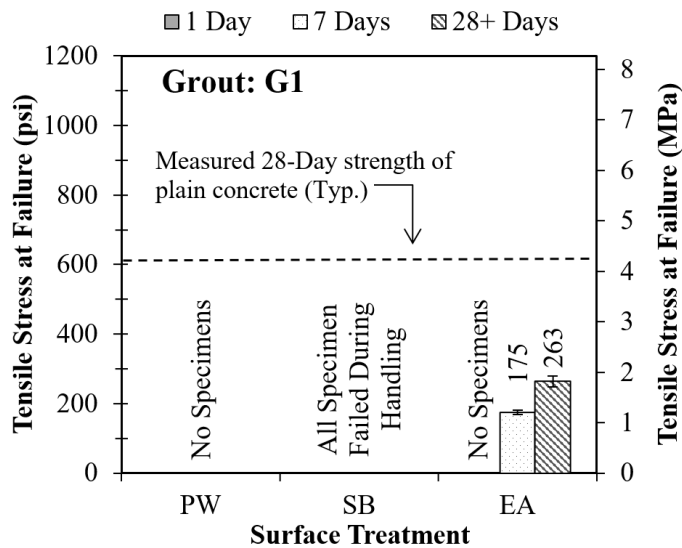
Where

P = maximum applied load

L = simply-supported length of the beam

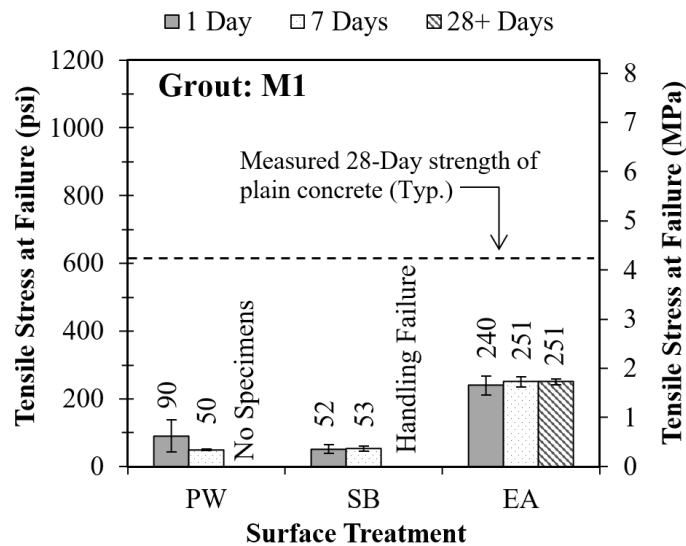
b = beam width

d = beam depth



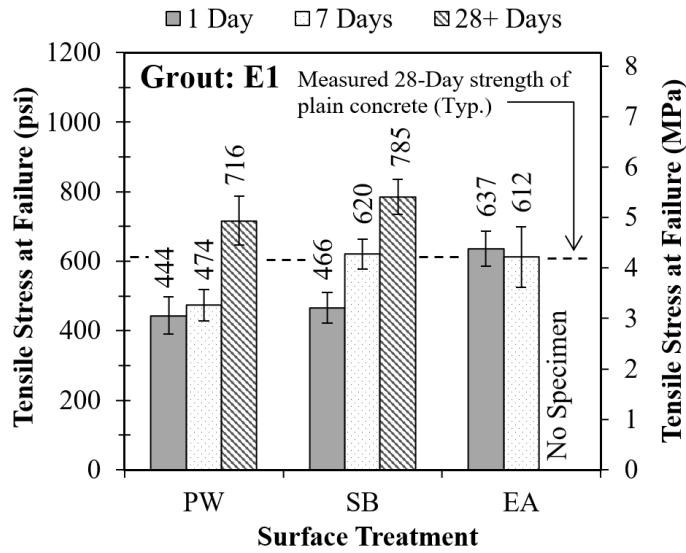
Source: FHWA

Figure 55. Graph. Average tensile strength flexural beam bond tests with G1 grout.



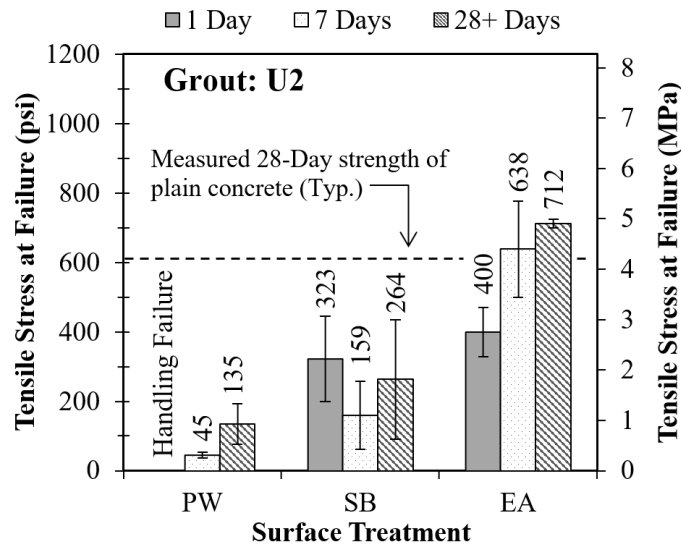
Source: FHWA

Figure 56. Graph. Average tensile strength flexural beam bond tests with M1 grout.



Source: FHWA

Figure 57. Graph. Average tensile strength flexural beam bond tests with E1 grout.

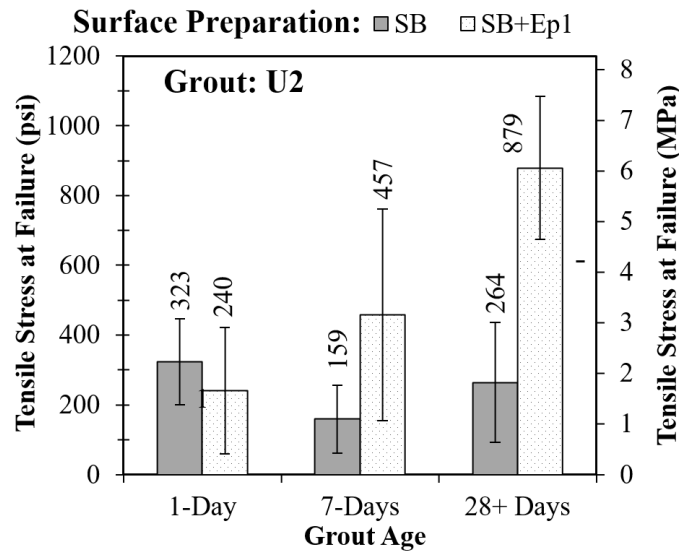


Source: FHWA

Figure 58. Graph. Average tensile strength flexural beam bond tests with U2 grout.

Beam specimens were also tested using epoxy bonding agents to promote the bond between grout and precast concrete. These results are shown in figure 59. Two grout-surface preparation combinations were investigated: G1 grout with PW surface preparation and epoxy 2 (G1-PW-Ep2), and U2 grout with SB surface preparation and epoxy 1 (U2-SB-Ep1). Results for the G1-PW-Ep2 configuration were mixed. After 28 days, the G1-PW-Ep2 system exhibited some tensile resistance, 95 psi (0.65 MPa), but the resistance was still significantly lower than the measured flexural tension strength of the concrete. All of these specimens tested after 42 days

failed during handling. Results for the U2-SB-Ep1 configuration showed that the average bond strength significantly increased after seven days compared to the same specimen configuration without the epoxy coating.



Source: FHWA

Figure 59. Graph. Average tensile strength from flexural beam bond tests with epoxy bonding agents using U2 grout.

Splitting Cylinder Tests

Similar to flexural beam bond tests, splitting cylinder specimens exhibited three distinct failure modes. These modes were the same as those described for flexural beam tests, and are shown in figure 60 through figure 62. Table 20 provides a list of observed modes for the different specimen configurations. With the exception of specimens cast with an epoxy grout, specimens with PW and SB surface preparations failed by debonding (Mode 1), which indicates a poor bond between the precast concrete and the grout materials, regardless of grout material and age. Similar to flexural beam tests, EA surface preparation resulted in improved bond from the standpoint of failure mode. Furthermore, epoxy grout consistently exhibited a good bond to the concrete.



Source: FHWA

Figure 60. Photo. Failure of splitting cylinder bond test specimens: Mode 1 – bond failure.



Source: FHWA

Figure 61. Photo. Failure of splitting cylinder bond test specimens: Mode 2 – partial substrate failure.



Source: FHWA

Figure 62. Photo. Failure of splitting cylinder bond test specimens: Mode 3 – substrate/grout failure.

Table 20. Observed failure modes in splitting cylinder bond tests.

Bonded Material	Grout Age (Days)	PW	SB	PW+Ep	SB+Ep	EA
G1	1	Mode 1	Mode 1	NT	NT	Mode 2
	7	Mode 1	Mode 1	Mode 1	NT	Mode 2
	28+	Mode 1	Mode 1	Mode 1	NT	Mode 2
M1	1	Mode 1	Mode 1	NT	NT	Mode 2
	7	Mode 1	Mode 1	NT	NT	Mode 2
	28+	Mode 1	Mode 1	NT	NT	Mode 2
E1	1	Mode 1, 2, and 3	Mode 2 and 3	NT	NT	Mode 2 and 3
	7	Mode 2 and 3	Mode 2/3	NT	NT	Mode 2
	28+	NT	Mode 2/3	NT	NT	Mode 2
U1	1	Mode 1	Mode 1	NT	Mode 1	Mode 3
	7	Mode 1	NT	NT	NT	Mode 3
	28+	Mode 1	Mode 1	NT	NT	Mode 3

NT = indicates a variable combination that was not tested.

The average splitting tensile strength, f_{st} , was determined in accordance with splitting cylinder bond tests using the equation shown in figure 63. The results for grouts G1, M1, E1, and U2 are presented in figure 64 through figure 67; the error bars shown indicate +/- one standard deviation from the mean.

In most cases, the splitting tensile strength was not significantly affected by surface preparation method or grout age. For a given grout material, the splitting tensile strength for each surface preparation method were comparable. The cementitious grouts, G1 and M1, exhibited consistently lower strength compared with epoxy grout and UHPC. Exposed aggregate surface preparations for E1 and U2 marginally improved the measured bond strength. It is possible that

differential material stiffness influenced the results from the splitting tensile tests. This concept is discussed in detail later in the chapter.

$$f_{st} = \frac{2P}{\pi dl}$$

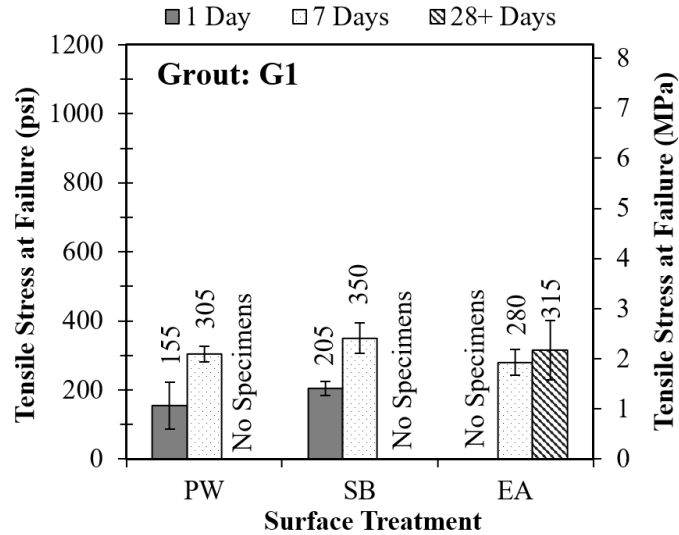
Figure 63. Equation. Splitting tensile strength.

Where

P = maximum applied load, kips

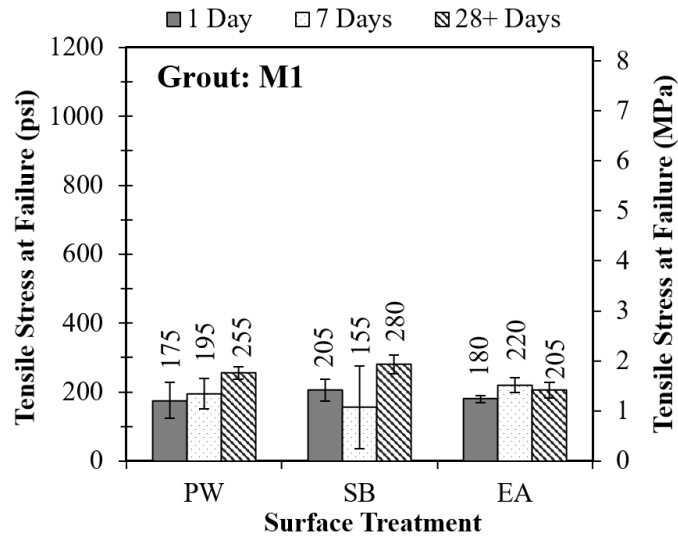
d = cylinder diameter, in

l = cylinder length, in



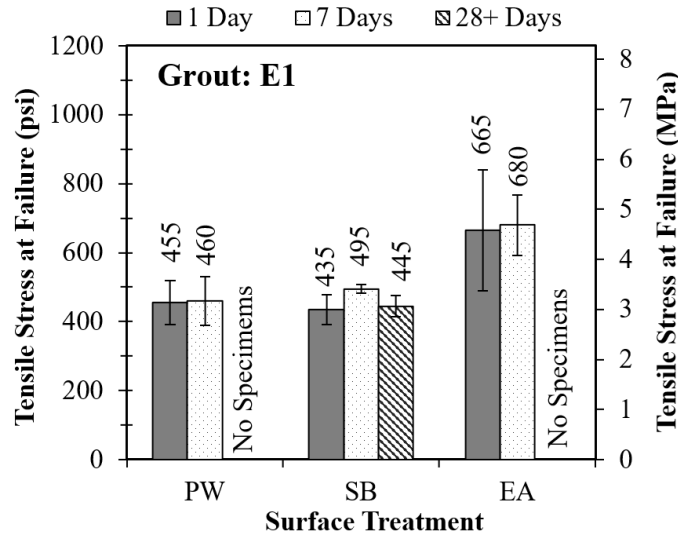
Source: FHWA

Figure 64. Graph. Average tensile strength from splitting cylinder bond tests with G1 grout.



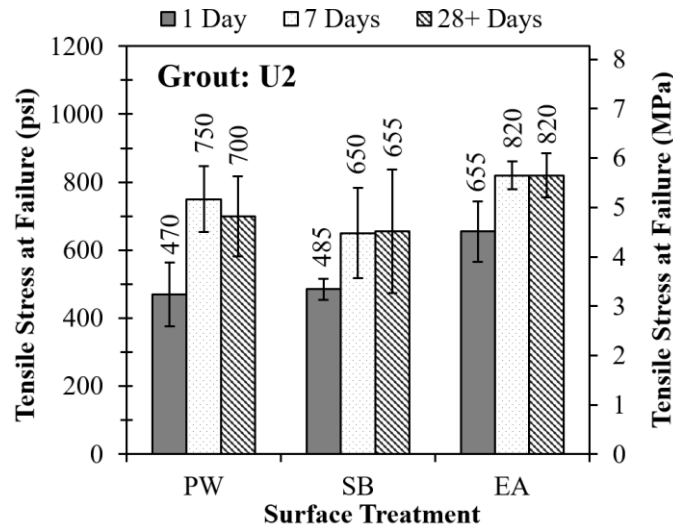
Source: FHWA

Figure 65. Graph. Average tensile strength from splitting cylinder bond tests with M1 grout.



Source: FHWA

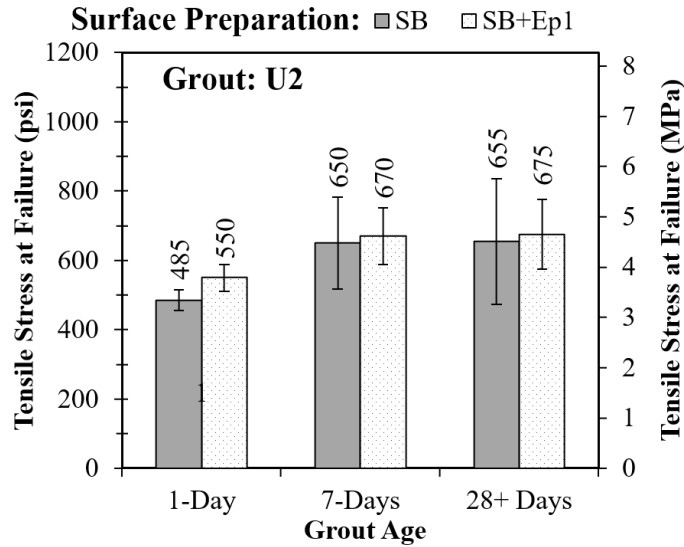
Figure 66. Graph. Average tensile strength from splitting cylinder bond tests with E1 grout.



Source: FHWA

Figure 67. Graph. Average tensile strength from splitting cylinder bond tests with U2 grout.

Splitting cylinder specimens were also tested using an epoxy bonding agent that was applied to the surface of precast concrete prior to casting grout. Similar to the flexural beam tests, only two grout-surface preparation combinations were investigated: G1 grout with PW surface preparation and epoxy 2 (G1-PW+Ep2), and U2 grout with SB surface preparation and epoxy 1 (U2-SB-Ep1). Both configurations, G1-PW+Ep2 and U2-SB+Ep1, produced results that were comparable to their counterparts without epoxy-coated precast concrete. For example, results for the U2 grout are shown in figure 68. Because the splitting cylinder tests did not exhibit significant distinction between the different surface preparations, it was difficult to assess whether epoxy coatings provided improved interface bond behavior.



Source: FHWA

Figure 68. Graph. Average splitting tensile strength from splitting cylinder bond tests with epoxy bonding agents.

Slant Shear Test

Figure 69 through figure 72 depict the different failure modes associated with slant shear bond tests. Modes 1 through 3 are the same as those defined for flexural beam and splitting cylinder bond tests. A fourth mode was required to identify specimens that failed by the crushing of concrete. This mode indicates excellent bond strength and was observed in specimens with EA surface preparation and E1 or U2 grouts (table 21). Similar to the other test methods, cementitious grouts (G1 and M1) and UHPC (U2) exhibited interface bond failure modes when PW and SB surface preparations were applied. Bond was improved in G1 and M1 by using exposed aggregate.



Source: FHWA

Figure 69. Photo. Failure of slant shear bond test specimens: Mode 1 – bond failure.



Source: FHWA

Figure 70. Photo. Failure of slant shear bond test specimens: Mode 2 – partial substrate failure.



Source: FHWA

Figure 71. Photo. Failure of slant shear bond test specimens: Mode 3 – substrate failure.



Source: FHWA

Figure 72. Photo. Failure of slant shear bond test specimens: Mode 4 – concrete crushing.

Table 21. Observed failure modes in slant-shear bond tests.

Bonded Material	Grout Age (Days)	PW	SB	PW+Ep	SB+Ep	EA
G1	1	Mode 1	Mode 1	Mode 1	NT	Mode 3
	7	Mode 1	Mode 1	NT	NT	NT
	28+	Mode 1	Mode 1	Mode 1	NT	Mode 3
M1	1	Mode 1	Mode 1	NT	NT	Mode 2
	7	Mode 1	Mode 1	NT	NT	Mode 2
	28+	Mode 1	Mode 1	NT	NT	Mode 1
E1	1	Mode 1 and 2	Mode 2	NT	NT	Mode 4
	7	Mode 1 and 2	Mode 1 and 2	NT	NT	Mode 4
	28+	Mode 1	Mode 1 and 2	NT	NT	Mode 3 and 4
U1	1	Mode 1	Mode 1	NT	Mode 1	Mode 4
	7	Mode 1	NT	NT	NT	Mode 4
	28+	Mode 1	Mode 1	NT	Mode 1	Mode 4

NT = indicates a variable combination that was not tested.

The slant shear bond strength, τ_{slant} , was determined using the equation shown in figure 73. The results for grouts G1, M1, E1, and U2 are presented in figure 74 through figure 77, respectively; error bars shown indicate +/- one standard deviation from the mean.

Specimens grouted with G1 or M1 grout and employing PW and SB surface preparations exhibited low bond strengths compared with specimens employing E1 and U2 grouts. Swenty and Graybeal (2013) showed that the concrete-to-concrete slant shear bond strength with SB surface preparation at 28 days was 680 psi (4.1 MPa) for concrete comparable to that used in this

study. The majority of specimens with G1 and M1 grout and PW and SB surface preparations had bond strengths that were lower than 680 psi (4.1 MPa). The use of exposed aggregate significantly improved the apparent bond strength. However, this is somewhat misleading. When aggregate is exposed, a significant portion of slant shear strength can be attributed to aggregate interlock and shear friction, which is described in more detail within the following sections. (Nilson, Darwin, and Dolan 2010)

$$\tau_{slant} = \frac{P \cos \theta}{A_{slant}}$$

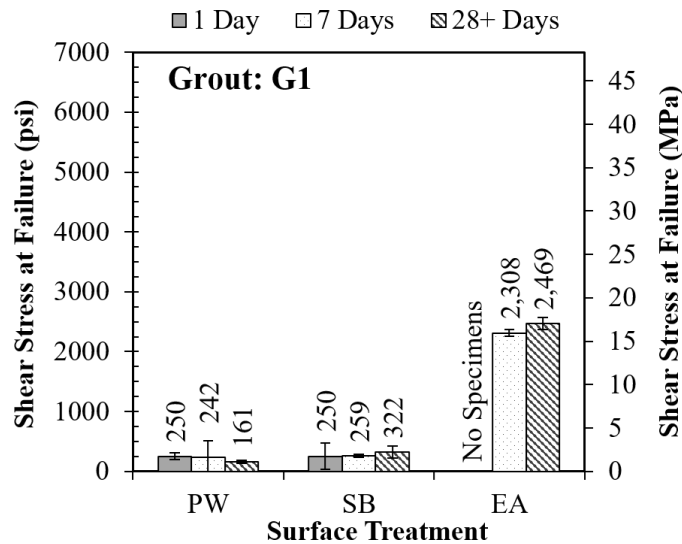
Figure 73. Equation. Slant shear bond strength.

Where

P = maximum applied load, kips.

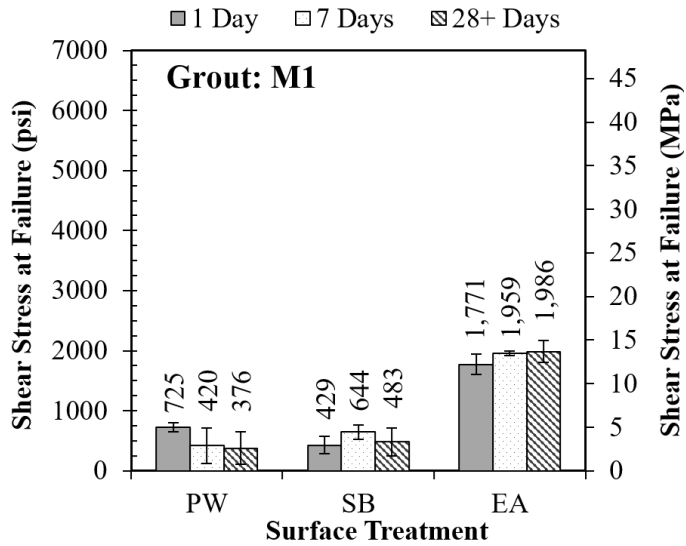
θ = slant angle, deg.

A_{slant} = area of the elliptical slant cut, in².



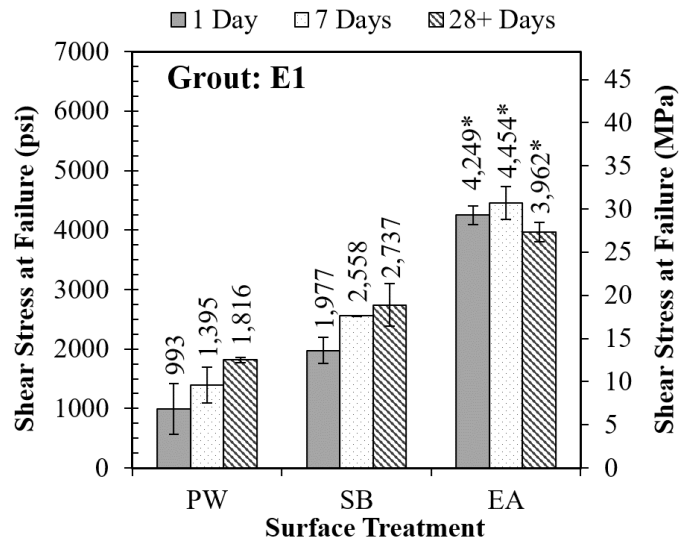
Source: FHWA

Figure 74. Graph. Average shear stress at failure for slant shear bond tests with G1 grout.



Source: FHWA

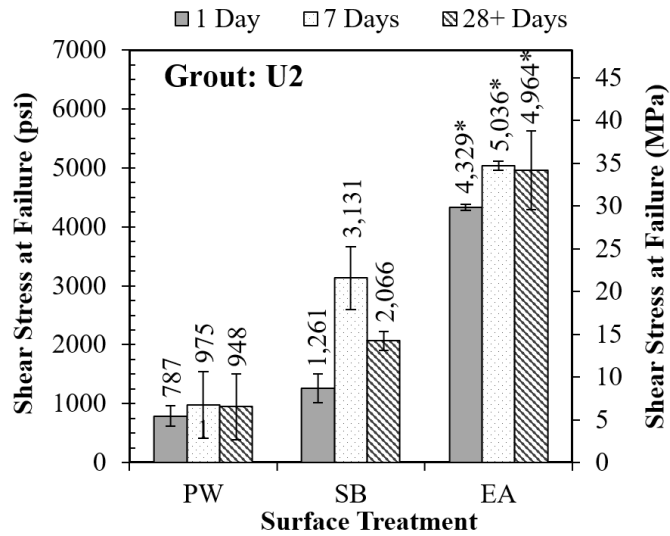
Figure 75. Graph. Average shear stress at failure for slant shear bond tests with M1 grout.



* Specimens failed as a result of concrete crushing.

Source: FHWA

Figure 76. Graph. Average shear stress at failure for slant shear bond tests with E1 grout.

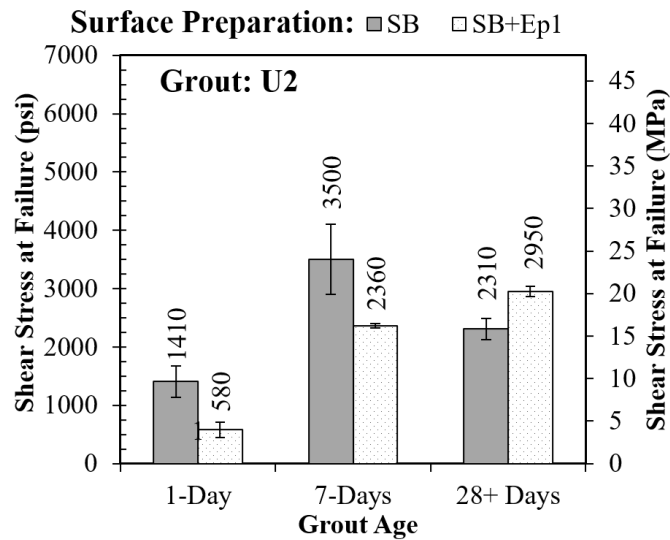


* Specimens failed as a result of concrete crushing.

Source: FHWA

Figure 77. Graph. Average shear stress at failure for slant shear bond tests with U2 grout.

A single group of U2 specimens were tested where epoxy bonding agents were applied to the precast concrete prior to casting grout: U2 grout with SB surface preparation and epoxy 1 (U2-SB-Ep1). These results are shown in figure 78. Average bond strengths after 1, 7, and 84 days were 580 psi (3.99 MPa), 2,360 psi (16.3 MPa), and 2,950 psi (20.3 MPa), respectively. At 1 and 7 days, average shear bond strengths were significantly lower than the counterpart specimens without epoxy. The average 84-day result was 27 percent greater than the bond strengths of the counterparts without epoxy-coated precast concrete.



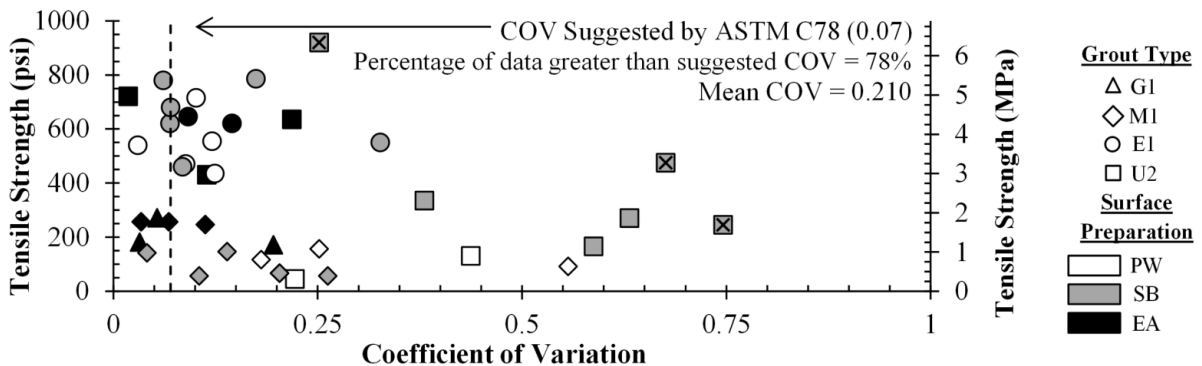
Source: FHWA

Figure 78. Graph. Average shear strength from slant shear bond tests with epoxy bonding agents.

Comparison of Test Methods

One goal of the bond characterization tests was to evaluate the applicability of each test method for assessing bond strength between precast concrete and grout materials. This includes variability in test results, consistency between methods, and suggestions for future use. Figure 79 through figure 81 compare the coefficient of variation (COV) among the three test methods. For each test method, the suggested COV for the corresponding ASTM standard test is shown for reference. However, it should be kept in mind that the ASTM standard tests and the tests performed in this study examine different properties. Each plot lists the percentage of data that is greater than the ASTM-suggested COV and the mean COV for a given test.

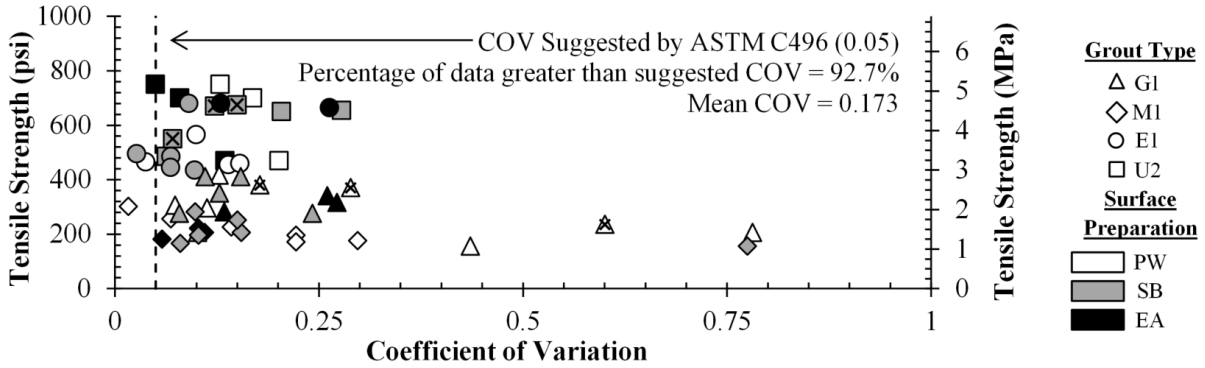
In general, all three test methods exhibited significant scatter characterized by a wide range of COV values. The mean COV for the flexural beam, splitting cylinder, and slant shear bonds tests were 21 percent, 17.3 percent, and 22.9 percent, respectively. The flexural beam and splitting cylinder tests had mean COVs that were significantly larger than the corresponding ASTM standard test method, which is not unexpected given that the test objectives are different. The majority of COV data for slant shear bond tests was less than the suggested COV for ASTM C882. However, the bond test conducted in this study and C882 are more similar in nature than the other bond tests and the ASTM counterparts.



Note: An “X” over a data point marker indicates the use of an epoxy surface coating on precast concrete.

Source: FHWA

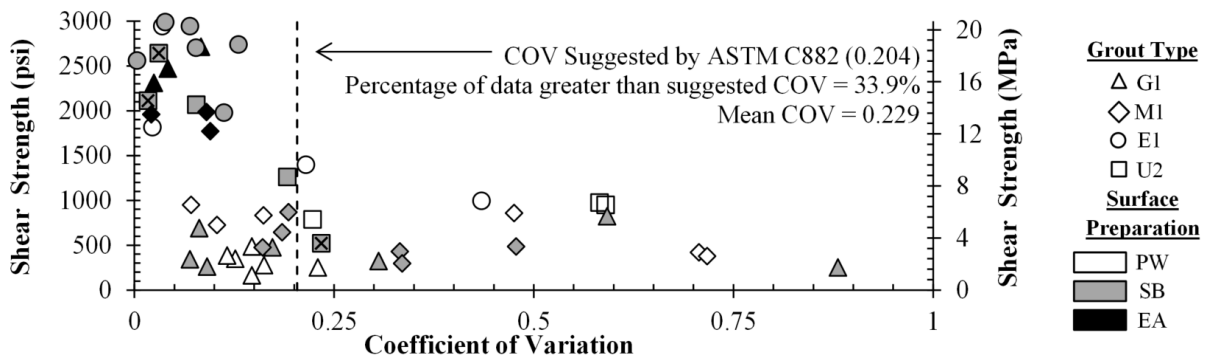
Figure 79. Graph. Coefficient of variation for flexural beam bond tests.



Note: An “X” over a data point marker indicates the use of an epoxy surface coating on precast concrete.

Source: FHWA

Figure 80. Graph. Coefficient of variation for splitting cylinder bond tests.



Notes: An “X” over a data point marker indicates the use of an epoxy surface coating on precast concrete; Data only reflects specimens that exhibited bond failure.

Source: FHWA

Figure 81. Graph. Coefficient of variation for slant shear bond tests.

Consistency between the test methods can be evaluated by comparing the trends observed between the three tests. Flexural beam and slant shear tests both indicated that as the precast concrete surface roughness increased there was an increase in bond performance. That is, the EA surface preparation exhibited a superior bond compared to PW and SB preparations for a given grout type. This was not the case in the splitting cylinder tests, which showed that for a given grout material, tensile strength was not highly dependent on surface preparation; this contradicts the results from the other tests.

The calculated tensile resistance f_{st} from the splitting cylinder test assumes a uniform stress distribution across the vertical center line, which is similar to that “true” stress distribution away from the load points as described by Borelli and Chong (2000). If the elastic modulus of the two halves differed significantly, the stress and strain fields across the interface could be affected, resulting in uneven distributions of stress and strain across the interface. This would compromise

the validity of the approximate tensile calculated using the equation shown in figure 63. There are two situations where the stiffness difference between the two halves could be significant:

1. *One mature half and early-age half:* If the precast concrete half was hardened and had matured longer than 28 days, and a grout half was cast and allowed to cure for 24 hours, there could be a significant difference in stiffness.
2. *Halves with different characteristic material properties:* If conventional concrete was used for one half and a material with a higher stiffness, such as UHPC, was used for the second half, there could be a large differential in stiffness.

A simple 2D linear-elastic finite-element (FE) model was created using Abaqus CAE, a commercially-available finite-element software package, to investigate the effect of material stiffness on the stress distribution across the interface. Figure 82 shows a representation of the FE model and the material properties for the two cases investigated. Case 1 represents a cylinder of uniform material or two materials with similar elastic moduli. In Case 2, the elastic modulus of the right-hand material, E_2 , has been doubled. This case is representative of a cylinder comprised of conventional concrete and UHPC and cured for 28 days based on the properties similar to those determined by Swenty and Graybeal (2013).

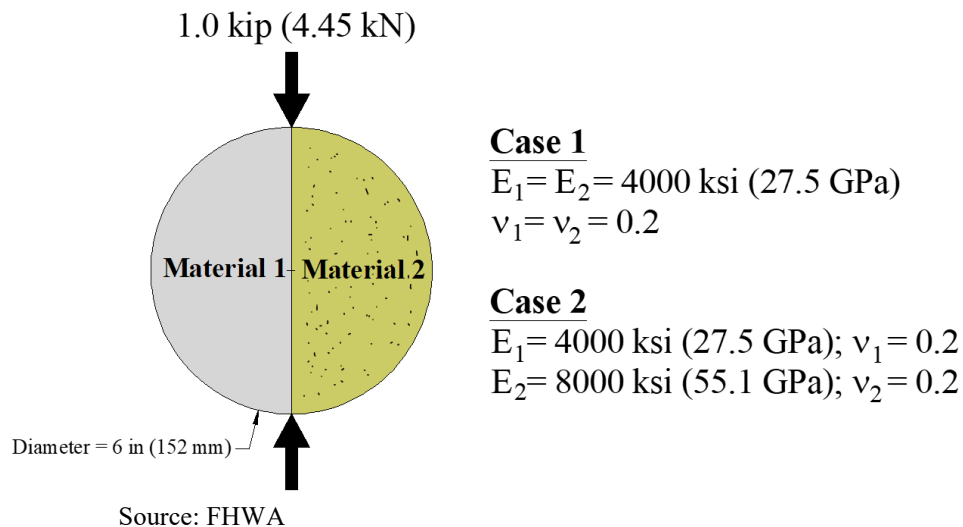
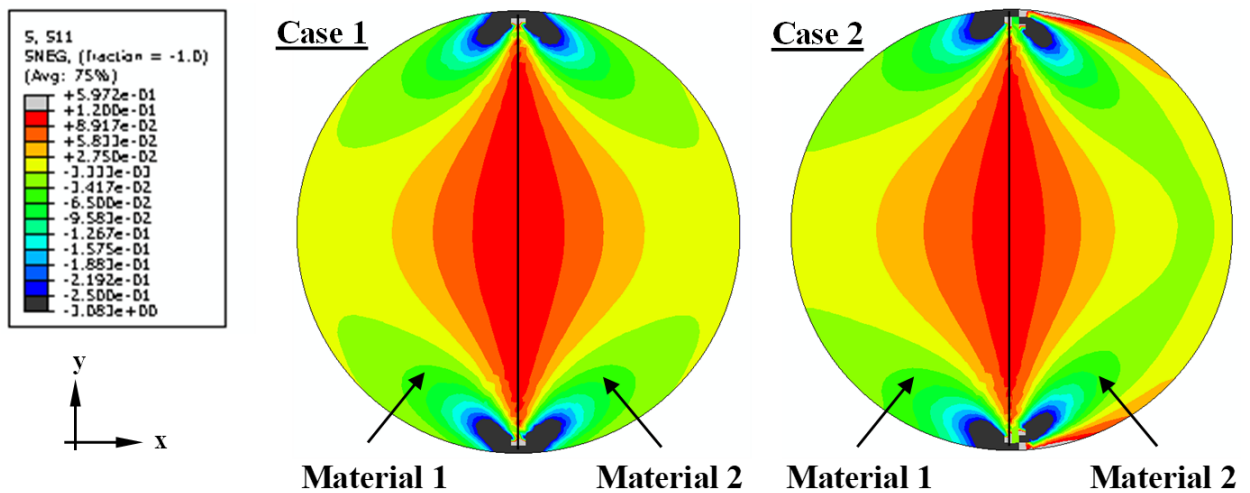


Figure 82. Illustration. Splitting cylinder bond test finite-element model and material properties.

Figure 83 shows the stress contours from the two cases investigated. Contour plots depict the stress in the x direction, σ_x , which corresponds to tensile stress across the interface. It can be observed that the stress distribution is indeed non-uniform, and it could potentially become more distorted as materials become locally nonlinear. The difference between the calculated stress using the equation shown in figure 63 and the average stress along the centerline of the Case 1 and 2 cylinders was 0.5 percent and 5.84 percent, respectively. Additionally, local stiffness differences could act as stress risers that serve to expedite initiation of tensile cracks near the

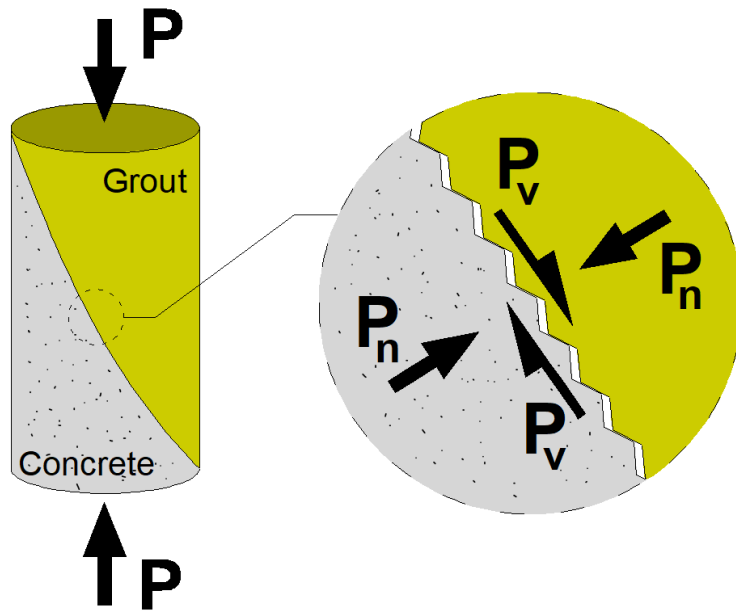
loading points. It is evident that differential material stiffness could influence the results of this test.



Source: FHWA

Figure 83. Illustration. Finite-element results for splitting cylinder test with different material properties.

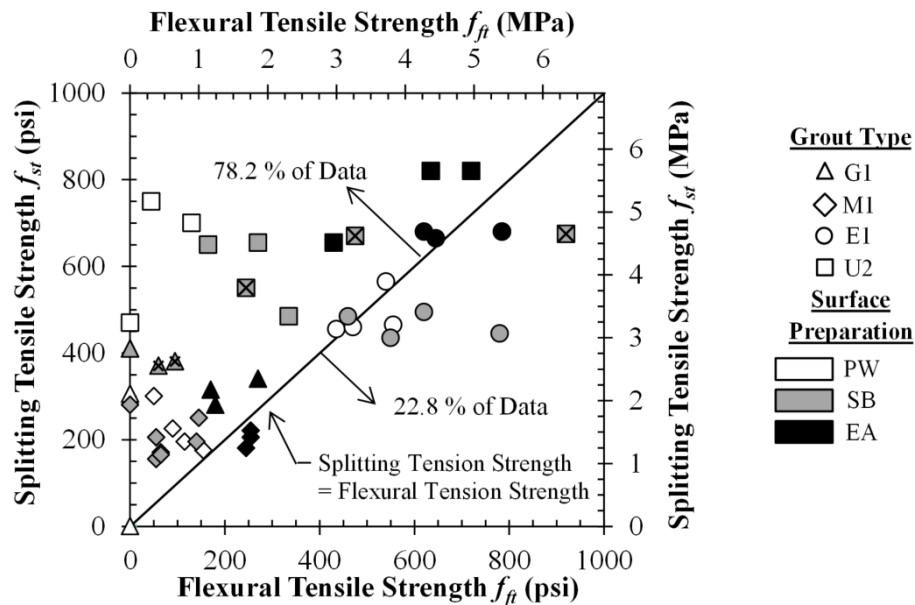
Results from the slant shear bond tests exhibited tends to be similar to those observed in flexural beam bond tests. That is, as the surface roughness increased, bond strength also increased. However, the results from the slant shear bond tests could be interpreted incorrectly due to the shear-friction effects (Nilson, Darwin, and Dolan, 2004). Figure 84 illustrates how shear friction occurs at the interface between the halves of the slant shear test specimen. When the load P is applied, a shear component acts parallel to the interface, P_v , and a normal component acts perpendicular, P_n . In order for failure to occur at the interface, the shear bond strength must be overcome along with the shear resistance caused by friction and the normal force P_n . Thus, the “true” bond strength between the two materials cannot be measured. This effect would become more predominate as the surface of the precast concrete half becomes rougher. Lastly, an empirical expression would be required to relate slant shear test results to the tensile bond strength between the concrete and the grout material.



Source: FHWA

Figure 84. Illustration. Shear friction effects in slant shear bond testing.

Both the flexural beam and splitting cylinder tests were used to evaluate the grout-to-precast concrete tensile bond strength. Figure 85 shows a comparison of tensile strength measured using these two test methods. The splitting cylinder tensile test reflected a larger tensile strength in the majority of materials and surface preparation configurations compared to those measured using a flexural beam test; 78.2 percent of tests showed higher tensile strength when the splitting cylinder test was used. Previous research has shown that the splitting tensile strength of plain concrete is typically 10 to 40 percent lower than the flexural tension strength (Mindess, Young, and Darwin, 2003). Thus, the results shown in figure 85 are contrary to the expected relationship between the splitting and flexural tension strength of plain concrete. This could be partly due to the stiffness difference between the two halves in the splitting cylinder tests, as discussed previously.



Note: An “X” over a data point marker indicates the use of an epoxy bonding agent on precast concrete.

Source: FHWA

Figure 85. Graph. Comparison between splitting cylinder and flexural beam tensile bond tests.

Overall Assessment and Key Observations

In general, the cementitious grouts G1 and M1 showed poor bond performance compared with U2 and E1 grouts. Non-shrink cementitious grout (G1) exhibited a poor bond with the concrete in each test regardless of the concrete substrate surface preparation. However, the bond was marginally improved through the use of the exposed aggregate preparation. A similar statement can be made regarding the performance of the magnesium phosphate grout (M1). Tests using UHPC as a grout material indicate that bond performance can be enhanced by increasing the level of surface roughness of the precast concrete component. Using UHPC grouts in conjunction with exposed aggregate surface preparation can provide sufficient bond strength such that the tensile strength of concrete can be developed. The best overall bond performance was exhibited by specimens that employed the epoxy grout material (E1). Bond performance was independent of the surface preparation method and the age of the material. Furthermore, the majority of specimens failed in the precast concrete away from the bond line.

In regard to test methods, flexural beam tests produced somewhat consistent results. The specimens tested in this study had 6-inch (152-mm) square cross-sections as specified by ASTM C78. The size of the beam resulted in some handling issues (i.e., specimens breaking apart prior to testing). Therefore, a smaller beam sample may need to be considered, but it would need to be evaluated and compared with available test results. Splitting tensile tests did not indicate a significant difference between the surface preparation methods such as that of the flexural beam.

A simple finite-element model showed that if the cylinder halves have a large differential stiffness, then the stress distribution can be affected and the test results may be misleading. The slant shear test does indicate differences in bond strength with respect to the surface preparation method and grout material. However, reliance on this test method would require a framework to relate slant shear results with flexural tensile or direct tensile behaviors. Given the stress state that is tested as compared to the stress state that is of interest, it is not clear that development of such a construct would be appropriate.

CHAPTER 5. DECK-LEVEL CONNECTION TEST RESULTS

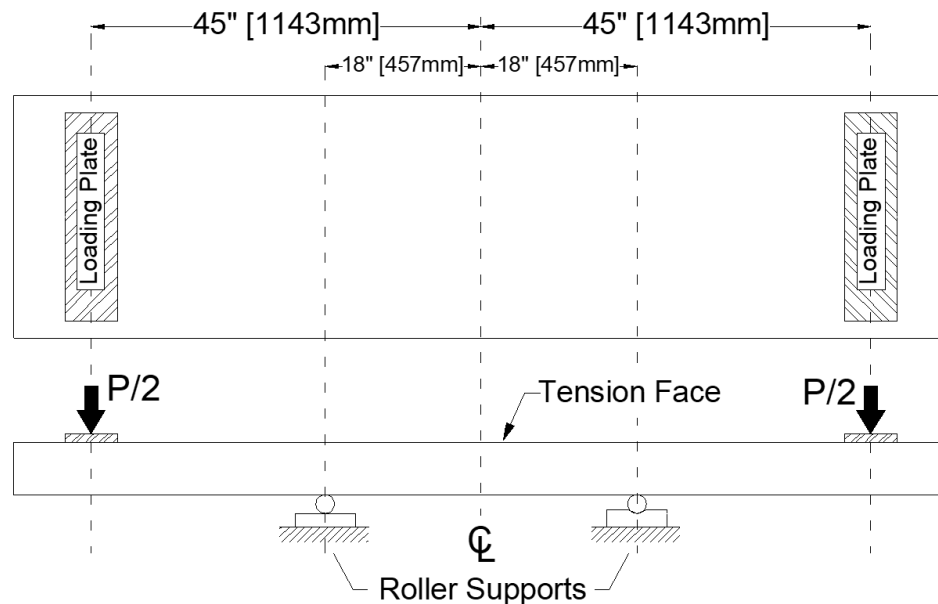
INTRODUCTION

The loading protocols and test results from deck-level connection tests are presented in this chapter. The experimental test setup and loading protocols are discussed followed by discussion of test results, which are grouped by loading protocol. The body, figures, and tables presented provide an overview of the key observations and results that are required to substantiate the conclusions presented in Chapter 6.

TEST PROCEDURES

Test Setup

The test setup is shown in figure 86. Specimens were tested in four-point bending using a 110-kip (490 kN) servo-controlled hydraulic actuator as shown in figure 87. The tension face of the specimen was positioned upward to facilitate inspection during testing. The grouted connection region was located within the constant moment region between the center supports. Prior to initial application of the load, each specimen was inspected for cracks that may have been caused by shrinkage or handling. Specimens were subjected to three different loading protocols: crack cyclic loading, post-cracking fatigue loading, and monotonic ultimate loading, which were applied in succession. If a specimen failed, which was defined as an abrupt loss of load-carrying capacity during one of the loading protocols, then subsequent loading was not pursued.



Source: FHWA

Figure 86. Illustration. Deck panel test set-up.

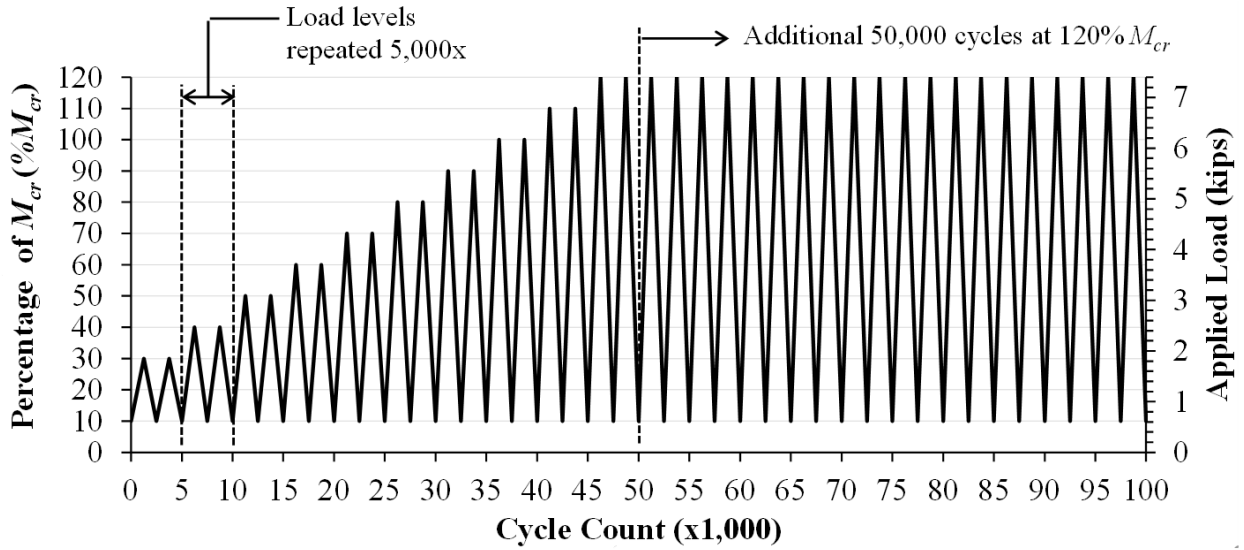


Source: FHWA

Figure 87. Photo. Deck panel specimen during loading.

Pre-Crack Cyclic Loading

The primary goals of the pre-cracking cyclic loading procedure were to investigate the performance of the grout-concrete interface at the component-level scale and to investigate the cracking resistance of the connection region. The cyclic crack loading protocol is shown in figure 88. The cracking moment, M_{cr} , was calculated using the equation shown in figure 89, which is based on provisions specified in section 5.7.3.3.2 of the *AASHTO LRFD Bridge Design Specifications*. (AASHTO 2010) M_{cr} was determined to be 98.8 kip-in (11.2 kN-m). The required actuator force to produce M_{cr} was 6.2 kips (27.6 kN); the calculated moments include the specimen self-weight and loading fixtures such as bearing plates. The load was applied at a frequency between 3 Hz and 5 Hz, and it was cycled between 10 percent of M_{cr} ($0.1M_{cr}$) and an upper load target that varied with the number of applied cycles. Five thousand cycles were applied for each upper load target that ranged from 30 percent of M_{cr} ($0.3M_{cr}$) to 120 percent of M_{cr} ($1.2M_{cr}$). An additional 50,000 cycles were applied at the 120 percent of M_{cr} ($1.2 M_{cr}$) target.



Source: FHWA

Figure 88. Illustration. Pre-cracking cyclic loading protocol (1 kip = 4.448 kN).

$$M_{cr} = \frac{f_r I_g}{y_t}$$

Figure 89. Equation. Cracking moment as define by AASHTO (2010).

Where

f_r = modulus of rupture of concrete defined by the equation shown in

figure 90

I_g = gross moment of inertia of the deck cross-section

y_t = distance between the neutral axis of bending and the extreme tension fiber of the deck cross-section

$$f_r = 0.24\sqrt{f'_c} \text{ (in ksi)}$$

Figure 90. Equation. Modulus of rupture for normal-weight concrete as defined by AASTHO (2010).

Where

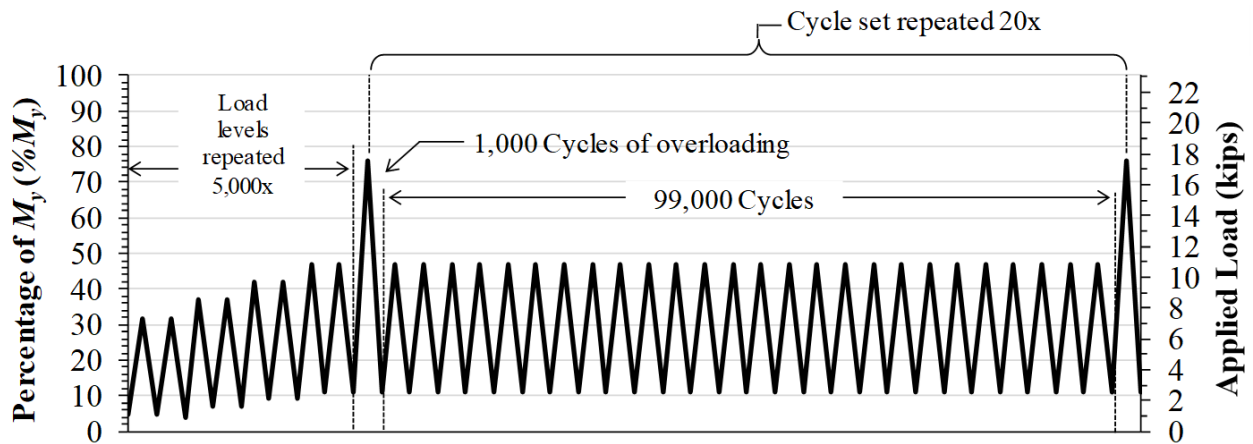
f'_c = specified 28-day compressive strength of concrete; deck panel concrete was specified to have compressive strength of 6 ksi (41.3 MPa) after 28 days.

Post-Cracking Fatigue Loading

The post-cracking fatigue loading protocol is shown in figure 91. This protocol had three different loading regimes: ramp-up cycles, a low-level cycles range, and a high-level cycles range that is referred to as “overloading.” The primary goal of the low-level cycle range was to subject the connection region to the maximum stress range without inducing fatigue fracture of the steel reinforcing bars. The load limits for the low-level cycles were determined using the constant amplitude fatigue threshold expression defined by AASHTO (2010) that is shown in its updated form in figure 92, which is from the 6th Edition of the LRFD. (AASHTO 2014a) A minimum load target of approximately 11 percent of calculated yield moment ($0.11M_y$) was selected, which was used to determine f_{min} . The upper load target for the low-level range was subsequently selected to be 47 percent of yield moment ($0.47M_y$). This resulted in a calculated stress range of 21.2 ksi (146 MPa) in the tension steel. Low-level cycles were applied in 99,000 cycle sets, where the maximum and minimum target actuator loads were 10.9 kips (48.4 kN) and 2.6 kips (11.6 kN), respectively. The overload cycles employed the same minimum load target as the low-level cycles but included an increased upper load target. The upper load target for the overload cycles was selected to be approximately 75 percent of M_y ($0.75M_y$), which corresponded to an actuator load of 17.6 kips (78.4 kN). Overload cycles were applied in sets of 1,000 cycles. Prior to initiating overload and low-level fatigue cycles, four ramp-up load steps were applied. Each step consisted of 5,000 cycles. The target peak applied actuator load for each of these groups was 7.37 kips (32.8 kN), 8.55 kips (38.0 kN), 9.72 kips (43.2 kN), and 10.9 kips (48.4 kN), which corresponded to 32, 29, 33, and 37 percent of the calculated yield moment, respectively. The lower load target for each of these groups was 1.13 kips (5.0 kN), 1.63 kips (7.3 kN), 2.14 kips (9.5 kN), and 2.64 kips (11.7 kN), which corresponded to 3.8, 5.5, 7.3, and 9.0 percent of the calculated yield moment, respectively.

The fatigue loading protocol for U-bar specimens and specimen U2-5.5-B-EA-Tr-75 differed slightly from that described above. The ramp-up phase for these specimens consisted of a single load level instead of four different load levels, and 20,000 cycles that oscillated between minimum and maximum load targets of approximately 11 percent and 47 percent of M_y .

At the conclusion of the loading protocol, specimens had endured a total of 20,000 ramp-up cycles, 2 million low-level fatigue cycles, and 20,000 overload cycles.



Source: FHWA

Figure 91. Illustration. Post-cracking fatigue loading protocol.

$$(\Delta F)_{TH} = 24 - 20f_{min}/f_y \text{ (in ksi)}$$

Figure 92. Equation. Constant amplitude fatigue threshold defined by AASHTO (2014).

Where

f_{min} = minimum tensile stress in reinforcing steel

f_y = specified yield strength of reinforcing steel

Monotonic Ultimate Loading

Specimens that survived the fatigue loading protocol were subsequently subjected to monotonic loading until failure. Load was applied in displacement control in 0.05-inch (1.28-mm) increments until failure.

PRE-TEST OBSERVATIONS

Shrinkage cracking in prefabricated deck panel connections can lead to durability-related problems. Furthermore, cracks initiated by shrinkage can propagate during mechanical and/or thermal loading, resulting in damage and stiffness loss. Thus, prior to any mechanical loading, deck panel specimens were inspected for shrinkage cracks and other cracks resulting from handling. Particular attention was given to the grouted connection region. Figure 93 presents the number of specimens that exhibited shrinkage cracking as a function of grout type.

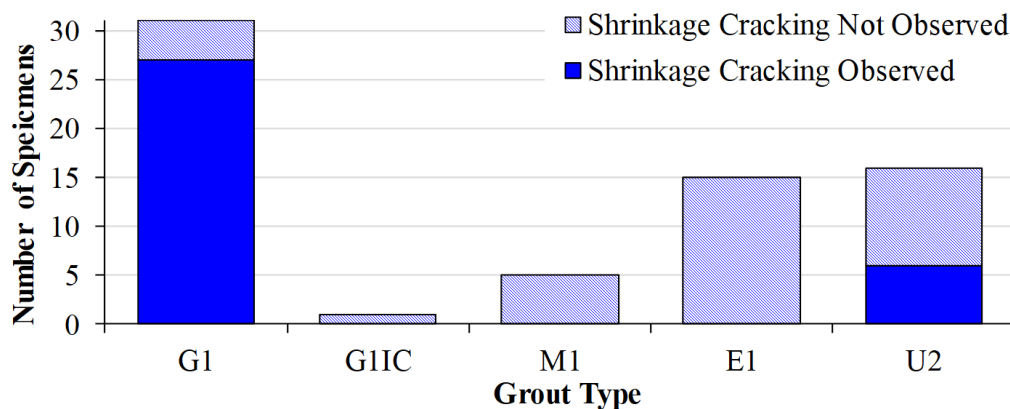
A total of 27 out of 31 specimens employing G1 grout exhibited shrinkage cracking in the connection grout. Figure 94 shows a representative photo of the shrinkage cracking observed in many of these specimens. For the most part, shrinkage cracking was extensive, and the cracks were observed in both longitudinal and traverse directions. In some cases, cracking was found at

the interface between the connection grout and the precast concrete. The result presented in the chapter indicated that G1 grout has a relatively low bond strength. Furthermore, Swenty and Graybeal (2013) showed that the G1 grout had the highest shrinkage strain rate of all the connection grout materials tested in this study; this was shown using the restrained shrinkage test described in ASTM C1581. (ASTM C1581/C1581M-09a, 2009) Thus, the shrinkage cracking could have been caused by a combination of weak bond strength and excessive shrinkage in the connection grout.

Figure 95 shows a photo of specimen G1IC-8.5-UB-EA-Tr-T-74. This specimen has the same variable combination as G1-8.5-UB-EA-Tr-T-73 except it included internal curing in the G1 connection grout. This specimen did not exhibit shrinkage cracking in the connection grout visible to the naked eye or shrinkage-induced cracks at the grout-concrete interface. This specimen exhibited only two relatively small shrinkage cracks that could be observed only via crack microscope. Previous research by the authors has shown that IC can mitigate autogenous shrinkage and reduce drying shrinkage in cementitious grouts by as much as 50 percent. (De la Varga and Graybeal 2015b; De la Varga, Haber, and Graybeal 2018) Thus, this was the expected outcome due to the enhanced shrinkage properties of internally-cured cementitious grouts.

Specimens with M1 or E1 grouts did not exhibit shrinkage cracking in the connection region. This was somewhat expected because magnesium phosphate and epoxy grouts have good dimensional stability, which was shown by Swenty and Graybeal (2013) and De la Varga and Graybeal (2015a).

Specimens with U2 grout exhibited shrinkage cracking in the connection region in 6 out of 16 specimens. Figure 96 shows a photo representative of the shrinkage cracking observed in specimens with U2 grout. Shrinkage cracks were fine and mostly occurred near free edges and adjacent to the concrete-grout interface but not at the concrete-grout interface. Furthermore, it is likely that these cracks were localized near the surface of the UHPC material.



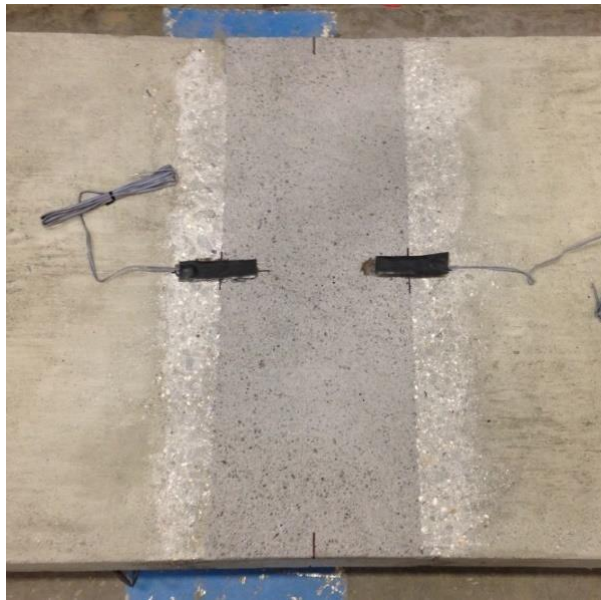
Source: FHWA

Figure 93. Graph. Observed shrinkage cracking in connection grout.



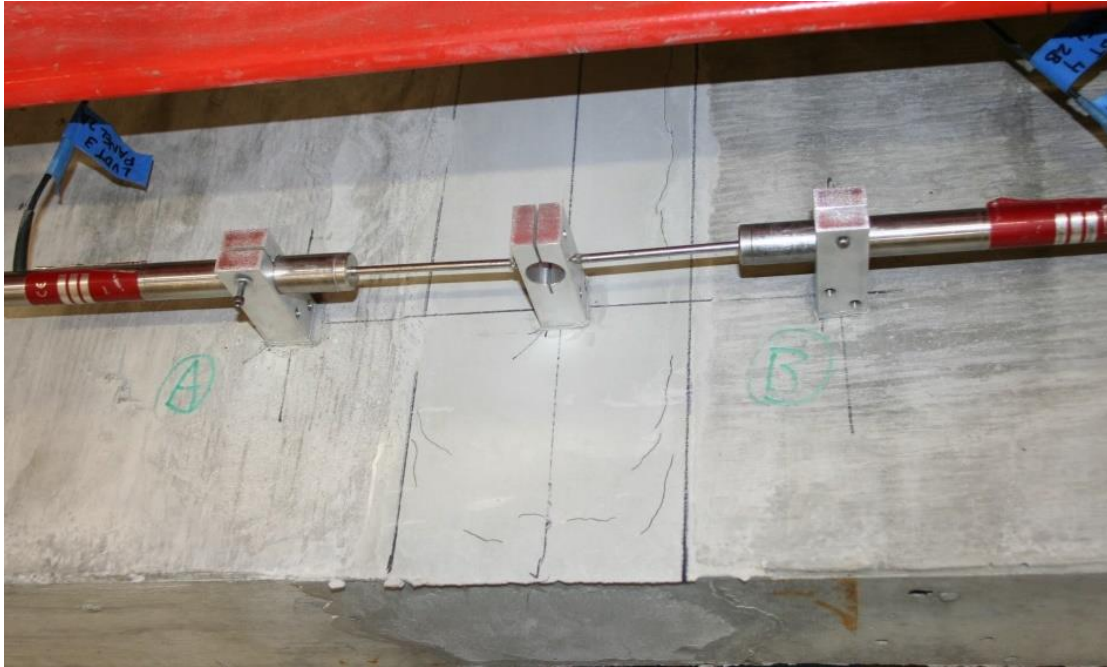
Source: FHWA

Figure 94. Photo. Representative photo of shrinkage cracking in specimens with G1 grout; specimen G1-8.5-UB-EA-Tr-T-73 shown.



Source: FHWA

Figure 95. Photo. Representative photo of the specimens with G1 grout and internal curing; specimen G1IC-8.5-UB-EA-Tr-T-74 shown.



Source: FHWA

Figure 96. Photo. Representative photo of shrinkage cracking in specimens with U2 grout.

TEST RESULTS

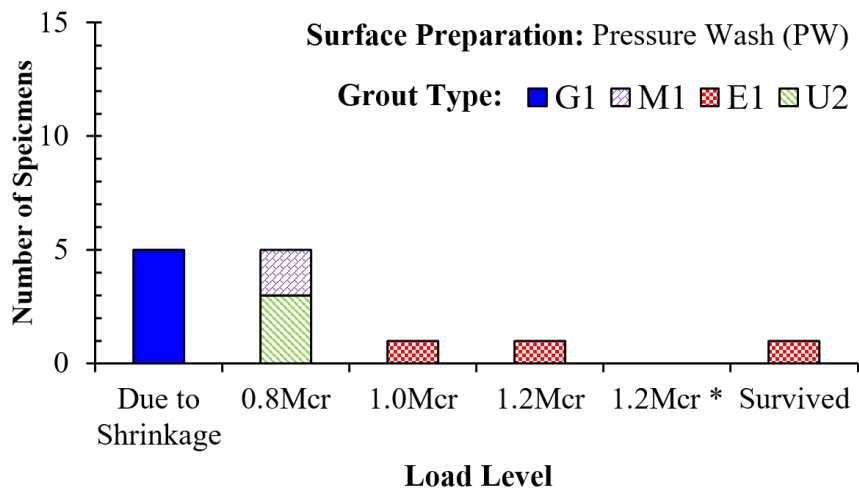
Pre-Crack Cyclic Loading

The primary objective of the pre-cracking cyclic loading was to evaluate the propensity for cracking-related damage in the grouted connection region. Of specific interest was the first cracking of the grout-concrete interface or cracking near the connection interface within the precast concrete deck panel. Due to field casting, cold joints form between the precast deck panels and the connection grout material. The test results discussed in Chapter 4 showed that the tensile bond strength of the grout-concrete interface, in some cases, is weaker than the lesser of the tensile strength of precast concrete or the grout material. Premature cracking at this interface can lead to durability issues as a result of water or chloride intrusion through the crack opening. Of equal interest was how cracks tended to nucleate and propagate in the presence of shrinkage cracks. Specimen behaviors were assessed by visual inspection and analysis of collected sensor data. As intended, all specimens survived the pre-cracking cyclic loading protocol.

Visual Assessment of Interface Cracking

Visual inspection of the grout-concrete interface was conducted after the $0.8M_{cr}$ (30,000 cycles), $1.0M_{cr}$ (40,000 cycles), $1.2M_{cr}$ (50,000 cycles), and at the end of the cyclic crack loading protocol (100,000 cycles) cycle sets; specimens with U-bars and specimen U2-5.5-B-EA-Tr-75 were inspected after each cycle set and were periodically inspected using a crack microscope.

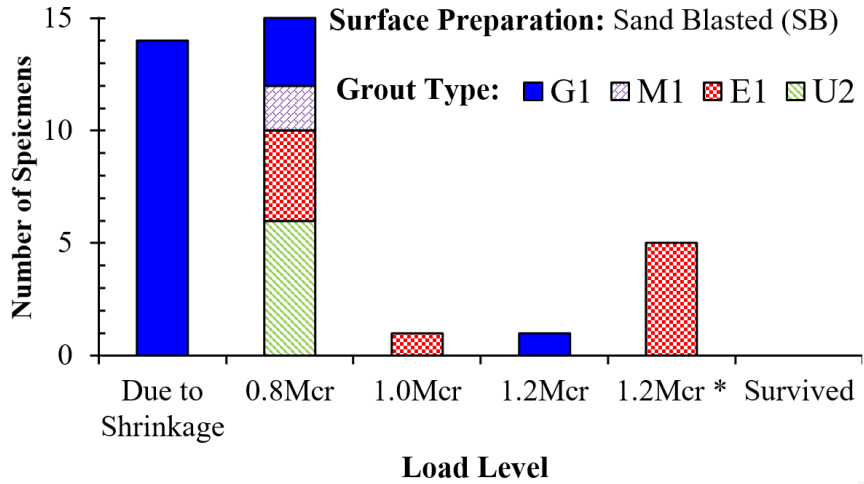
The results from these inspections are shown in figure 97 through figure 100. These figures report the number of specimens that exhibited interface cracking for a given load level. Results are presented as functions of connection grout type and surface preparation for different load levels. The majority of specimens employing G1 grout were observed to have interface cracking caused by shrinkage regardless of the precast concrete surface preparation. All specimens employing M1 grout displayed interface cracking after the $0.8M_{cr}$ cycles. Based on the results from bond characterization testing, this is not unexpected, given that G1 and M1 grouts exhibited poor bonding to precast concrete regardless of surface preparation. However, two specimens employing G1 grout did not exhibit interface cracking. Instead, cracking occurred with precast concrete near the grout-concrete interface. Approximately one-third of specimens employing E1 grout displayed interface cracking after $0.8M_{cr}$ cycles; these specimens all had SB surface preparation. The remaining two-thirds of E1 specimens exhibited interface cracking between the $1.0M_{cr}$ cycles and the end of the cyclic crack loading protocol. However, there was no distinct correlation between the load level where the apparent interface cracking occurred and the precast concrete surface preparation. The majority of specimens employing U2 grout exhibited interface cracking after the $0.8M_{cr}$ cycles. There were three specimens with U2 grout that had EA surface preparation. Two of these specimens survived the loading protocol without exhibiting interface cracking, while the third exhibited interface cracking at $1.2M_{cr}$. This observation was consistent with results from bond characterization testing that indicated the U2 grouts exhibited an improved bond to concrete when EA surface preparation was employed.



* denotes the end of the cyclic cracking loading protocol

Source: FHWA

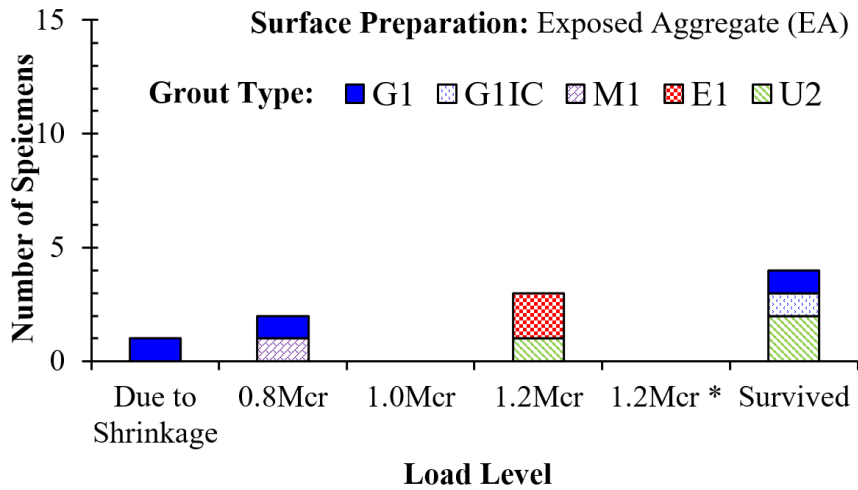
Figure 97. Graph. Observed interface cracking at different cracking cycle load levels for specimens with the pressure washed surface preparation.



* denotes the end of the cyclic cracking loading protocol

Source: FHWA

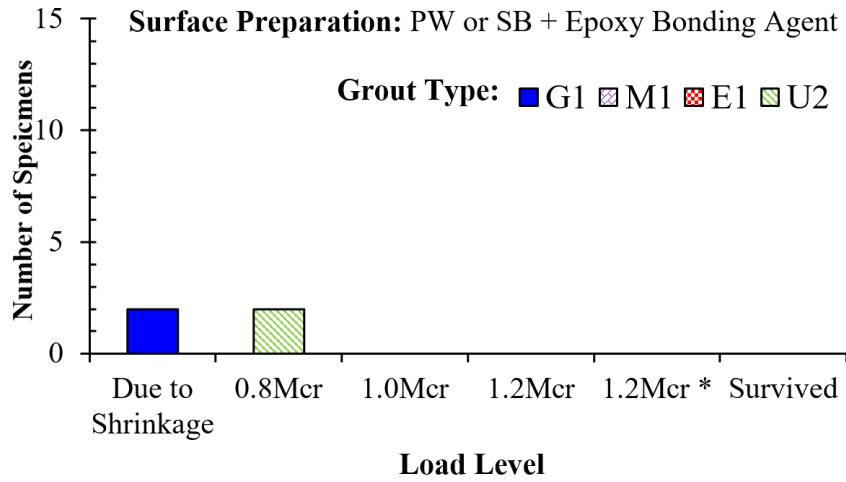
Figure 98. Graph. Observed interface cracking at different cracking cycle load levels for specimens with the sand blasted surface preparation.



* denotes the end of the cyclic cracking loading protocol

Source: FHWA

Figure 99. Graph. Observed interface cracking at different cracking cycle load levels for specimens with the exposed aggregate surface preparation.



* denotes the end of the cyclic cracking loading protocol

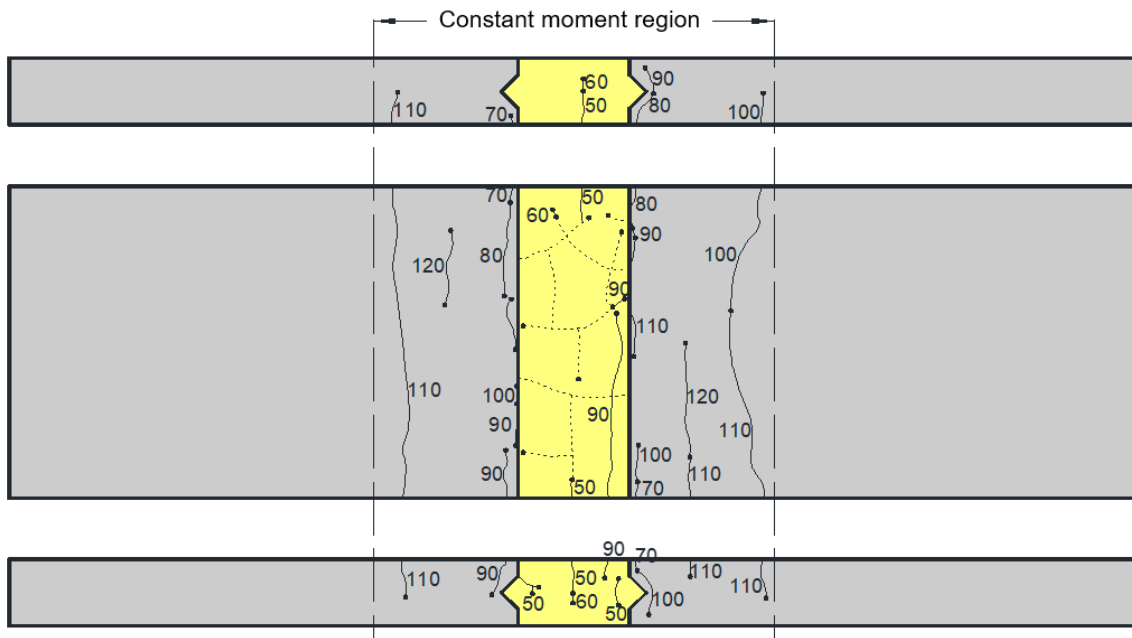
Source: FHWA

Figure 100. Graph. Observed interface cracking at different cracking cycle load levels for specimens with PW or SB preparation and epoxy bonding agents.

Apparent Damage

The progression of cracking damage was tracked by marking cracks with each increasing load level. Figure 101 through figure 103 shows the damage progression observed in a representative group of specimens. Shrinkage cracks are denoted by dashed lines, and the numerical values adjacent to cracks indicate the load level (in percent of M_{cr}) during crack formation. In general, shrinkage cracks within the connection grout tended to propagate with the application of mechanical load. For example, shrinkage cracks propagated at relatively low loads (50–60 percent of M_{cr}) in the case of specimen G1-8.5-UB-EA-Tr-T-73 that employed the G1 connection; this could indicate widening of existing fine cracks (see figure 101). Furthermore, in the case of the specimen employing G1 grout with IC (G1IC-8.5-UB-EA-Tr-T-74), shrinkage cracking did not propagate until 100 percent of M_{cr} (see figure 102). At this load level, the cracks in G1IC grout were approximately 0.003 inches (0.076 mm) wide. Figure 103 shows the damage progression exhibited by a representative specimen with UHPC connection grout (U2-5.5-B-EA-Tr-75). This specimen did not exhibit visually apparent cracks within the connection grout. When inspected with a crack microscope, microcracks were found that were smaller than 0.00098 inches (0.025 mm) wide, which was the minimum gradation on the microscope. Upon completion of the loading protocol, each specimen exhibited flexural cracking in the precast concrete deck panels.

- Denotes cracks formed by shrinkage (observed prior to mechanical loading)
- Denotes cracks formed by cyclic loading; number indicates % of M_{cr}

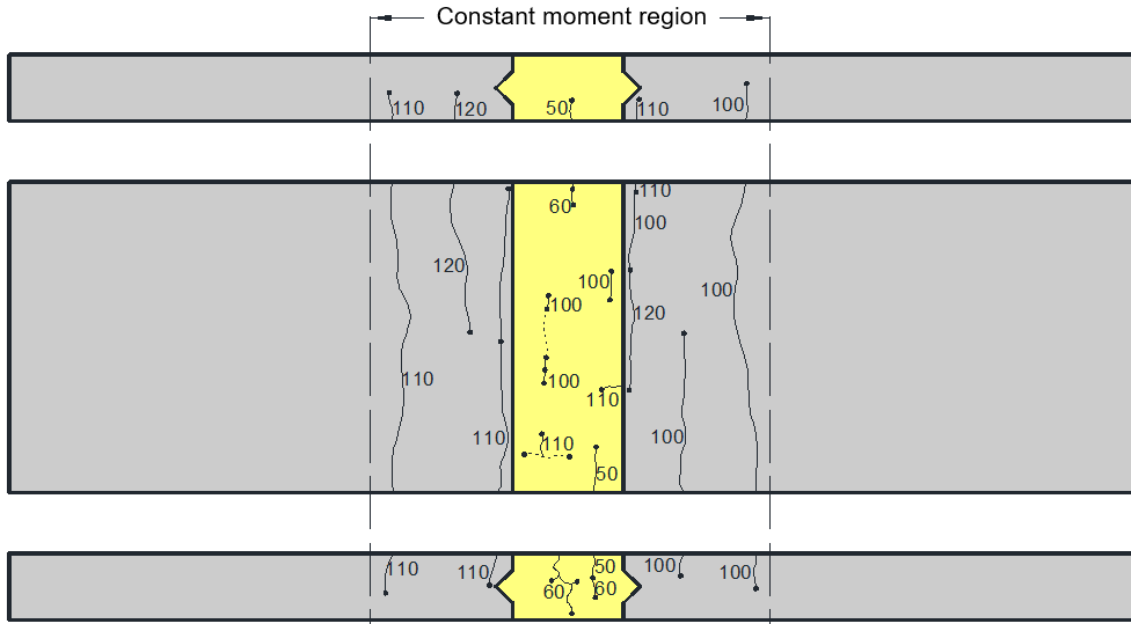


Note: Cracks are only shown in the constant moment region

Source: FHWA

Figure 101. Illustration. Damage progression during pre-cracking cyclic loading for specimen G1-8.5-UB-EA-Tr-T-73.

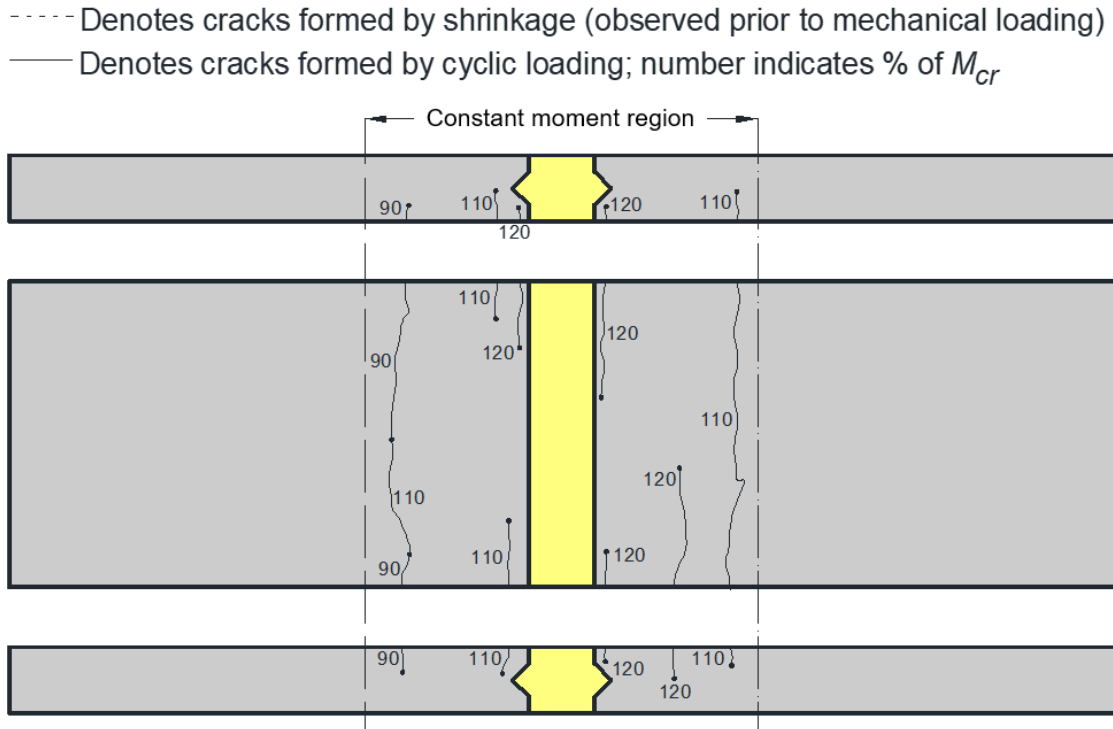
- - - - Denotes cracks formed by shrinkage (observed prior to mechanical loading)
- Denotes cracks formed by cyclic loading; number indicates % of M_{CR}



Note: Cracks are only shown in the constant moment region

Source: FHWA

Figure 102. Illustration. Damage progression during pre-cracking cyclic loading for specimen G11C-8.5-UB-EA-Tr-T-74.



Note: Cracks are only shown in the constant moment region

Source: FHWA

Figure 103. Illustration. Damage progression during pre-cracking cyclic loading for specimen U2-5.5-B-EA-Tr-75.

Figure 104 compares the apparent damage among different specimen types after completion of the loading protocol; a representative photo was selected for each grout type used. As noted previously, all specimens exhibited flexural cracks in the precast concrete deck panels at the end of the cyclic cracking loading protocol.

Many specimens employing G1 grout exhibited cracking at the grout-concrete interface. In some cases, cracking was apparent along the entire depth of the concrete-grout interface, which indicates that cracks were in part caused by shrinkage. Upon completion of the loading protocol, most of these specimens exhibited significant cracking within the G1 connection grout material.

Specimens employing the remaining three grout types, M1, E1, and U2, had minimal or no visible cracks within the grouted connection region. As previously noted, some of these specimens exhibited cracking along the concrete-grout interface. Figure 105 shows an example of specimen U2-5.5-B-EA-Tr-75, which did not exhibit interface cracking. Instead, cracking occurred in the precast concrete adjacent to the interface, which indicates a sound bond between the precast concrete and UHPC. Figure 106 compares the apparent damage in specimens with G1 connection grout with and without IC. This figure shows that using IC resulted in reduced cracking after low-level mechanical loading.



A. G1 connection grout



B. M1 connection grout



C. E1 connection grout



D. U2 connection grout

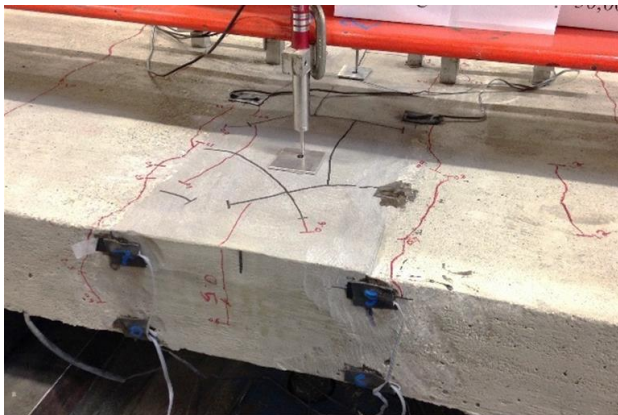
Source: FHWA

Figure 104. Photos. Representative photos of deck-level connection regions pre-cracking cyclic loading.

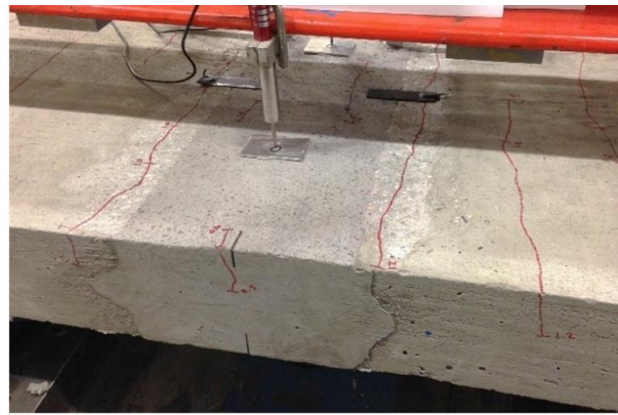


Source: FHWA

Figure 105. Photo. Specimen U2-5.5-B-EA-Tr-75 after cyclic crack loading.



A. Without IC: G1-8.5-UB-EA-Tr-T-73



B. With IC: G1IC-8.5-UB-EA-Tr-T-74

Source: FHWA

Figure 106. Photos. Comparison between specimens with and without IC.

Structural Response

The local and global effects of cracking on specimen behavior were quantified by examining strains across the grout-concrete interface, strains in steel reinforcing bars, and flexural stiffness degradation.

Interface behavior was assessed by comparing measured strains over the interface with the calculated theoretical response. After grout placement and curing, foil-backed resistive strain gages (SG) and spring-loaded LVDTs were installed over the grout-concrete interface. Four

bursts of data were recorded throughout each 5,000-cycle period. The measured results presented in this section reflect the last burst of data recorded for a given load level; this methodology captures the cumulative effect of the previous cycles at the same load level. Strain data is presented as change in tensile strain, $\Delta\varepsilon$, for a given load level. The change in tensile strain is defined by the equation presented in figure 107.

$$\Delta\varepsilon = \varepsilon_{t, max} - \varepsilon_{t, min}$$

Figure 107. Equation. Change in tensile strain.

Where

$\varepsilon_{t, max}$ = maximum tensile strain recorded during a given cycle

$\varepsilon_{t, min}$ = minimum tensile strain recorded during a given cycle

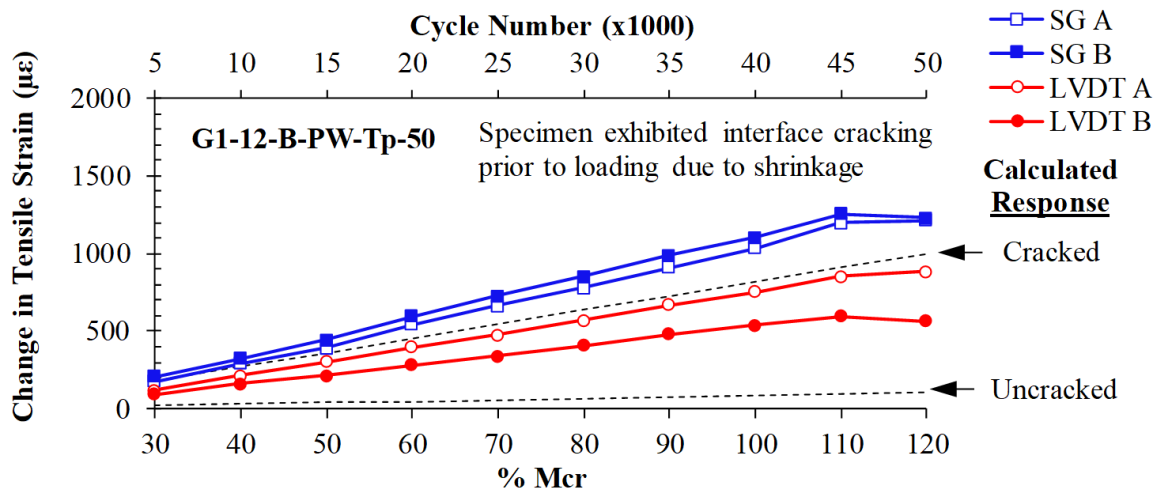
Comparison of measured and calculated data indicated that the majority of specimens followed one of two distinct trends that are denoted as “early-cycle interface cracking” and “late cycle interface cracking.” Figure 108 shows interface strain data from specimen G1-12-B-PW-Tp, which is representative of early-cycle interface cracking behavior. This figure shows the relationship between $\Delta\varepsilon$ and the load level in terms of percent M_{cr} (and cycle number). Two reference lines are also shown that correspond to the theoretical (calculated) response of the specimen in the cracked and uncracked state; these are denoted by dashed lines. Each data point represents data collected near the end of a given cracking cycle set. For each load step, the measured strains were significantly higher than those calculated for an uncracked section. In fact, the measured interface strains were close to or exceeded those for a cracked section. This indicates that either the bond at the grout-concrete interface has failure or a crack formed near the interface. This would indicate one of two scenarios: the precast concrete-grout interface was cracked prior to loading, or the interface (or area near the interface) cracked during the first 5,000 cycles at the $0.3M_{cr}$ load level.

There were eight specimens employing G1 grout (including G1IC) that did not have apparent interface cracking due to shrinkage:

1. G1-8-B-SB-Tp-3.
2. G1-12-B-SB-Tp-5.
3. G1-12-B-PW+E1-Tr-30.
4. G1-12-B-SB-Tr-31.
5. G1-12-B-EA-Tr-33.

6. G1-12-B-SB-Tp-49.
7. G1-8.5-UB-EA-Tr-T-73.
8. G1IC-8.5-UB-EA-Tr-T-74.

However, six had measured strains comparable to the calculated cracked response by completion of the $0.5M_{cr}$ load level. This indicates that cracking likely occurred well before it was noted through visual inspection and well before the nominal calculated cracking strength of the deck panel. Furthermore, there was little to no correlation between interface cracking behavior and different parameter combinations for specimens with G1 grout. The behavior illustrated in figure 108 was also representative of specimens employing M1 grout and a portion of the specimens employing U2 grout. That is, specimens exhibited measured strains comparable to the cracked section response prior to visual observation of interface cracking. All specimens with M1 grout had apparent cracking at the concrete-grout interface after the $0.8M_{cr}$ cycle set. However, comparison of measured and calculated strain data indicated that all specimens had interface strains comparable with the cracked section by the end of the $0.6M_{cr}$ load level. Similar to that observed in G1 specimens, there was no correlation between interface bond behavior and different parameter combinations for M1 specimens. Approximately two-thirds of specimens employing U2 grout exhibited early cracking behavior similar to specimens with G1 and M1 grout.



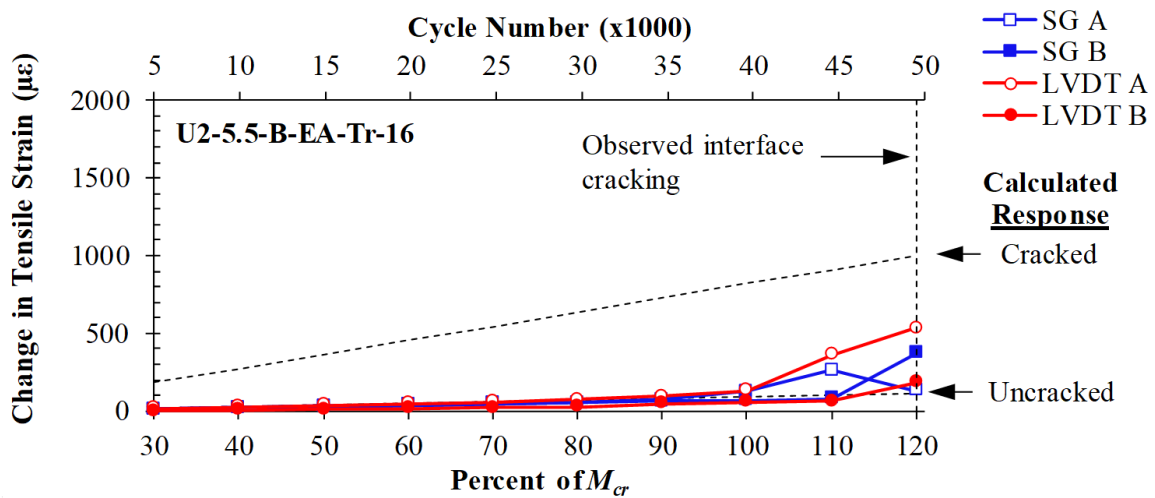
Source: FHWA

Figure 108. Graph. Example of early cracking behavior in specimen G1-12-B-PW-Tp (50).

One-third of the specimens with U2 grout and the majority of specimens with E1 grout exhibited the second distinct trend observed in strain measurements across the interface, which is referred to as “late-cycle cracking.” Specimens that exhibited this behavior had measured strains that were comparable with those calculated for an uncracked specimen for most load levels prior to visual observation of interface cracking. Furthermore, a distinct point could be identified where

measured strains dramatically increased, indicating crack formation at or near the concrete-grout interface. This behavior is depicted in figure 109, which shows the result from specimen U2-5.5-B-EA-Tr.

Prior to $1.0M_{cr}$, measured strains were comparable with those calculated for an uncracked section. After $1.0M_{cr}$, the measured strains began to increase significantly, which would indicate that the concrete-grout interface (or region in close proximity) likely ruptured during load cycles between $1.0M_{cr}$ and $1.2M_{cr}$ load levels. Visual inspection of U2-5.5-B-EA-Tr indicated that the interface was bonded after 5,000 cycles of $1.0M_{cr}$ but exhibited cracks after cycling at $1.2M_{cr}$, which confirms measured data.



Source: FHWA

Figure 109. Graph. Example of late cracking behavior in specimen U2-5.5-B-EA-Tr (16).

In general, evaluation of the strain measured over the concrete-grout interface revealed that the majority of specimens employing G1, M1, and U2 grouts cracked prior to the first visual inspection of the interface that was made at $0.8M_{cr}$. On the contrary, a small group of specimens with U2 grout employing exposed aggregate interface surface preparation or epoxy bonding agents did not show interface cracking until later in the loading protocol. Many specimens employing E1 grout also showed that interface cracking did not occur until later in the loading protocol.

The aforementioned trends can be observed in figure 111 through figure 113. These figures present the normalized interface strain, which is defined in figure 110, for three select load levels: $0.3M_{cr}$, $0.5M_{cr}$, and $1.0M_{cr}$. All specimens employing M1, E1, and U2 grouts are shown, while a representative group of specimens with G1 grout are shown for each of three load levels.

$$\text{Normalized Interface Strain} = \frac{\Delta\varepsilon_{\text{measured}}}{\Delta\varepsilon_{\text{cracked}}}$$

Figure 110. Equation. Normalized interface strain.

Where

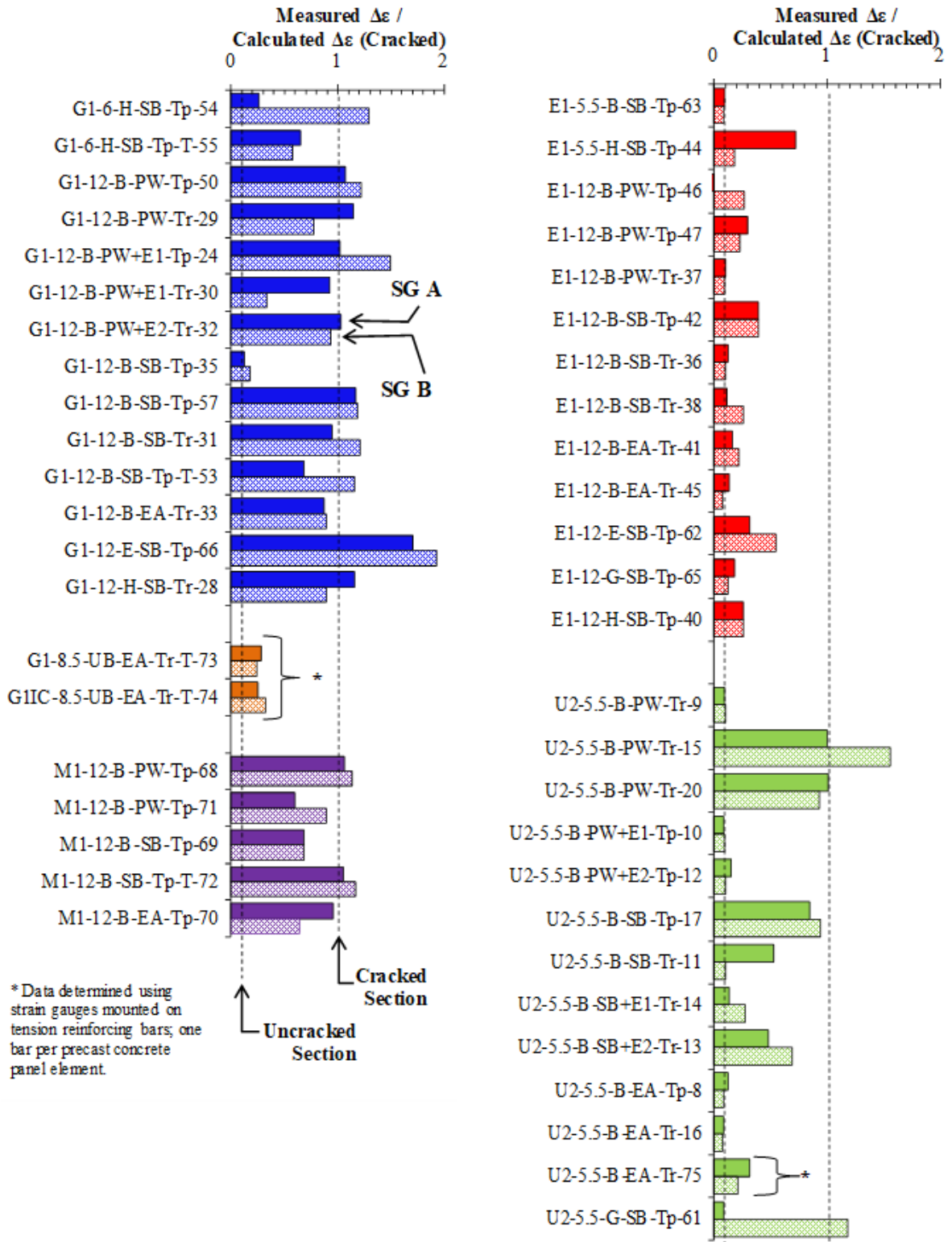
$\Delta\varepsilon_{\text{uncracked}}$ = Change in tensile strain as defined by figure 107

$\Delta\varepsilon_{\text{cracked}}$ = Calculated change in tensile strain assuming a cracked section

Figure 111 depicts the normalized interface strain at the end of the $0.3M_{cr}$ cycle set. These plots clearly identify that a majority of specimens with G1 and M1 grout likely developed interface cracking due to shrinkage or sustained interface cracking during the first 5,000 cycles of the loading protocol. In comparison, specimens with E1 grout exhibited strains comparable with the uncracked section, and nine out of the thirteen specimens with U2 grout exhibited strain comparable with the uncracked section, five of which employed either EA surface preparation or epoxy bonding agents on the precast concrete panel.

Figure 112 depicts the normalized interface strain at the end of the $0.5M_{cr}$ cycle set. All specimens employing G1 and M1 grouts exhibited interface strains comparable with the cracked section with the exception of G1-12-B-SB-Tp-35, G1-8.5-UB-EA-Tr-73, and G1-8.5-UB-EA-Tr-74. Specimens employing E1 grout still showed relative low strains that were comparable with the uncracked section. Five specimens with U2 grout had strains similar to uncracked section response, of which five employed either EA surface preparation or epoxy bonding agents. The remaining U2 specimens showed larger interface strains, some of which exceeded the cracked section response.

Figure 113 depicts the normalized interface strain at the end of the $1.0M_{cr}$ cycle. Many of the trends noted previously can be observed. However, at this point in the loading protocol, most specimens exhibited large strains at the concrete-grout interface.



Source: FHWA

Figure 112. Graph. Normalized tensile strain response at the concrete-grout interface at $0.5M_{cr}$.

Similar to the results from bond characterization testing (Chapter 3), cyclic crack loading showed that the interface bond behavior was primarily governed by grout type and could be influenced, in some cases, by surface preparation. Precast concrete surface preparation did not have a significant influence on the behavior of the connections with G1, M1 and E1 grouts. That is, G1 and M1 grouts exhibited poor performance regardless of concrete surface preparation while E1 grout exhibited good performance regardless of surface preparation. Connections with U2 grout showed that bond strength of the concrete-grout interface could be improved with EA surface preparation or with the application of epoxy bonding agents on the precast concrete prior to grout placement.

Post-Cracking Fatigue Loading

All 4 monolithic deck panel specimens and 49 precast specimens survived the fatigue loading protocol. This section focuses on the failure mechanisms of those specimens that did not survive fatigue loading and the damage accumulated by those that did survive. Results are grouped according to the type of grout material used within the connection region.

Fatigue Performance of Specimens with G1 Grout

Of the 32 specimens employing G1 grout, 14 failed during fatigue loading. Table 22 provides a list of the specimens that failed during the fatigue loading along with information related to the number of cycles sustained prior to failure. The “Total Cycle Count” represents the total number of fatigue cycles the specimen completed prior to failure, which includes ramp-up, overload, and non-overload fatigue cycles. The “Overload Cycle Count” represents the total number of overload cycles the specimen completed prior to failure. Of the 14 specimens that failed during the post-cracking fatigue loading protocol, 13 specimens failed during overload cycles, and a single specimen failed during the low-level cycles (G1-8-B-SB-Tp-3).

After testing, these specimens were inspected. Wide longitudinal splitting cracks were observed within the G1 grout along with wide cracks at the concrete-grout interface. In some cases, the G1 grout completely broke apart and fell away from the specimen. Figure 114 shows representative photos of the specimens with G1 grout that failed during fatigue loading. These observations indicate that bond failure between the embedded reinforcing bars and the grout connection material occurred. Most G1 specimens that failed during fatigue loading had numerous shrinkage cracks. These cracks propagated during cyclic crack loading while new cracks also formed. During fatigue loading, cracks continued to propagate and eventually began to weaken the bond between the reinforcing bars and grout, which led to failure. As can be observed in table 22, fatigue failure of specimens with G1 grout occurred as early as the third overload cycle. It should be noted that the documented shrinkage cracking in the specimens that survived fatigue loading (16 of 30) was noted to be less extensive than that observed in specimens that failed during fatigue loading.

The 18 specimens that survived fatigue loading had significant cracking within the G1 grout upon completion of the fatigue loading protocol. Visual observations captured throughout the course of testing were used to identify a well-defined damage sequence. Figure 115 through figure 117 show the progression of damage that occurred within the grouted connection region of specimens employing G1 grout; note that the specimen shown in these figures, G1-12-B-SB-Tp-34, was representative of those employing G1 grout that survived fatigue loading. Prior to the fatigue loading, flexural and splitting cracks were observed within the G1 grout (see figure 115). As fatigue loading began and as the cycle count increased, existing cracks propagated and joined with adjacent cracks, and new flexural cracks formed. This behavior can be observed by comparing the crack patterns in figure 115 with those in figure 116. Existing cracks continued to grow until completion of the fatigue protocol (see figure 117).

Table 22. Summary of specimens with G1 grout that failed during fatigue loading.

Specimen ID	Total Cycle Count	Overload Cycle Count
G1-12-G-SB-Tp-64	20,003	3
G1-12-E-SB-Tp-66	20,020	20
G1-12-B-SB-Tp-59	20,202	202
G1-12-B-PW-Tr-29	20,813	813
G1-12-B-SB-Tr-26	20,873	873
G1-12-B-SB-Tr-31	20,879	879
G1-8-B-SB-Tp-3*	100,500	1,000
G1-12-B-PW+E2-Tp-22	120,364	1,364
G1-12-B-PW-Tp-50	420,431	4,431
G1-12-B-PW-Tr-27	520,756	5,756
G1-12-B-SB-Tp-51	920,939	9,939
G1-12-B-PW+E1-Tp-24	1,220,255	12,255
G1-12-B-SB-Tp-T-53	1,320,959	13,959
G1-12-B-PW-Tp-58	1,620,671	16,671

* Specimen failed during low-level fatigue cycles.



A. G1-12-E-SB-Tp-66



B. G1-12-B-SB-Tr-59

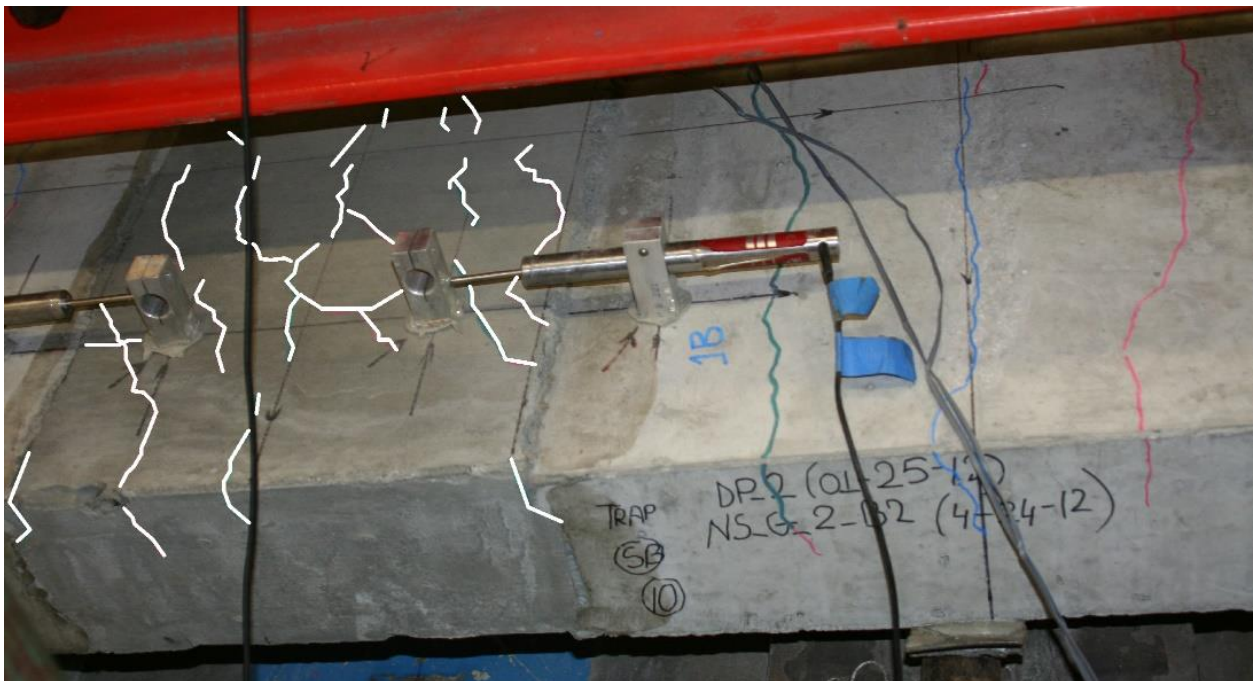
Source: FHWA

Figure 114. Photos. Representative photos of fatigue failure of specimens with G1 grout.



Source: FHWA

Figure 115. Photo. Representative photo of deck-level connection specimen with G1 grout after completion of cyclic crack loading (Specimen G1-12-B-SB-Tp-34 shown).



Source: FHWA

Figure 116. Photo. Representative photo of deck-level connection specimen with G1 grout during fatigue loading (Specimen G1-12-B-SB-Tp-34 shown after 794,744 cycles).



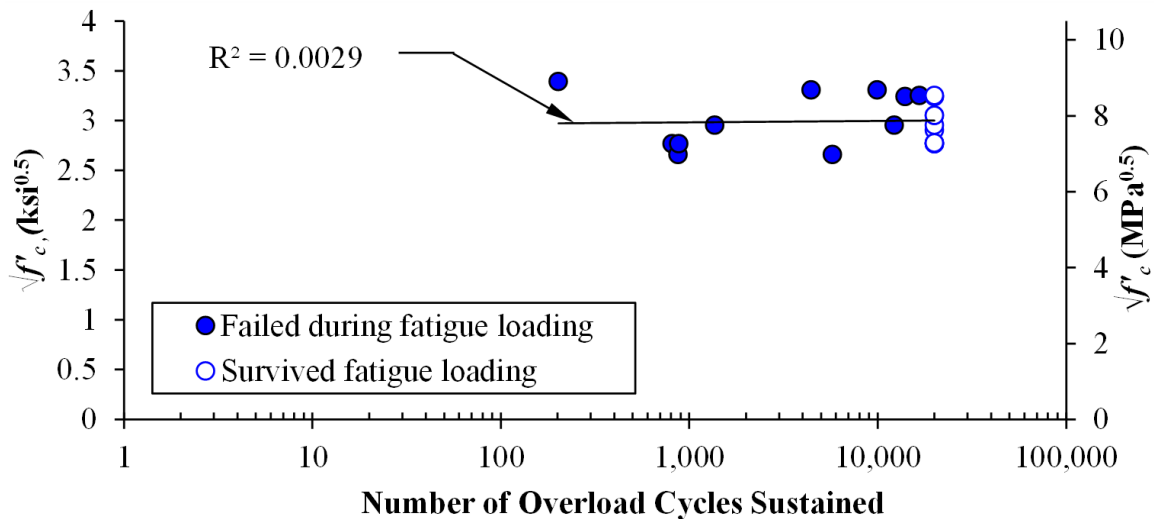
Source: FHWA

Figure 117. Photo. Representative photo of deck-level connection specimen with G1 grout after completion of fatigue loading (Specimen G1-12-B-SB-Tp-34 shown).

The majority of specimens employing G1 grout had 12-inch (305-mm) lap splice lengths. Some of these specimens failed during fatigue loading, while others completed the loading protocol without failure, and the data does not explicitly indicate why this happened. It has been well documented that reinforcing bar bond behavior is highly dependent on both the tensile strength of the cementitious substrate and the splice (or development) length of the embedded bar. (ACI Committee 408, 2003) Thus, differences in the tensile strength of the G1 grout could be related to fatigue resistance. The tensile strength of cement-based materials is typically correlated with the square root of the compressive strength of the material, and the compressive strength of the G1 grout varied from specimen to specimen on the day the testing began. The maximum and minimum grout strengths were 7 ksi (48.7 MPa) and 11.5 ksi (79.2 MPa), respectively. Figure 118 shows the relationship between $\sqrt{f'_c}$ and the number of overload cycles sustained by each specimen with G1 grout and a 12-inch (305-mm) lap splice length; herein f'_c is the measured compressive strength of the G1 grout on the first day of fatigue testing. It should be noted that specimens with epoxy-coated and GFRP bars were excluded from figure 118. The graph uses overload cycles sustained rather than total cycles because the specimens were subject to more demand, and the majority of specimens failed during overload cycles. A linear trend line is

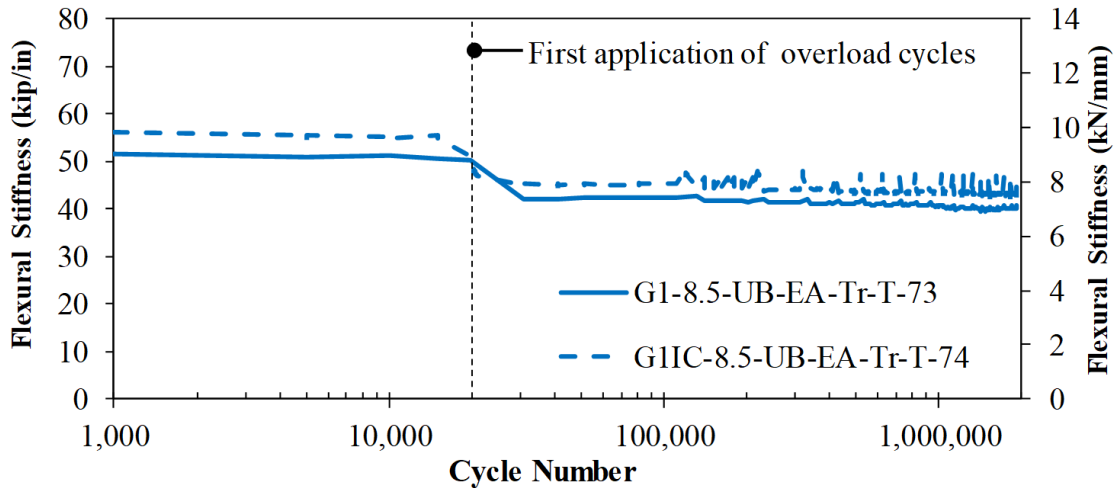
shown along with the corresponding coefficient of determination, R^2 . The trend line is flat and the coefficient of determination is close to zero, which indicates that there is very little, if any, correlation between $\sqrt{f'_c}$ and the number of overload cycles sustained. Therefore, grout strength did not influence the fatigue behavior of the specimens.

Flexural stiffness is a response parameter that defines the resistance of a member to flexural deformation, and it is commonly represented as the force generated per unit of displacement or deformation. Considered a global response parameter, flexural stiffness plays an important role in how forces are distributed throughout a structural system. Degradation of flexural stiffness can result in excessive deflections and undesirable redistribution of forces. One of the primary sources of stiffness losses in reinforced concrete structures is cracking, but stiffness loss can also be a result of reinforcing bar slippage (loss of bond). Figure 119 shows the relationship between flexural stiffness degradation and number of load cycles for specimens with U-bars. The purpose of this graph is to demonstrate that U-bar connections exhibited good fatigue performance. The data presented in this graph only reflects measurements taken during the low-level cycles. As noted previously, a set of 20,000 low-level cycles was applied prior to the first set of overload cycles. During these first 20,000 cycles, there was very little stiffness degradation. A sizable drop in stiffness can be observed immediately after the 20,000-cycle mark, which is a result of the first set of overload cycles. The abrupt stiffness loss was a result of newly formed cracks and propagation of existing cracks. New cracks primarily formed within the precast concrete deck sections. The key observation is that very little stiffness loss occurred, thus good performance was confirmed.



Source: FHWA

Figure 118. Graph. Relationship between number of overload cycles sustained and $\sqrt{f'_c}$ for specimen with G1 grout and 12-inch (305-mm) lap splice lengths.



Source: FHWA

Figure 119. Graph. Relationship between flexural stiffness and cycle number for specimens with U-bars; the graph only reflects data recorded during low-level cycles.

Fatigue Performance of Specimens with M1 Grout

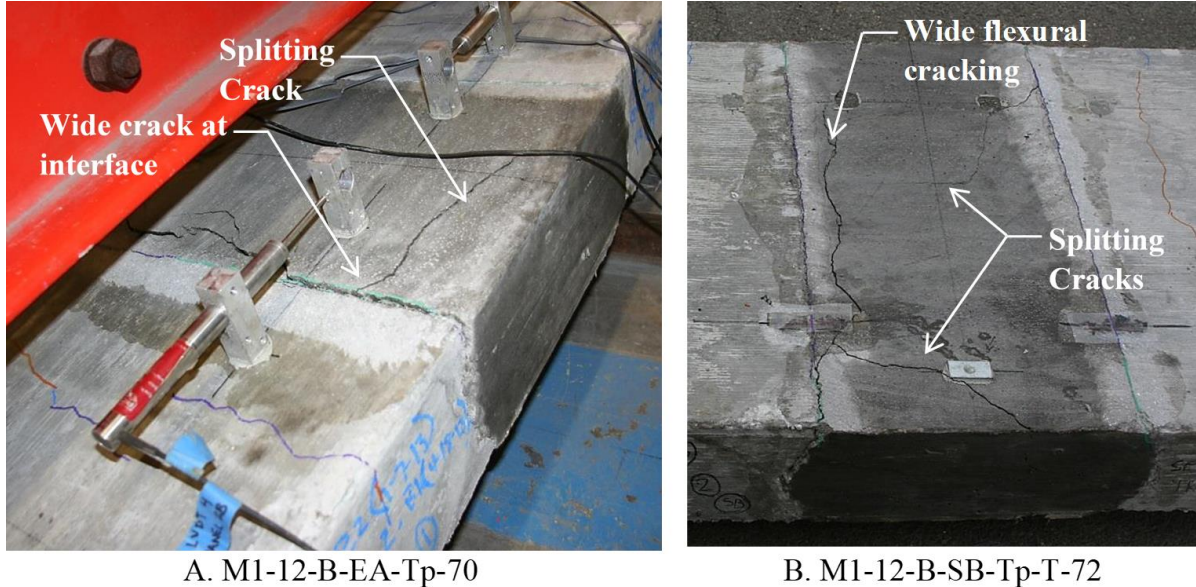
All specimens employing M1 grout failed during the fatigue loading protocol. Table 23 provides a list with the specimen identification and the information related to the number of cycles sustained prior to failure. Other than specimen M1-12-B-SB-Tp-69, all specimens failed during the first 1,000 cycles of overloading. The observed failure mode was similar to that exhibited by specimens with G1 grout. Figure 120 shows representative photos of two specimens with M1 grout that failed during fatigue loading. Large cracks in the concrete-grout interface can be observed in both photos. During overload cycles, the maximum applied load was 60 percent of the nominal yield force. Thus, wide cracks within the deck panel would not be expected unless the longitudinal reinforcing bars began to slip from the M1 grout as a result of bond failure. This was further substantiated by the presence of longitudinal splitting cracks within the M1 grout. Unlike specimens with G1 grout, shrinkage cracks in the grout material were not observed prior to loading, and flexural cracks were not observed after cyclic crack loading. The bond failure appears to have been significantly influenced by damage caused during fatigue loading.

Table 23. Summary of specimens with M1 grout that failed during fatigue loading.

Specimen ID	Total Cycle Count	Overload Cycle Count
M1-12-B-PW-Tp-68	20,298	298
M1-12-B-SB-Tp-69*	75,422	1,000
M1-12-B-EA-Tp-70	20,114	114
M1-12-B-PW-Tp-71	20,069	69
M1-12-B-SB-Tp-T-72	20,619	619

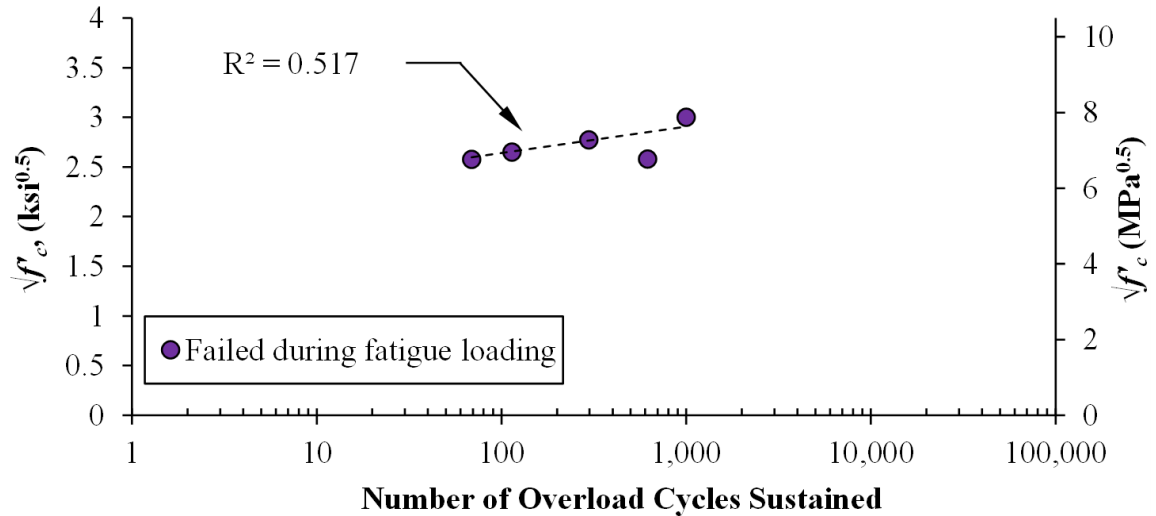
* Specimen failed during non-overload fatigue cycles.

All five specimens with M1 grout employed 12-inch (305-mm) lap splice lengths. Similar to observations from the fatigue testing of similar specimens with G1 grout, there was no apparent justification for the number of cycles sustained prior to failure. Figure 121 shows the relationship between $\sqrt{f'_c}$ and the number of overload cycles sustained by each specimen with M1 grout. The trend shown has a distinct positive slope, which indicates some level of correlation between $\sqrt{f'_c}$ and the number of overload cycles sustained. The coefficient of determination was 0.517, which is almost directly between 0 and 1, and which indicates that the correlation is neither weak nor strong. Thus, it is likely that grout strength had some influence on the fatigue behavior of the specimens with M1 grout, but grout strength did not drive the performance.



Source: FHWA

Figure 120. Photo. Representative photos of fatigue failure of specimens with M1 grout.

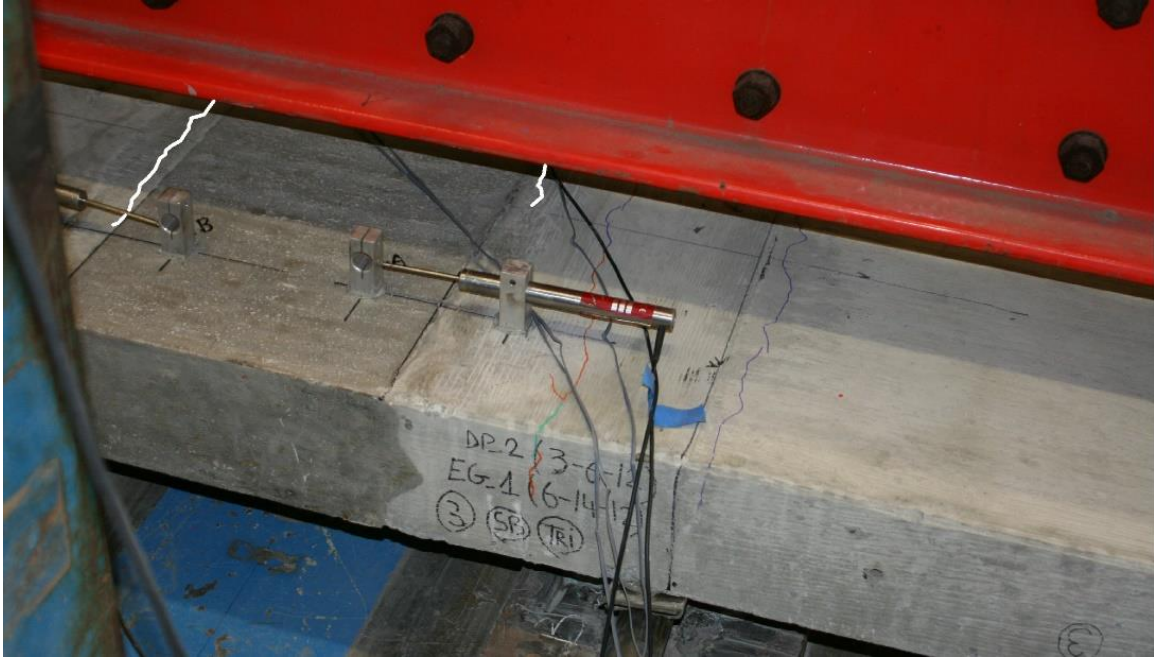


Source: FHWA

Figure 121. Graph. Relationship between number of overload cycles sustained and $\sqrt{f'_c}$ for specimen with M1 grout and 12-inch (305-mm) lap splice lengths.

Fatigue Performance of Specimens with E1 Grout

All specimens employing E1 grout survived the fatigue loading protocol. It should be noted that 5.5-inch (140-mm) and 12-inch (305-mm) lap splice lengths were tested. Observations made during and after fatigue testing indicated that little to no apparent damage occurred within the grouted connection region other than interface cracking. Figure 122 through figure 124 show a set of representative photos depicting the observed progression of damage in specimens with E1 grout during fatigue loading. Prior to fatigue loading, cracking along the concrete-grout interface or cracking in the precast concrete near the concrete-grout interface were the only signs of apparent damage within the connection region (see figure 122). As fatigue loading began and as the cycle count increased, existing cracks propagated along the interface and new cracks formed in the precast concrete deck panels; cracks did not form within the E1 grout (see figure 123). This behavior can be observed by comparing the crack patterns in figure 122 with those in figure 123. The propagation of interface cracks was primarily caused by overload cycles, and once a crack ran the complete length of the interface, very little damage occurred thereafter. Figure 124 shows a representative photo of a specimen with E1 grout upon completion of the fatigue loading protocol.



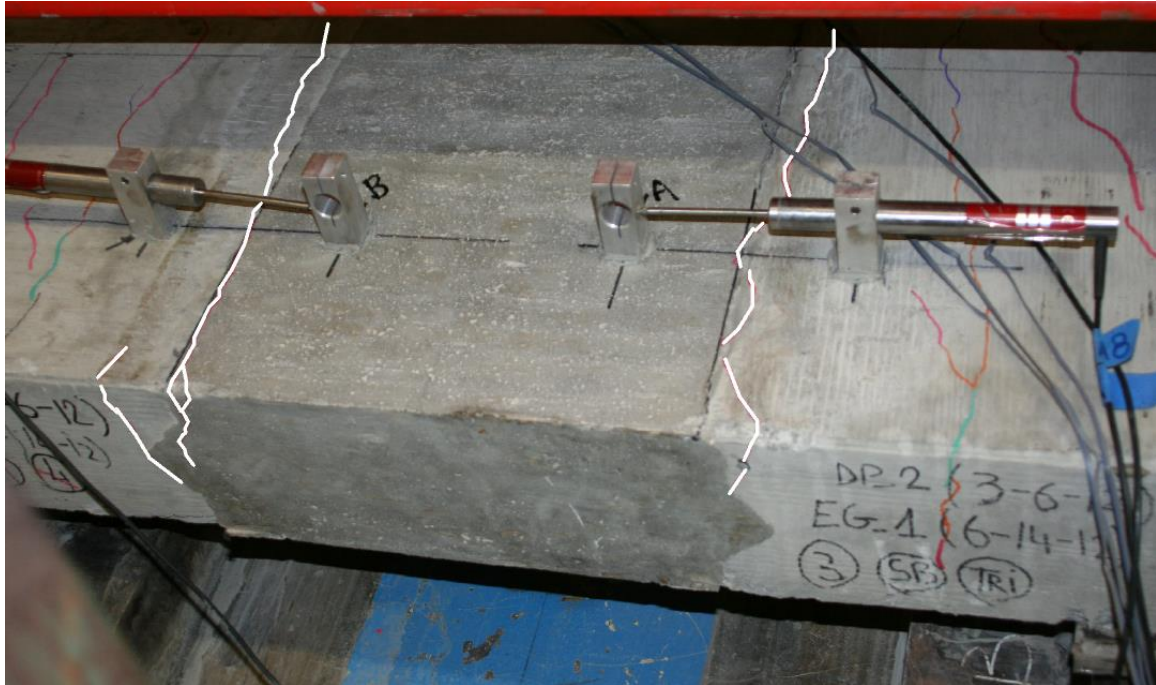
Source: FHWA

Figure 122. Photo. Representative photo of deck-level connection specimen with E1 grout after completion of cyclic crack loading (Specimen E1-12-B-SB-Tr-36 shown).



Source: FHWA

Figure 123. Photo. Representative photo of deck-level connection specimen with E1 grout during fatigue loading (Specimen E1-12-B-SB-Tr-36 shown after 263,943 cycles).



Source: FHWA

Figure 124. Photo. Representative photo of deck-level connection specimen with E1 grout after completion of fatigue loading (Specimen E1-12-B-SB-Tr-36 shown).

Fatigue Performance of Specimens with U2 Grout

Similar to specimens with E1 grout, all specimens employing U2 grout survived the fatigue loading protocol. Specimens with U2 grout employed only a 5.5-inch (140-mm) lap splice length. Observations made during and after fatigue testing indicated that little to no apparent damage occurred within the grouted connection region other than interface cracking. Figure 125 through figure 127 show the observed progression of damage in a representative specimen with U2 grout during fatigue loading. Prior to fatigue loading, damage within the connection region was limited to cracking along the concrete-grout interface, cracking in the precast concrete near the concrete-grout interface, and/or minor cracking within the U2 grout in some specimens (see figure 125). As fatigue loading began and as the cycle count increased, existing cracks propagated along the interface, new cracks formed in the precast concrete deck panels, but no new cracks formed in the U2 grout. This behavior can be observed by comparing the crack patterns in figure 125 with those shown in figure 126. The propagation of interface cracks was primarily caused by overload cycles, and once a crack ran the complete length of the interface, very little damage occurred thereafter. Figure 127 shows a representative photo of a specimen with E1 grout upon completion of the fatigue loading protocol.

Figure 128 shows the relationship between flexural stiffness degradation and number of load cycles for a single specimen with the U2 connection grout; data from the specimens with U-bars is also shown for comparison. The data presented in this graph reflect measurements taken only during the low-level fatigue cycles. Similar to previous results, abrupt loss of stiffness was observed after the first set of overload cycles as a result of newly formed cracks and propagation of existing cracks. In the specimen employing the U2 grout, new cracks formed within the precast concrete deck sections. A crack microscope was used to further inspect the UHPC connection grout after fatigue loading. The inspection revealed that a few fine microcracks were present with crack widths smaller than 0.001 inch. (0.025 mm). For comparison, the specimen employing the G1 grout exhibited a significant amount of cracking within the connection grout and had crack widths greater than 0.01 inch. (0.25 mm).



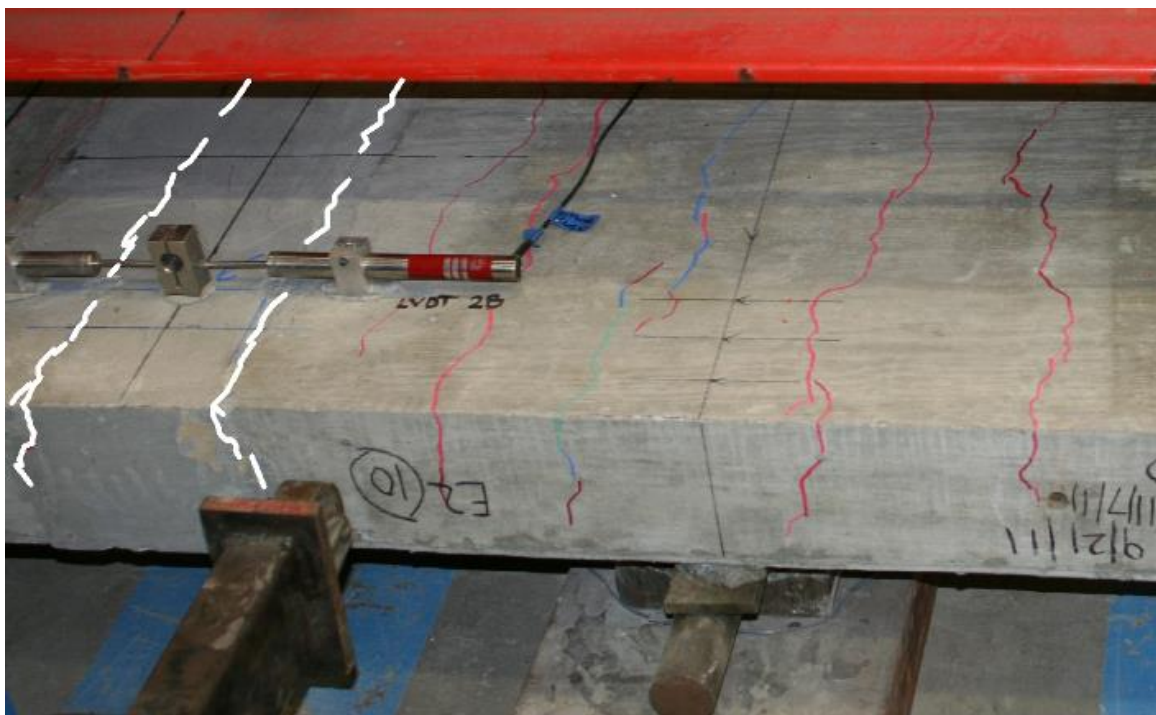
Source: FHWA

Figure 125. Photo. Representative photo of deck-level connection specimen with U2 grout after completion of cyclic crack loading (Specimen U2-5.5-B-SB+E1-Tr-12 shown).



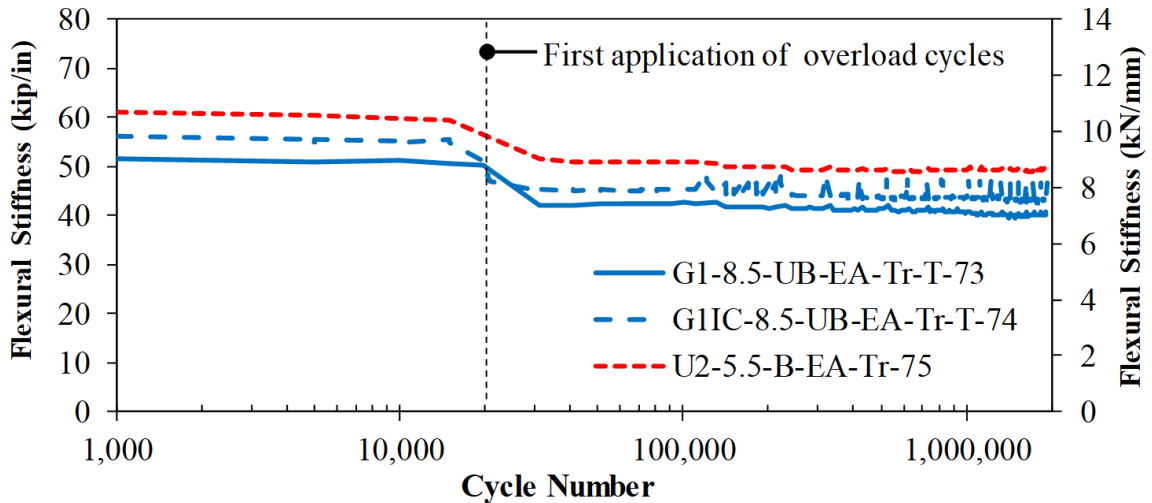
Source: FHWA

Figure 126. Photo. Representative photo of deck-level connection specimen with U2 grout during fatigue loading (Specimen U2-5.5-B-SB+E1-Tr-12 shown after 1,291,897 cycles).



Source: FHWA

Figure 127. Photo. Representative photo of deck-level connection specimen with U2 grout after completion of fatigue loading (Specimen U2-5.5-B-SB+E1-Tr-12 shown).



Source: FHWA

Figure 128. Graph. Relationship between flexural stiffness and cycle number for U2-5.5-B-EA-Tr-75 compared with specimens with U-bars; the graph only reflects data recorded during low-level cycles.

Monotonic Ultimate Loading

Specimens that survived the fatigue loading protocol were subsequently subjected to monotonic ultimate loading. The results of the loading are presented in the following sections. The ultimate load performance of the specimens was assessed by comparing the apparent yield strength, ultimate strength, and estimated displacement ductility of the precast panels with corresponding monolithic control panels. In this report, displacement ductility, which is a measure of post-yield deformation before failure, is defined according to the equation shown in figure 129. This definition is similar to that used by Azizinamini et al. (1999). A specimen was considered to have failed after a 20 percent drop in the applied load once the peak applied load had been reached. The displacement of the deck specimens was determined using the measured displacement of the actuator.

$$\text{Displacement Ductility} = \frac{\Delta_U}{\Delta_Y}$$

Figure 129. Equation. Definition of displacement ductility.

Where

Δ_U = vertical displacement of the deck panel at peak applied (ultimate) load

Δ_Y = vertical displacement of the deck panel upon apparent yielding steel, which was identified as a significant decrease in flexural stiffness

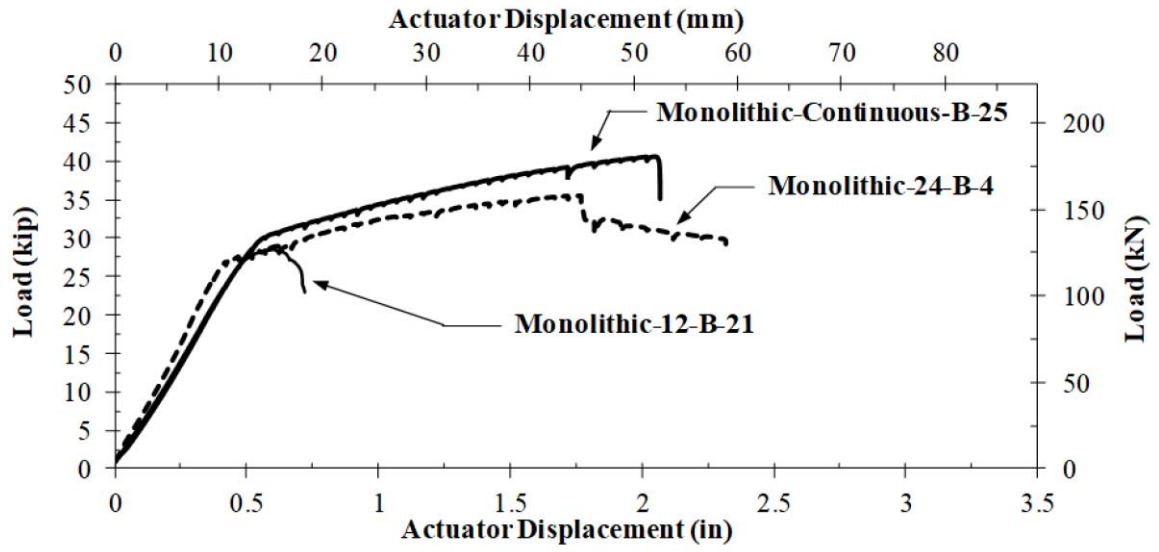
Results from the monolithic deck panel specimens with mild steel reinforcing bars, which established the baseline behavior for precast panels, are discussed first. The ultimate loading response of precast panels with mild steel bars is subsequently discussed in groups according to the type of grout used within the connection region. For each grout type, a set of representative force-displacement curves are presented along with photos of the observed failure modes. The specimens employing GFRP reinforcing bars, both monolithic and precast, are discussed together within a single subsection following the discussion of specimens with mild steel bars. The achieved ultimate load and displacement ductility are compared among specimens at the end of the section.

Monolithic Deck Panel Specimens with Mild Steel Bars

The measured force-displacement curves from monolithic deck panel specimens with mild steel bars are presented in figure 130. Specimen Monolithic-Continuous-B-25, which was the primary baseline specimen with continuous longitudinal reinforcing bars, exhibited ductile behavior during monotonic loading. The force-displacement curve for Monolithic-Continuous-B-25 was comparable to what would be expected for a RC flexural member designed to be tension-controlled. After the apparent yield point, which was observed at approximately 31 kips (138 kN), wide flexural cracks began to form on the tension face of the design panel due to yielding of the steel (figure 131-A). Failure of Monolithic-Continuous-B-25 was a result of concrete crushing near of the mid-span supports, which can be observed in figure 131-A

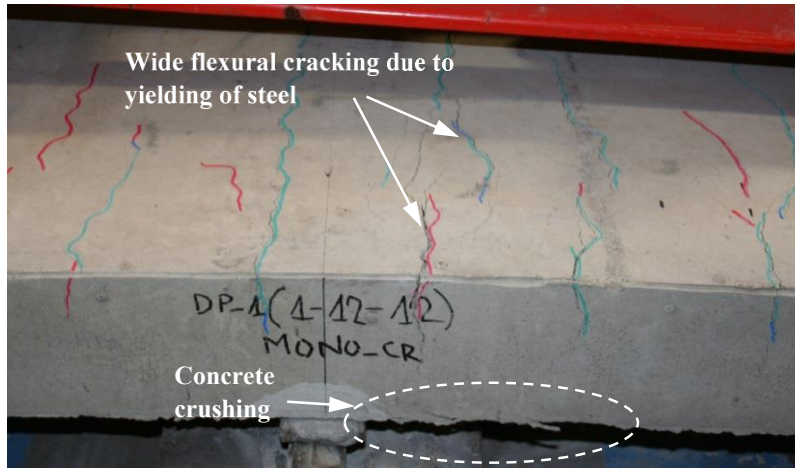
The monolithic panel with a 24-inch (610-mm) non-contact lap splice, Monolithic-24-B-4, also exhibited ductile behavior. The general behavior of Monolithic-24-B-4 was comparable with that of Monolithic-Continuous-B-25, although the apparent yield and the ultimate strengths were slightly lower; lower strengths can be attributed to variation in material properties. Failure of specimen Monolithic-24-B-4 was a result of concrete crushing at the mid-span of the deck panel, which can be observed in figure 131-B. At failure, similar to Monolithic-Continuous-B-25, wide flexural cracks could be seen on the tension face of the deck panel within the constant moment region. It can be deduced that these wide cracks were caused by yielding of the steel rather than bond failure between the embedded bars and concrete given that longitudinal splitting cracks were not observed.

Contrary to the other monolithic panels, the panel that employed a 12-inch (305-mm) non-contact lap splice, Monolithic-12-B-21, did not exhibit ductile behavior. Shortly after the apparent yielding of the steel, which occurred at approximately 29 kips (129 kN), Monolithic-12-B-21 experienced an abrupt loss of applied load. After testing, visual inspection revealed longitudinal splitting cracks and wide flexural cracks within the region that contained the lap splice (figure 131-C). Because the panel did not experience large post-yield deformation, wide flexural cracks were likely a result of bar pull-out from bond failure. This indicates that a 12-inch (305-mm) non-contact lap splice is not sufficient for developing the ultimate capacity of the panel.

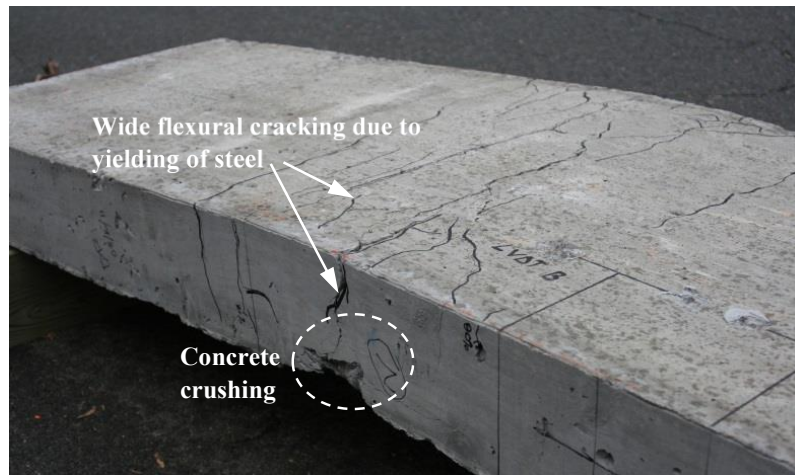


Source: FHWA

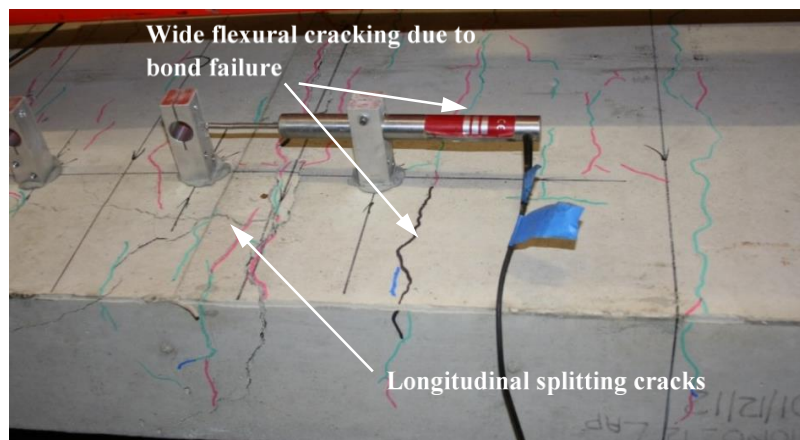
Figure 130. Graph. Force-displacement behavior of monolithic deck panels with mild steel bars.



A. Monolithic-Continuous-B-25



B. Monolithic-24-B-4



C. Monolithic-12-B-21

Source: FHWA

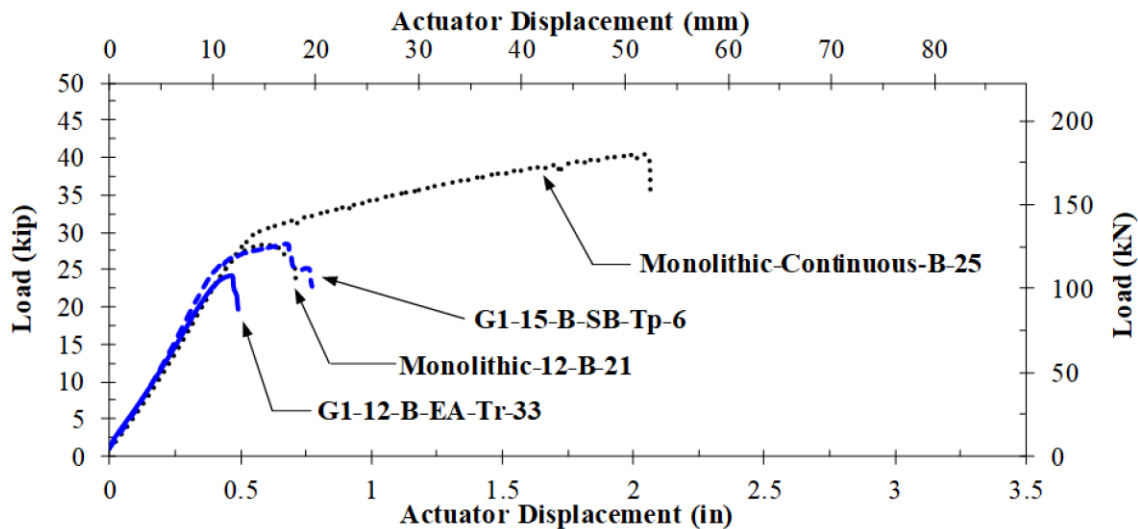
Figure 131. Photos. Observed failure modes of monolithic deck panels with mild steel bars.

Precast Deck Panel Specimens with G1 Grout and Mild Steel Bars

In general, deck panels employing G1 grout did not perform well in the ultimate load tests. These deck panels exhibited low ultimate loads at failure compared with Monolithic-Continuous-B-25. In most cases, specimens failed prior to yielding of the steel and exhibited little to no ductility. All specimens failed prematurely due to bond failure caused by excessive cracking within the G1 grout.

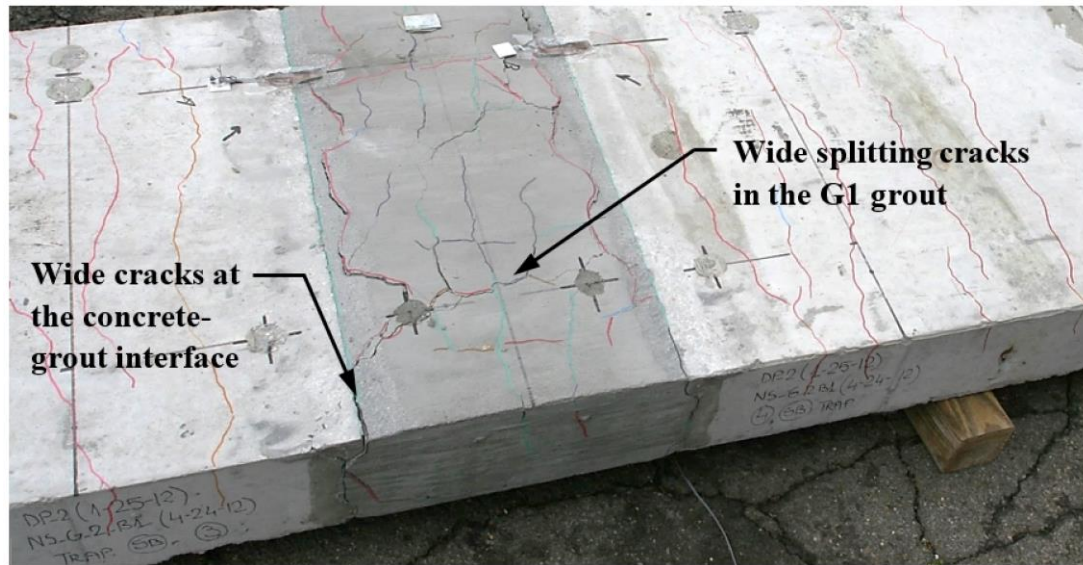
Figure 132 shows a set of measured force-displacement curves for two specimens with G1 grout and different lap splice lengths: G1-12-B-EA-Tr-33 and G1-15-B-SB-Tp-6. The force-displacement curves from Monolithic-Continuous-B-25 and Monolithic-12-B-21 are also shown for comparison. Specimen G1-12-B-EA-Tr-33, which employed a 12-inch (305-mm) lap splice, failed abruptly and prior to the apparent yielding of the steel. As noted previously, failure occurred by bar pull-out from the grout materials. This was evident from wide cracks at the concrete-grout interface although yielding did not occur, and by longitudinal splitting cracks within the grout material as shown in figure 133.

Even when the lap splice length was increased from 12 inches (305 mm) to 15 inches (381 mm), the performance of the panel was not significantly improved and bond failure still governed the behavior of the specimen. It can be observed in figure 132 that the force-displacement behavior of G1-15-B-SB-Tp-6 was similar to that of Monolithic-12-B-21. Although yielding of the steel was achieved along with a higher loading bearing capacity compared with G1-12-B-EA-Tr-33, the ductility of the panel was still poor compared with that of Monolithic-Continuous-B-25.



Source: FHWA

Figure 132. Graph. Force-displacement relationships from specimens with G1 grout and straight black bars.



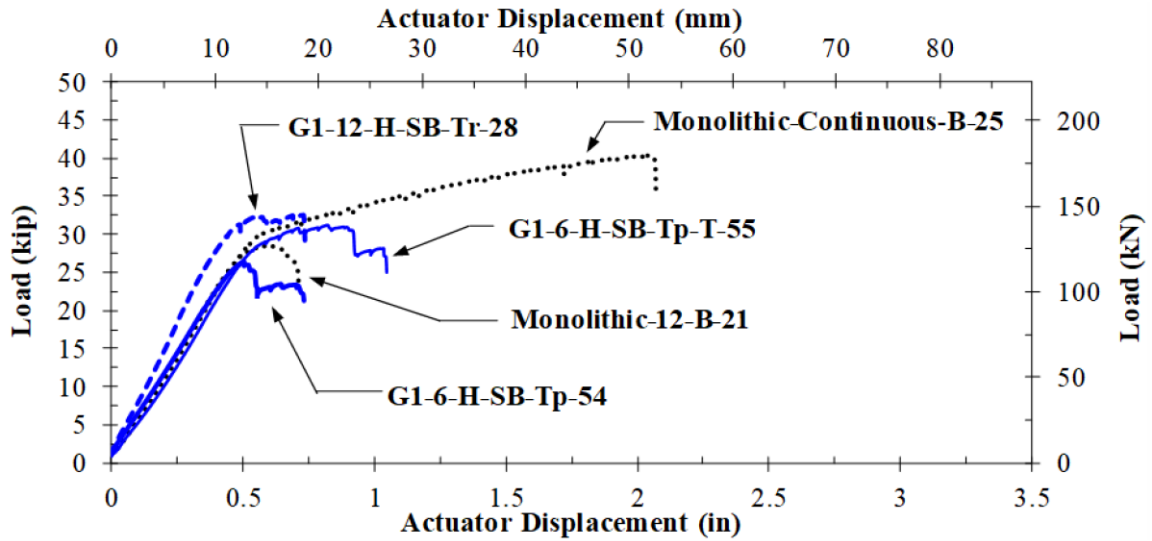
Source: FHWA

Figure 133. Photo. Representative photo of the observed failure of specimens with G1 grout and straight black bars after ultimate loading.

Deck panels employing headed bars did not exhibit substantial improvement in performance compared to panels with G1 grout and straight bars. As shown in figure 134, specimens G1-6-H-SB-Tp-54 and G1-12-H-SB-Tp-28 exhibited force-displacement curves that were comparable to that exhibited by G1-15-B-SB-Tp-6. That is, both panels appeared to reach yielding of the steel but failed shortly thereafter as a result of bond failure in the connection region. Thus, very little ductility was developed.

There was a single specimen, G1-6-H-SB-Tp-T-55, that employed headed bars and had transverse reinforcement within the connection region. It was apparent that the addition of transverse reinforcement may have moderately improved the ductility and load-bearing capacity of the specimen compared with G1-6-H-SB-Tp-54, which had the same combination of variables with the exception of transverse joint reinforcement. However, performance was still not comparable with that of Monolithic-Continuous-B-25.

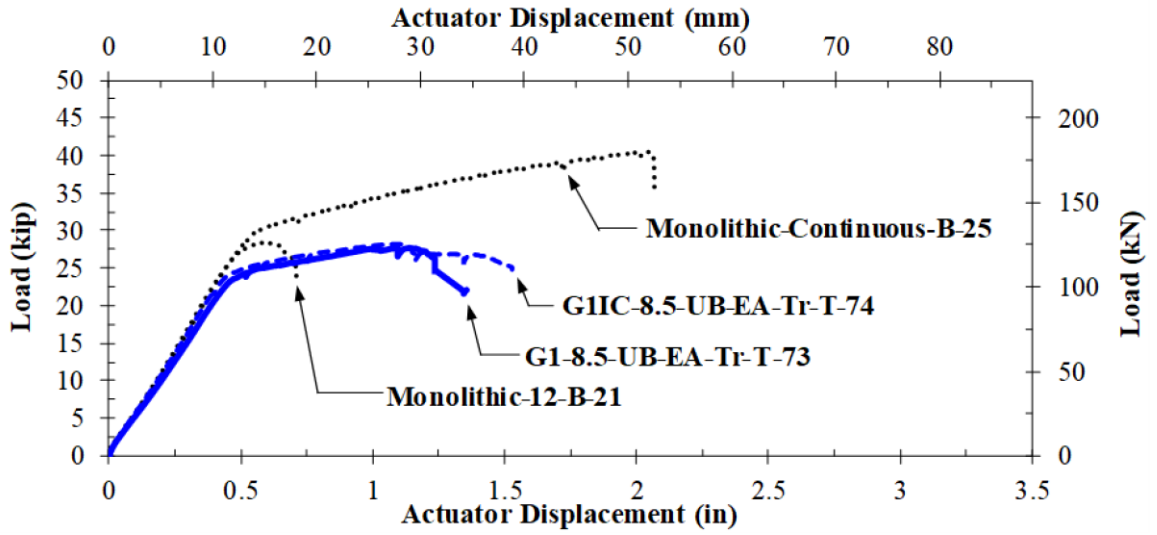
Analysis of force-displacement data indicated that the precast concrete surface preparation and shear key geometry did not influence the ultimate loading behavior of the deck specimens with G1 grout. Although deck panels with longer splice lengths and headed bars with transverse joint reinforcement did exhibit minor improvements in performance, the behavior of the panels was primarily governed by the G1 grout itself. Panels that survived fatigue loading exhibited significant damage within the grouted connection region at the start of the monotonic loading. As a result, these panels were susceptible to premature flexural failure and poor ductility.



Source: FHWA

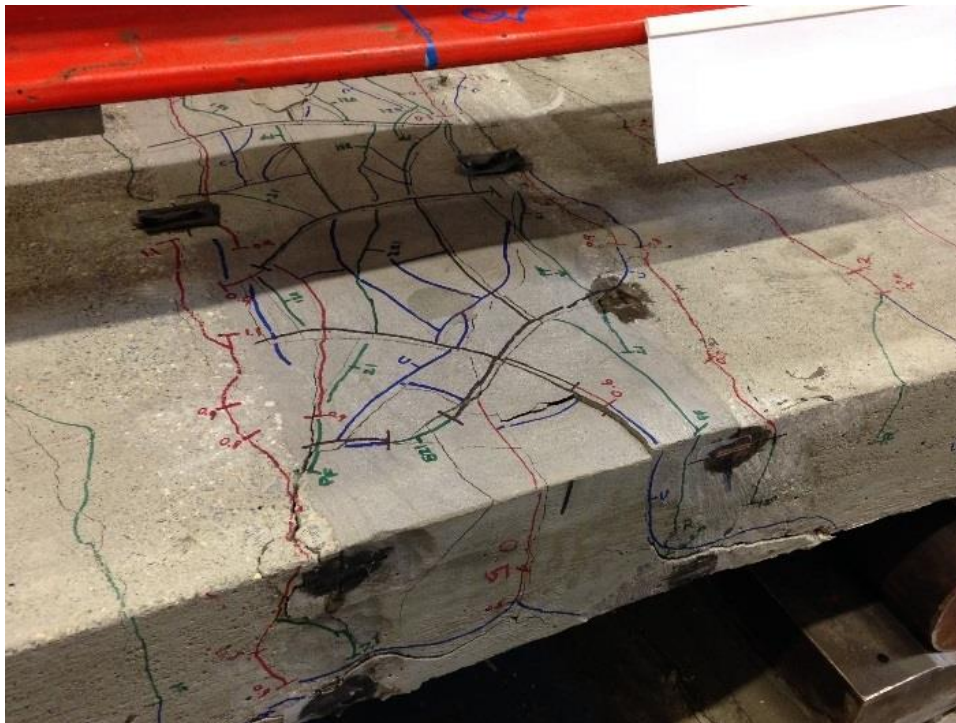
Figure 134. Graph. Force-displacement relationships from specimens with G1 grout and headed bars.

Deck panels employing U-bars exhibited improvement compared with specimens with straight bars and headed bars. As shown in figure 135, specimens G1-8.5-UB-EA-Tr-T-73 and G1IC-8.5-UB-EA-Tr-T-74 exhibited yielding of the steel and significant post-yield displacement capacity. Both specimens failed as a result of concrete crushing as shown in figure 136 and figure 137. Thus, both specimens achieved ductile behavior prior to failure and a desirable failure mode. After loading, both specimens exhibited significant cracking within the connection region, which is expected. Both specimens exhibited lower load-carrying capacity than the control specimen. This is in part due to the differences in the actual yield strength of the steel. The reinforcing bars in the control specimen had a slightly higher yield strength than those used in the specimens with U-Bar; see table 5.



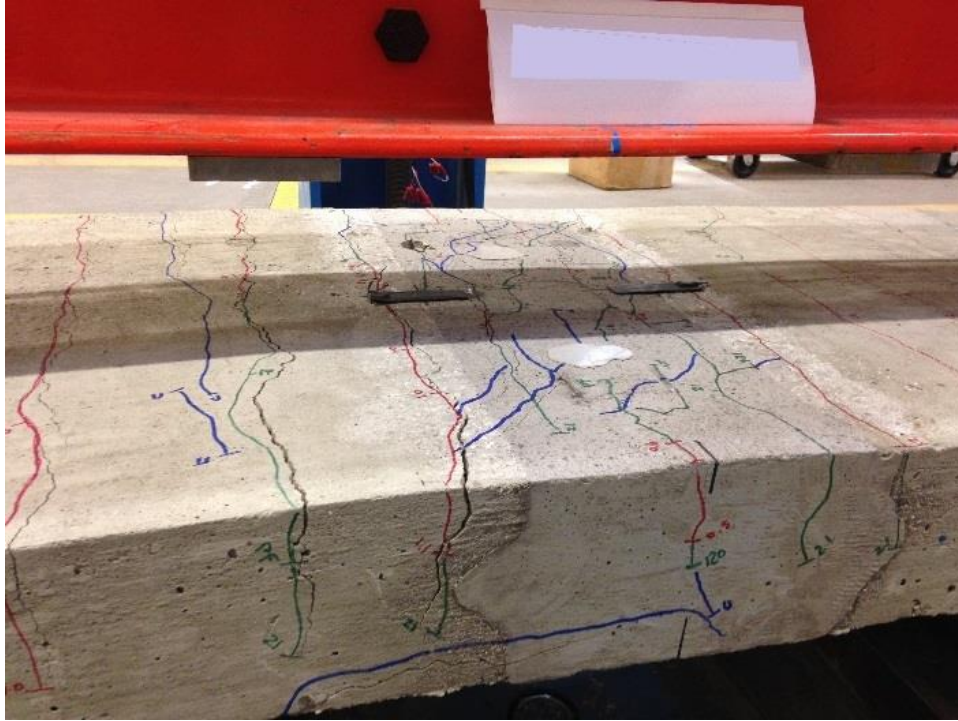
Source: FHWA

Figure 135. Graph. Force-displacement relationships from specimens with G1 grout and U-bars.



Source: FHWA

Figure 136. Photo. Specimen G1-8.5-UB-EA-Tr-T-73 after ultimate loading.



Source: FHWA

Figure 137. Photo. Specimen G11C-8.5-UB-EA-Tr-T-74 after ultimate loading.

Precast Deck Panel Specimens with E1 Grout and Mild Steel Bars

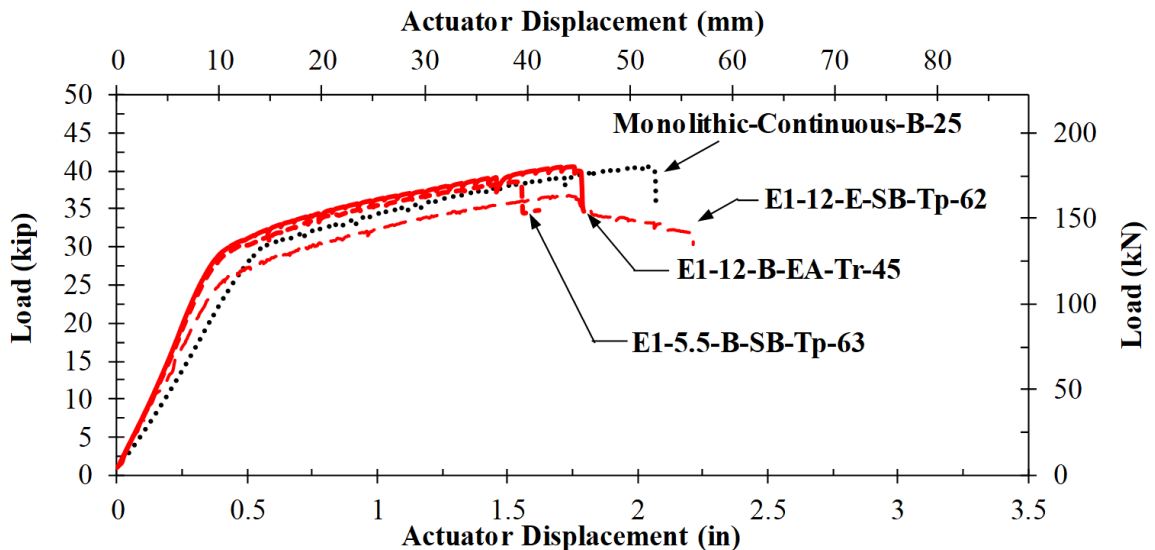
Deck panels specimens employing E1 grout in the connection region performed well in the ultimate load tests. All panels exhibited apparent yield strength, ultimate strength, and displacement ductility that were similar to Monolithic-Continuous-B-25. With the exception of panels with 5.5-inch (140-mm) lap splice lengths, all specimens failed as a result of concrete crushing.

The force-displacement curves for three representative specimens with E1 grout are shown in figure 138; Monolithic-Continuous-B-25 is also shown for comparison. Of the three E1 specimens shown, two employed black rebar with different splice lengths, E1-5.5-B-SB-Tp-63 and E1-12-B-EA-Tr-45, and the third, E1-12-E-SB-Tp-62, employed epoxy-coated bars and a 12-inch (305-mm) splice length. Specimen E1-5.5-B-SB-Tp-63, which used a 5.5-inch (140-mm) lap splice length, had a force-displacement response that was similar to the control specimen, Monolithic-Continuous-B-25; the initial and post-yielding stiffness were comparable along with the ultimate load capacity. After testing, inspection of E1-5.5-B-SB-Tp-63 revealed large longitudinal cracks on the tensile face of the E1 grout and areas on the compression face where the concrete and grout had been crushed (figure 139). Thus, it was difficult to characterize the failure mode of E1-5.5-B-SB-Tp-63, which may have been concrete/grout crushing, bar pull-out, or interaction between the two. Furthermore, the longitudinal cracks were not parallel to the

longitudinal reinforcing bars—instead they were inclined. This could have been a result of imbalanced loading, which would result in slight torsional effects, or it could be a result of the offset reinforcing bars. Conversely, panels with 12-inch (305-mm) lap splice lengths, E1-12-B-EA-Tr-45 and E1-12-E-SB-Tp-62, failed as a result of concrete crushing, as shown in figure 140. The measured force-displacement curves for these specimens closely resembled that of Monolithic-Continuous-B-25. The use of epoxy coated bars in specimens with E1 grout and 12-inch (305-mm) lap splice length, as shown in figure 138, had little influence on the ultimate performance of the deck panel.

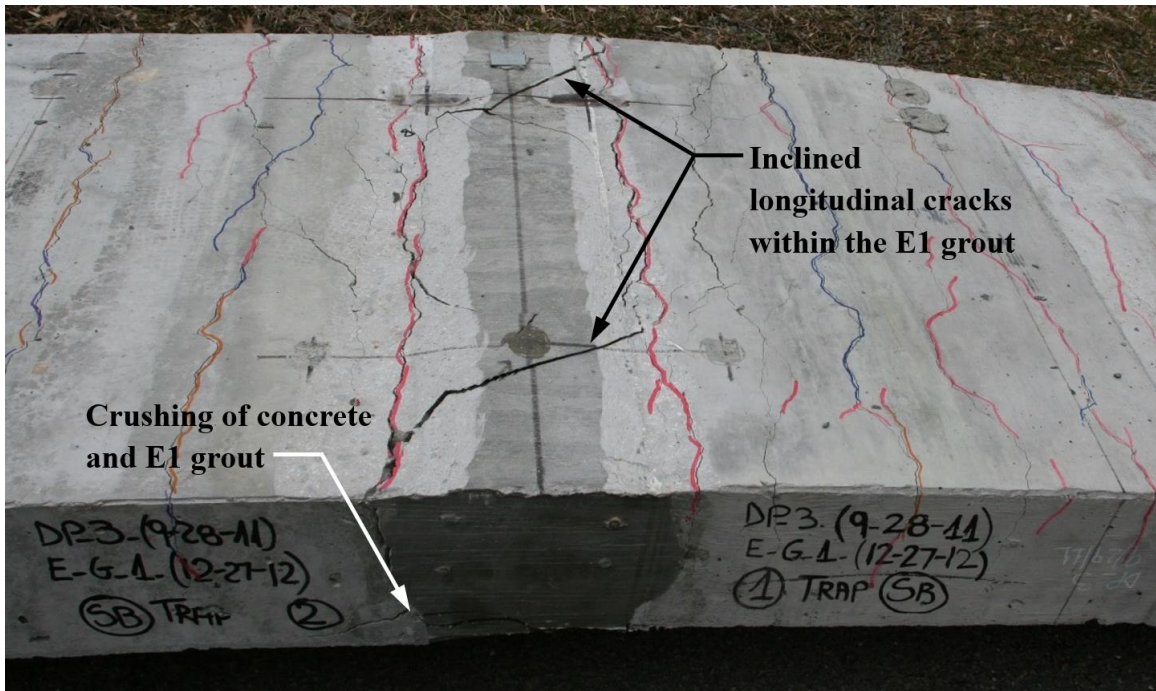
Two deck panels with E1 grout employed headed longitudinal bars: E1-5.5-H-SB-Tp-44 and E1-12-H-SB-Tp-40. As shown in figure 141, both specimens exhibited comparable force-displacement relations with the monolithic control panel Monolithic-Continuous-B-25, which indicates good performance. After testing, inspection of E1-5.5-H-SB-Tp-44 revealed concrete/grout crushing and longitudinal cracking similar to E1-5.5-B-SB-Tp-63 (see figure 139). Specimen E1-12-H-SB-Tp-40 failed as a result of concrete crushing in the precast deck panel.

Post-test inspection of panels with 12-inch (305-mm) splice lengths revealed that little to no cracking occurred within the E1 grout during ultimate loading. In some cases, a flexural crack was observed to form in the E1 grout adjacent to the concrete-grout interface, but cracks mostly formed within the precast deck panel. It was also determined that the surface preparation of the precast concrete and the shear key geometry had no effect on the ultimate flexural behavior of deck panels with E1 grout.



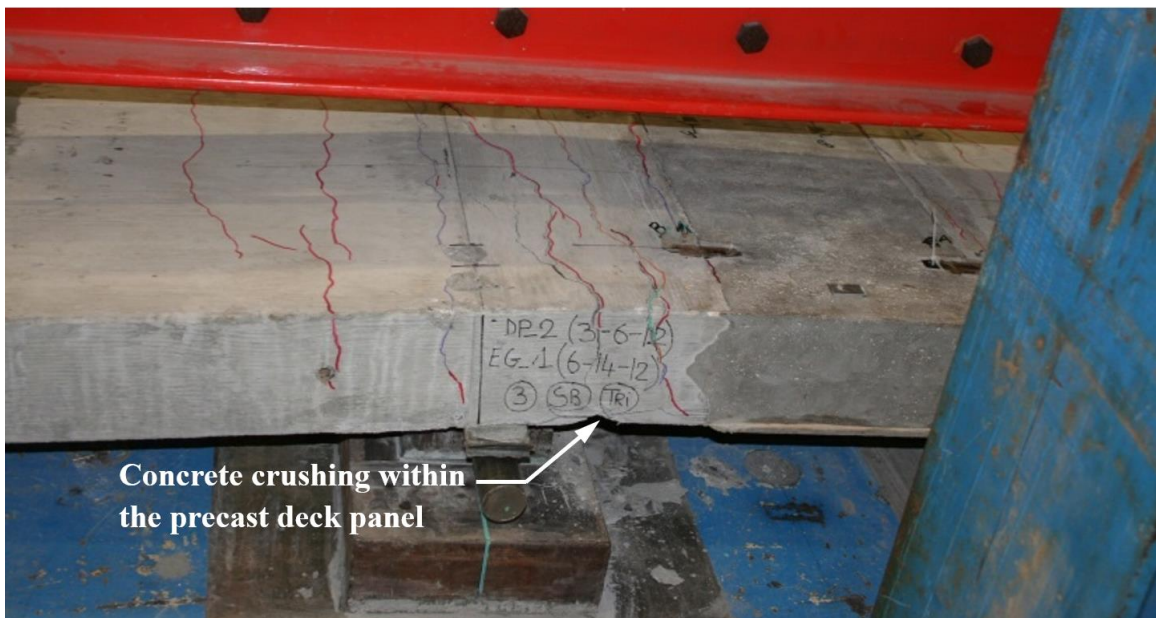
Source: FHWA

Figure 138. Graph. Force-displacement relationships from specimens with E1 grout and black and epoxy-coated bars.



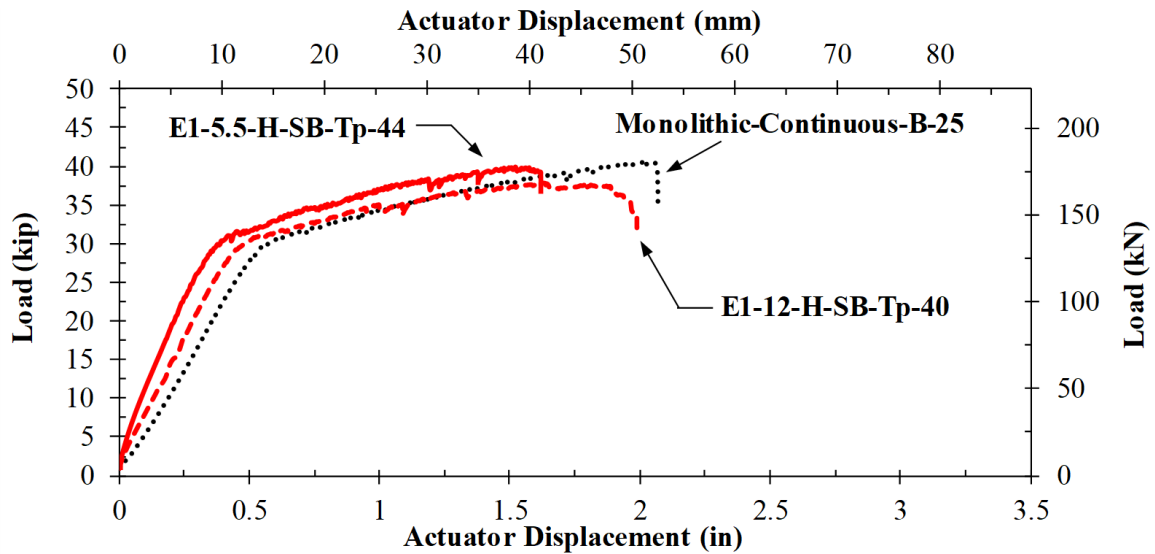
Source: FHWA

Figure 139. Photo. Observed failure of specimens with E1 grout and 5.5-inch (140-mm) splice lengths (Specimen E1-5.5-B-SB-Tp-63 shown).



Source: FHWA

Figure 140. Photo. Observed failure of specimens with E1 grout and 12-inch (305-mm) splice lengths.



Source: FHWA

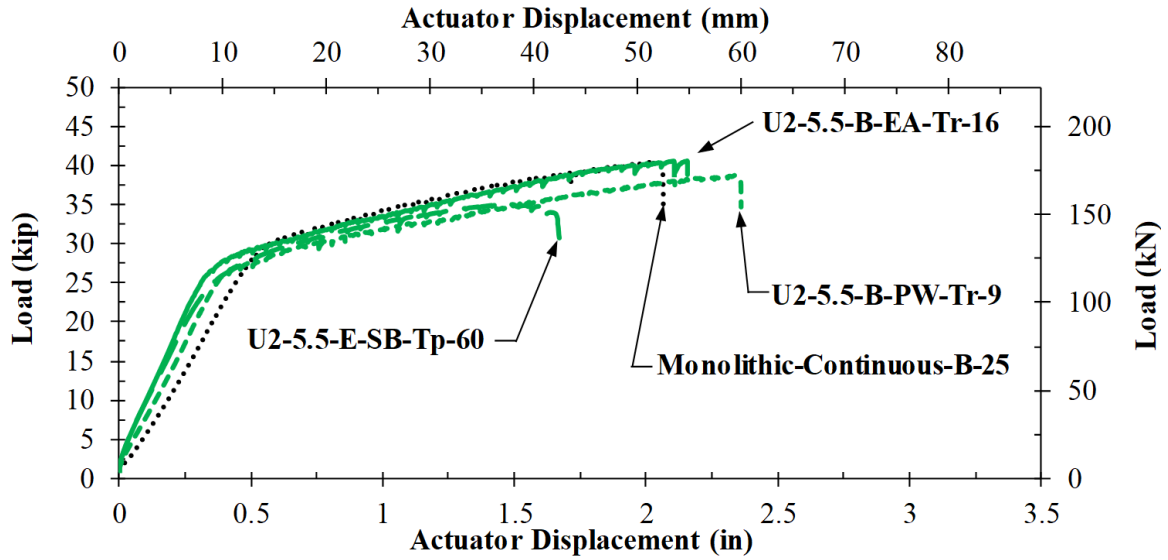
Figure 141. Graph. Force-displacement relationships from specimens with E1 grout and headed bars.

Precast Deck Panel Specimens with U2 Grout and Mild Steel Bars

Deck panels specimens employing U2 grout in the connection region performed well in the ultimate load tests. All panels exhibited apparent yield strength, ultimate strength, and displacement ductility that were similar to Monolithic-Continuous-B-25, and all panels failed by crushing of the concrete.

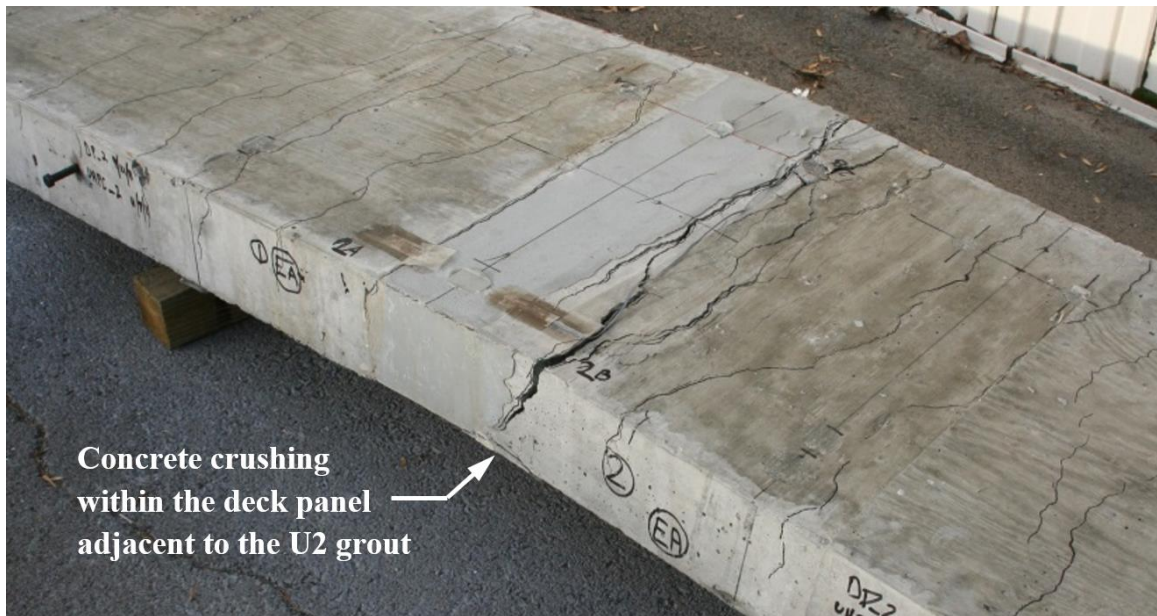
The force-displacement relationships for two representative panels with U2 grout are shown along with Monolithic-Continuous-B-25 in figure 142. It can be observed that the behavior of both panels is comparable to the monolithic control panel. All three panels exhibit similar pre- and post-yielding stiffness as well as comparable ultimate loads and displacements. All panels with black bars and U2 grout failed as a result of concrete crushing. In most cases, crushing occurred within the precast deck panel adjacent to the grouted connection region as shown in figure 143. Otherwise, the crushing of the concrete occurred near the supports at mid-span.

Post-testing inspection of panels revealed that little to no cracking occurred within the U2 grout during ultimate loading. In some cases, wide flexural cracks formed at the interface between the precast concrete and U2 grout, but for the most part cracks formed within the precast deck panel. It was also determined that the surface preparation of the precast concrete and the shear key geometry had no effect on the ultimate flexural behavior of the deck panels with U2 grout.



Source: FHWA

Figure 142. Graph. Force-displacement relationships from specimens with U2 grout and black or epoxy-coated bars.



Source: FHWA

Figure 143. Photo. Representative photo of the observed failure of specimens with U2 grout after ultimate loading.

Monolithic and Precast Deck Panel Specimens with GFRP Bars

Four deck panel specimens employed GFRP reinforcing bars in place of mild steel bars. One panel, Monolithic-Continuous-G-67, was cast monolithically with continuous bars and served as the baseline panel. The nominal moment capacity of the baseline panel was 77 kip-ft (104 kN-m), which corresponded to 34.2 kips (152 kN) of actuator force. The remaining three panels were precast with lap-spliced bars within the connection region and employed G1, E1, or U2 grout; a single specimen was tested for each grout type.

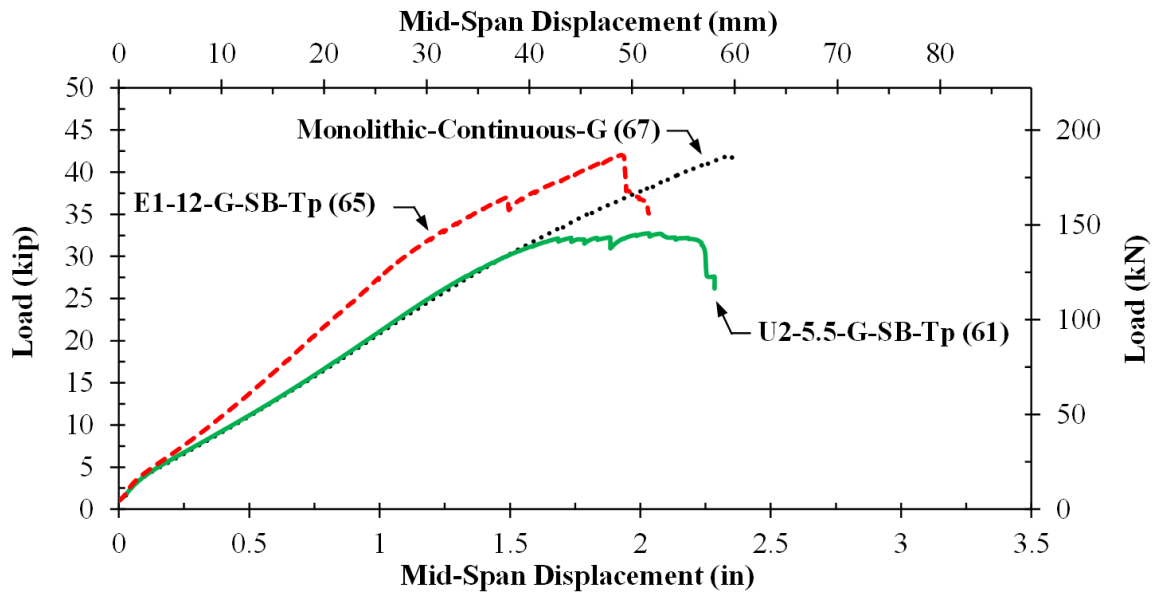
The force-displacement curves for Monolithic-Continuous-G-67, E1-12-G-SB-Tp-65 and U2-5.5-G-SB-Tp-61, are shown in figure 144. The specimen employing G1 grout in the connection region failed during fatigue loading and is consequently not shown. The response of Monolithic-Continuous-G-67 was approximately linear until failure. The ultimate capacity was 41.9 kips (186 kN), which exceeded the nominal capacity. The baseline panel formed a wide shear crack adjacent to the support that continued to open during loading. Shear failure ultimately occurred when GFRP reinforcing bars fractured under dowel action and a portion of the specimen separated from the remainder of the deck panel (see figure 145). After testing, numerous flexural cracks were observed within both the constant moment region and in the shear spans.

The force-deformation response of E1-12-G-SB-Tp-65 was approximately linear until failure despite some slight variations in flexural stiffness. A small drop in load was recorded at 37 kips (165 kN) when a full-depth shear crack developed near the support. The load loss was recovered, and the specimen eventually failed in shear similar to that of the baseline specimen (see figure 146). The ultimate load achieved by E1-12-G-SB-Tp-65 was 42 kips (187 kN). Although wide flexural cracks had formed at the concrete-grout interface, there were no visible cracks or distress within the E1 grout.

The force-deformation response of U2-5.5-G-SB-Tp-61 was identical to that of the baseline specimen until the applied load reached 30 kips (133 kN) with a corresponding vertical displacement of 1.7 inches (43.2 mm). After this point, the panel quickly softened and the subsequent response was approximately perfectly plastic. Small load gains and losses occurred as the panel underwent an additional 0.5 inches (12.7 mm) deflection until failure occurred. The maximum recorded load and displacement achieved by U2-5.5-G-SB-Tp-61 were 32.7 kips (145 kN) and 2.28 inches (57.9 mm), respectively.

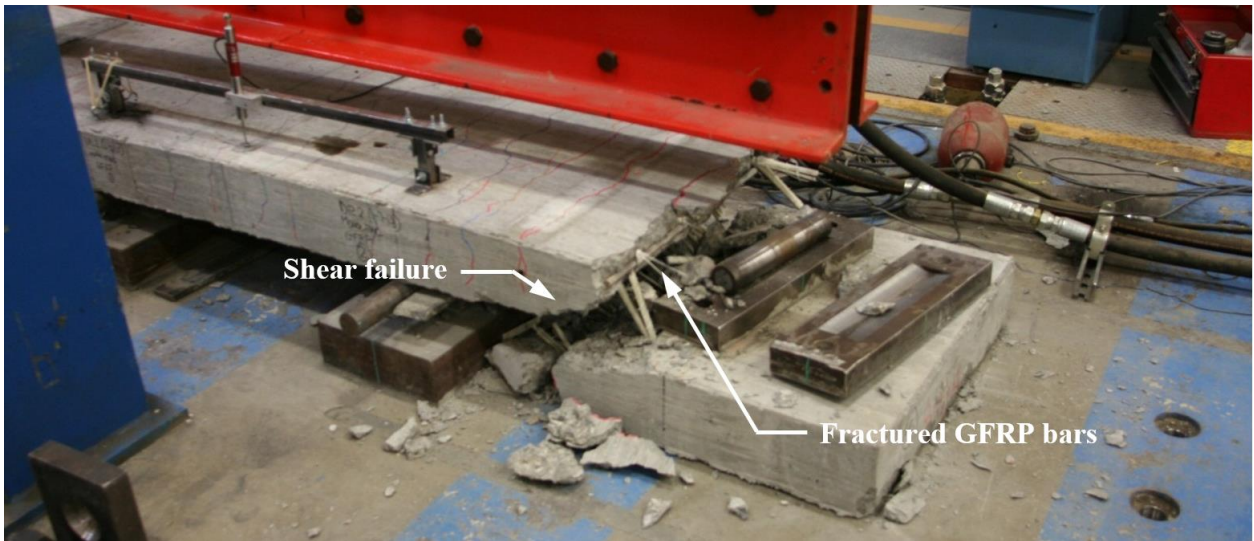
After testing, U2-5.5-G-SB-Tp-61 was inspected. A wide flexural crack had formed along one of the concrete-grout interfaces on the tension face of the specimen, and crushed concrete was observed along the corresponding compression face (see figure 147-A). Portions of concrete and U2 grout were removed from the tension face the specimen to determine whether failure resulted from bar rupture or pull-out. Once the concrete was removed, two out of four GFRP bars were found to have fractured, whereas the bond between the bars and the U2 grout appeared sound (see figure 147-B). Thus, the failure of U2-5.5-G-SB-Tp-61 was ultimately caused by bar

fracture, not bond failure. Other than interface cracking, there was neither cracking nor distress observed within the U2 grout material after the ultimate loading.



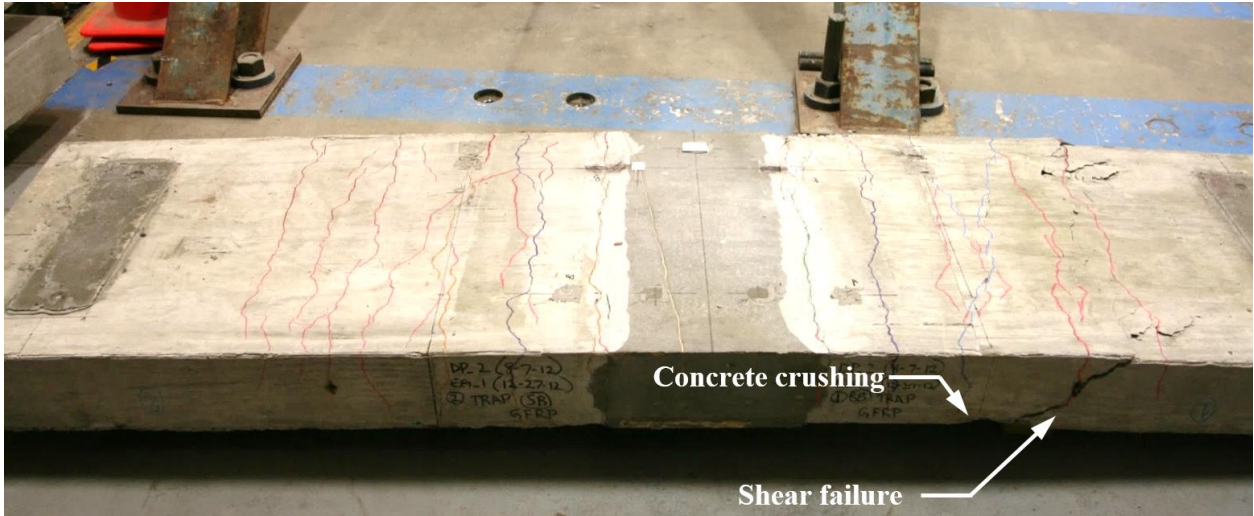
Source: FHWA

Figure 144. Graph. Force-displacement relationships from specimens with GFRP bars.



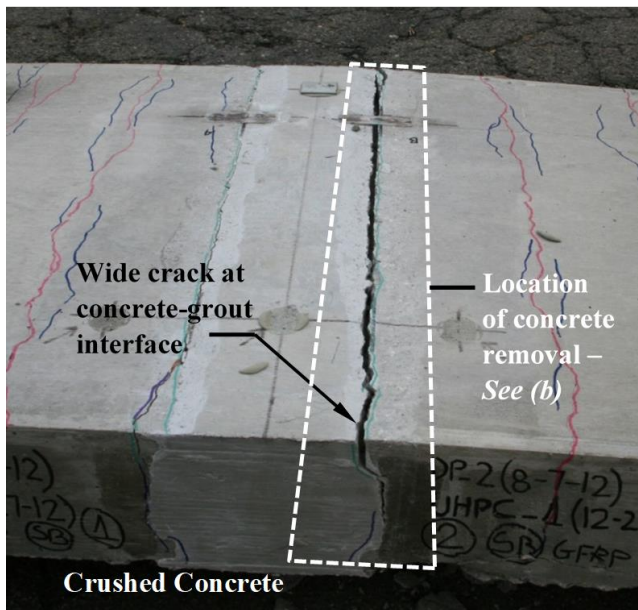
Source: FHWA

Figure 145. Photo. Failure of Monolithic-Continuous-G-67.



Source: FHWA

Figure 146. Photo. Failure of E1-12-G-SB-Tp-65.



A. After testing



B. Inspection after concrete removal

Source: FHWA

Figure 147. Photos. Failure of U2-12-G-SB-Tp-61.

Overall Comparison of Ultimate Flexural Behavior

The ultimate load capacity of the deck-level connection specimens is compared in figure 149 through figure 151. Specimens were grouped according to grout type, and the measured ultimate load of each precast panel specimen was normalized with respect to the ultimate load achieved

by the baseline monolithic panel with continuous bars, Monolithic-Continuous-B-25. Thus, these figures display both the measured ultimate loads and the metric used for comparison, which is the normalized ultimate load. This metric is defined by the equation shown in figure 148. To aid interpretation, reference lines are also shown for the nominal yield point and for the response of Monolithic-12-B-21.

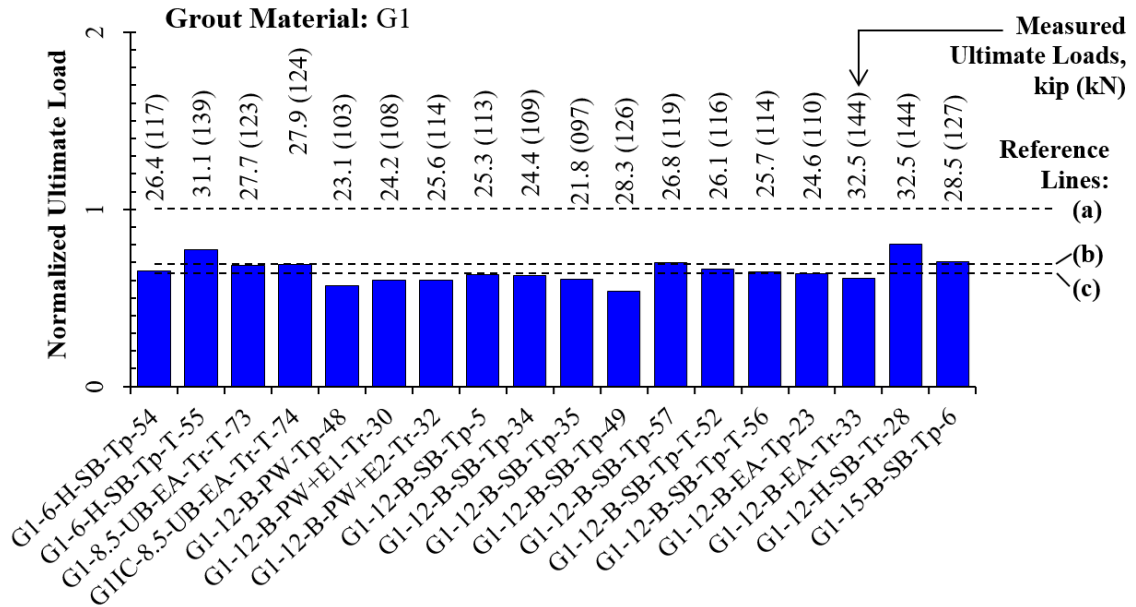
$$\text{Normalized Ultimate Load} = \frac{P_{U, \text{Specimen}}}{P_{U, \text{Control}}}$$

Figure 148. Equation. Normalized ultimate load.

Where

$P_{U, \text{Specimen}}$ = Measured ultimate load of a given deck-level connection specimen

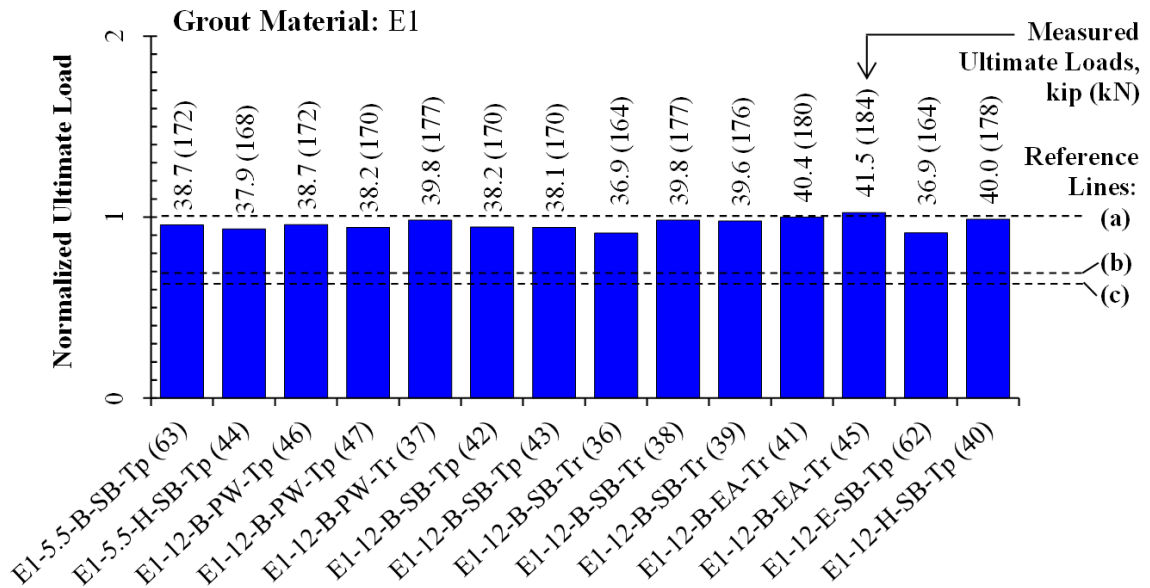
$P_{U, \text{Control}}$ = Measured ultimate load of the baseline deck panel specimen, Monolithic-Continuous-B-25



Reference Lines: (a) Measured ultimate load from the control specimen Monolithic-Continuous-B-25= 40.5 kips (180 kN); (b) Measured ultimate load from specimen Monolithic-12-B-21 = 28.5 kips (128 kN); and (c) Calculated yield point of 26.5 kips (118 kN).

Source: FHWA

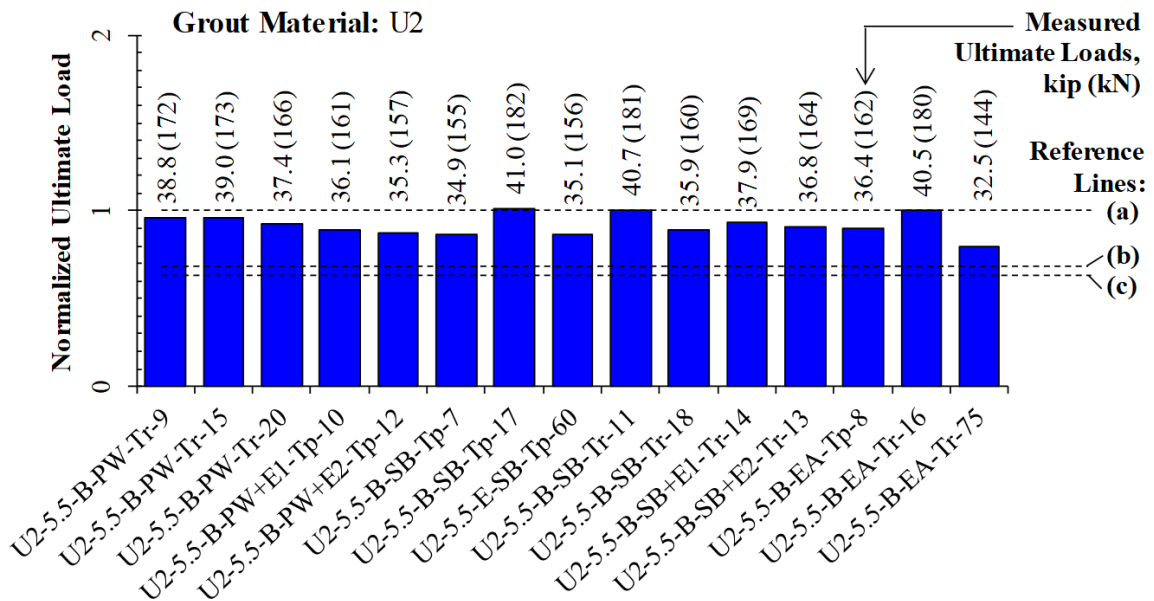
Figure 149. Graph. Ultimate loads of deck-level connection specimens with G1 grout.



Reference Lines: (a) Measured ultimate load from the control specimen Monolithic-Continuous-B-25= 40.5 kips (180 kN); (b) Measured ultimate load from specimen Monolithic-12-B-21 = 28.5 kips (128 kN); and (c) Calculated yield point of 26.5 kips (118 kN).

Source: FHWA

Figure 150. Graph. Ultimate loads of deck-level connection specimens with E1 grout.



Reference Lines: (a) Measured ultimate load from the control specimen Monolithic-Continuous-B-25= 40.5 kips (180 kN); (b) Measured ultimate load from specimen Monolithic-12-B-21 = 28.5 kips (128 kN); and (c) Calculated yield point of 26.5 kips (118 kN).

Source: FHWA

Figure 151. Graph. Ultimate loads of deck-level connection specimens with U2 grout.

The estimated displacement ductility of the deck-level connection specimens is compared in figure 153 through figure 155. Specimens were grouped according to grout type, and estimated displacement ductility of each precast panel specimen was normalized with respect to the estimated displacement ductility achieved by the baseline monolithic panel with continuous bars, Monolithic-Continuous-B. Thus, these figures display both the estimated displacement ductility and the metric used for comparison, which is the normalized ductility. This metric is defined by the equation shown in figure 152. To aid interpretation, reference lines are also shown for the ductility of specimens Monolithic-Continuous-B-25 and Monolithic-12-B-21. Some specimens with G1 grout did not exhibit an apparent yield point and thus do not exhibit ductility. The results for these specimens are shown as “No Yielding.”

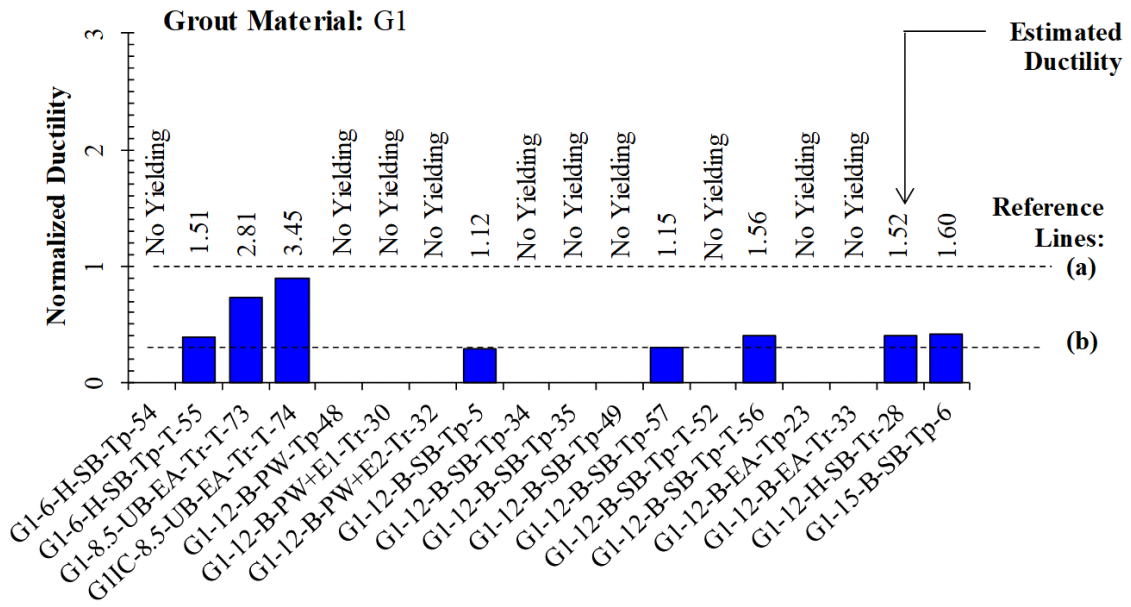
$$\text{Normalized Ductility} = \frac{\mu_{\text{Specimen}}}{\mu_{\text{Control}}}$$

Figure 152. Equation. Normalized ultimate load.

Where

μ_{Specimen} = Estimated displacement ductility of a given deck-level connection specimen as defined by the equation in figure 129.

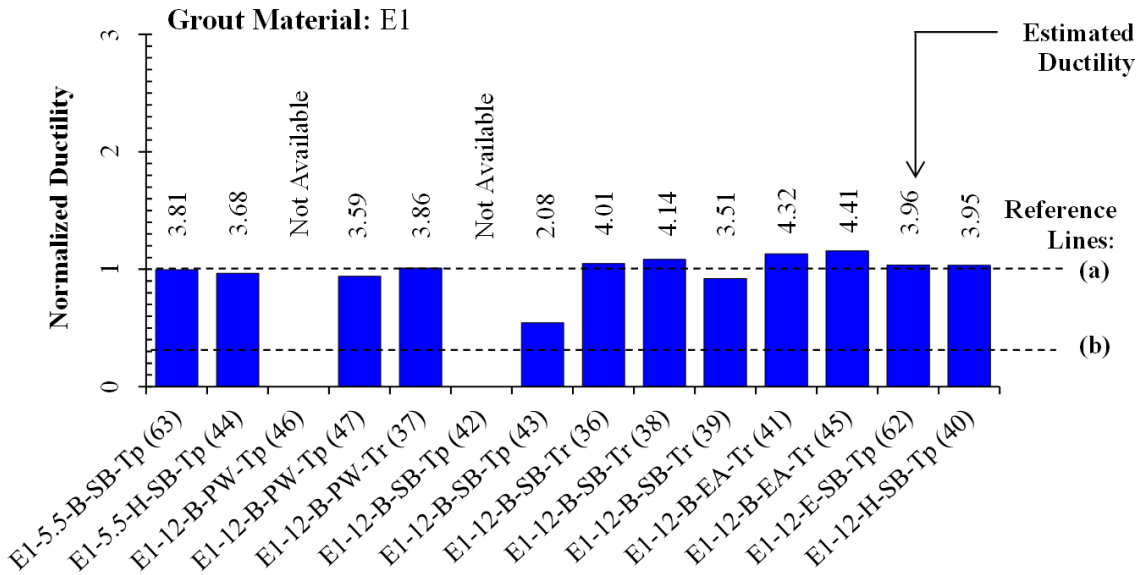
μ_{Control} = Estimated displacement ductility of the baseline deck panel specimen, Monolithic-Continuous-B-25, as defined by the equation in figure 129.



Reference Lines: (a) Estimated displacement ductility of the control specimen Monolithic-Continuous-B-25 = 3.86; and (b) Estimated displacement ductility of specimen Monolithic-12-B-21 = 1.25.

Source: FHWA

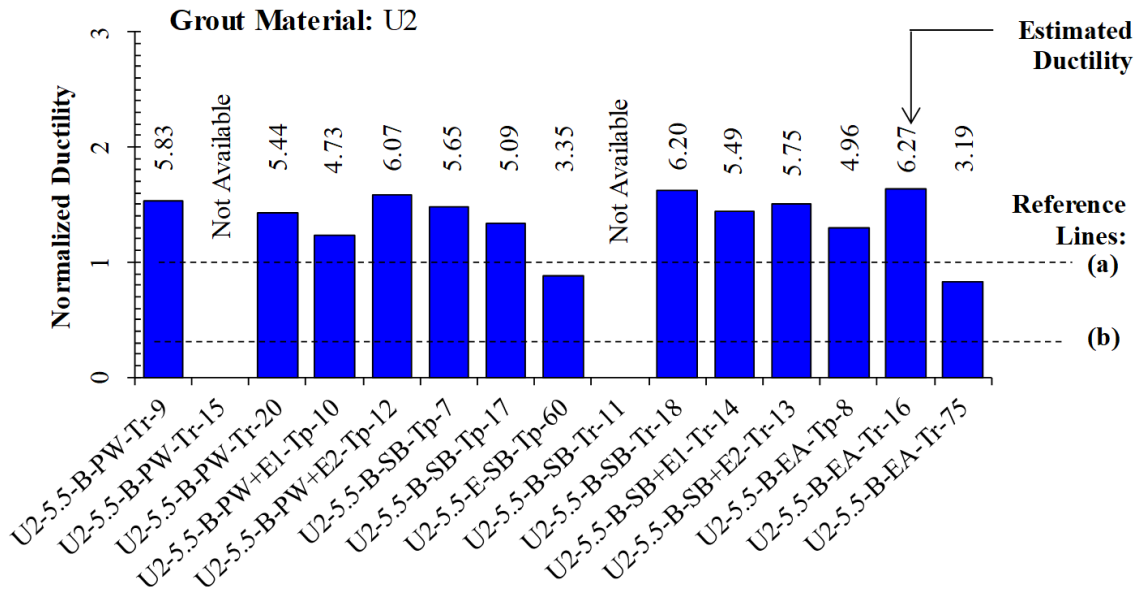
Figure 153. Graph. Estimated displacement ductility of deck-level connection specimens with G1 grout.



Reference Lines: (a) Estimated displacement ductility of the control specimen Monolithic-Continuous-B-25 = 3.86; and (b) Estimated displacement ductility of specimen Monolithic-12-B-21 = 1.25.

Source: FHWA

Figure 154. Graph. Estimated displacement ductility of deck-level connection specimens with E1 grout.



Reference Lines: (a) Estimated displacement ductility of the control specimen Monolithic-Continuous-B-25 = 3.86; and (b) Estimated displacement ductility of specimen Monolithic-12-B-21 = 1.25.

Source: FHWA

Figure 155. Graph. Estimated displacement ductility of deck-level connection specimens with U2 grout.

CHAPTER 6. SUMMARY AND CONCLUSIONS

SUMMARY

This report discussed the findings of an extensive research project carried out at the FHWA Turner-Fairbank Highway Research Center to advance the understanding of deck-level connections for prefabricated bridge decks. A number of parameters frequently considered during the design of these connections, including shear key shape, reinforcement type, connection grout material type, precast surface preparation, and transverse reinforcement were investigated. Variables were selected to be representative of materials that are currently being used or that show significant promise for use with prefabricated concrete bridge deck systems.

The research program was executed in two phases such that both local and global behavior of these connections could be investigated. The first phase, referred to as “Bond Characterization Testing,” utilized small-scale specimens with geometric details and loading protocols that were based on currently available ASTM standard test methods. Three different test methods were used to study the bond behavior between precast concrete and grout: a flexural beam (modified from ASTM C78), a splitting cylinder (modified from ASTM C496), and a slant shear cylinder (modified from ASTM C882). Bond characterization tests investigated how bond behavior was affected by different combinations of grout materials and precast concrete surface preparations. A secondary objective of these tests was to investigate the applicability of each test method for evaluating the tensile strength of the grout-to-precast concrete bond.

In the second phase of the program, referred to as “Deck-Level Connection Testing,” 75 large-scale deck-level connection assemblies were tested in four-point bending and then were subjected to cyclic crack loading, fatigue loading, and monotonic loading until failure. The three loading protocols enabled assessment of the connection parameters as they related to durability, serviceability, and ultimate strength.

KEY OBSERVATIONS

The following key observations were made based on the parameters investigated during the course of this study:

Bond Characterization Tests

Cementitious grouts G1 and M1 showed poor bond performance regardless of the precast concrete surface preparation, although the bond was nominally improved by the use of exposed aggregate surface preparation.

The bond performance of the UHPC grout, U2, was found to be dependent on the surface preparation, and the bond strength could be enhanced by increasing the surface roughness of the precast concrete. The use of U2 grout in conjunction with exposed aggregate surface preparation

could provide sufficient bond strength such that the tensile strength of precast concrete can be developed.

Bond strength between the precast concrete and G1, M1, or U2 grout was dependent on the age of the grout material. As the grout material matured, bond strength increased.

Epoxy grout, E1, was found to bond very well with precast concrete. Furthermore, the bond strength of E1 grout to precast concrete was independent of investigated surface preparation methods or the age of the material.

The flexural beam test produced consistent results as compared to the splitting cylinder and slant shear bond tests. However, the specimen size resulted in handling issues and premature failure of many specimens prior to testing. Therefore, a smaller beam sample may need to be considered, but would need to be evaluated and compared with available test results.

Splitting tensile tests did not indicate significant differences in bond strength as a result of the different surface preparation methods investigated. Computational modelling showed that differential stiffness between cylinder halves could affect the stress distribution across the interface of the two materials resulting in potentially incorrectly interpreted bond strengths.

The slant shear test does indicate differences in bond strength with respect to the surface preparation method and grout material. However, the stress state is more complex at the interface of the two materials due to shear friction, and therefore results could be misinterpreted.

Deck Panel Connection Tests

Pre-Test Inspection

A significant number of the specimens employing a non-shrink cementitious grout, G1, exhibited shrinkage cracking within the field-cast grout and along the interface between the precast concrete and the field-cast grout.

The performance of conventional non-shrink connection grouts can be improved by providing internal curing (IC). The addition of IC significantly reduces both autogenous and drying shrinkage, which can reduce shrinkage cracking in the connection region.

Approximately one-third of the specimens employing U2 grout exhibited fine shrinkage cracks within the field-cast grout. However, specimens that exhibited shrinkage cracks did not have apparent cracking at the interface between the precast concrete and U2 grout.

With the exception of a single specimen with E1 grout, specimens employing M1 and E1 grouts did not exhibit shrinkage cracking within the field-cast grout.

Pre-Cracking Cyclic Loading

Visual inspection indicated that the majority of deck panel specimens had cracking at the concrete-grout interface after the $0.8M_{cr}$ load cycles. Data analysis further indicated that some specimens employing G1, M1, and U2 grout may have cracked at the concrete-grout interface as early as $0.5M_{cr}$ assuming interface cracking was not caused by shrinkage.

Epoxy grout, E1, exhibited good bond performance under cyclic crack loading. In most cases, strains across the concrete-grout interface were small and comparable with those calculated for an uncracked section. There was also good correlation between interface cracking that was identified by observation and that was identified by data analysis.

Connections with U2 grout showed that the bond strength of the concrete-grout interface could be improved with exposed aggregate surface preparation.

Unlike the specimens employing M1, E1, and U2 grouts, which exhibited little to no cracking within the grouted connection region after the crack loading protocol, specimens with G1 grout exhibited significant flexural cracking and numerous splitting cracks within the grouted connection materials. Some of these cracks nucleated from existing shrinkage cracks, which in turn reduced initial element stiffness. The use of IC tended to reduce shrinkage cracking in the connection region, which enhanced the initial stiffness of the connection.

Shear key geometry, transverse reinforcement, splice length, and reinforcing bar type had a negligible effect on the behavior of deck-level connection specimens when subjected to the cyclic crack loading.

Post-Cracking Fatigue Loading

Specimens employing G1 grout that failed during fatigue loading had exhibited more shrinkage cracks compared with specimens that survived the loading protocol; these specimens also employed straight bar lap splices with lengths equal to or less than 12 inches (305 mm). Failure of these specimens was a result of lap splice failure. This was caused by formation of splitting cracks in the connection grout that reduced bar confinement thus leading to a lap splice failure.

Specimens with G1 grout that survived fatigue loading exhibited a distinct progression of damage that began with crack formation caused by shrinkage and pre-crack cyclic loading. During the post-cracking fatigue cycles, cracks continued to grow with the increasing number of cycles. At the conclusion of the loading protocol, cracking within the grouted regions was extensive. Specimens employing lap splices with additional anchorage, such as headed or U-bars, all survived the post-cracking fatigue loading protocol. It was determined that connections employing U-bar lap splices exhibited good stiffness retention.

All specimens employing M1 grout failed early in the fatigue loading as a result of lap splice failure. Grout strength appeared to partially influence the number of cycles sustained prior to failure.

All specimens employing E1 and U2 grouts survived the fatigue loading protocol with minimal damage to the connection grout. However, in most cases, by the end of the fatigue loading protocol, the existing cracking in the vicinity of the concrete-grout interface had grown to span the entire width of each deck panel specimen. This cracking occurred either at the interface or within the precast concrete adjacent to the concrete-grout interface depending on the precast concrete surface preparation.

Monotonic Ultimate Loading

Precast concrete surface preparation and shear key geometry had no influence on the ultimate flexural performance of the deck-level connections regardless of grout material, lap splice length, or use of transverse reinforcement with the connection.

Deck level connections employing G1 grout that used longer lap splice lengths and headed bars with transverse reinforcement exhibited nominal improvement in the ultimate loading performance over other parameter combinations using G1 grout. However, in general, the ultimate performance of specimens with G1 grout was poor compared to the monolithic panels with continuous bars or with adequately developed lap-spliced bars. The majority of the specimens with G1 grout failed prior to achieving the nominal yield moment of the deck panel. Most of these specimens exhibited bond failure due to insufficient lap splice anchorage. Headed bars provided nominal performance enhancement, while the specimens with U-bars exhibited increased ductility. Use of IC to enhance the performance of the G1 connection grout was not found to negatively impact the ultimate behavior of the specimen (G1IC-8.5-UB-EA-Tr-T-74).

Specimens employing E1 and U2 grout exhibited ultimate performance that was comparable with the monolithic baseline specimens with continuous bars. These specimens were able to develop the full flexural capacity of the deck panel prior to failure, which was a result of concrete crushing, and exhibited good ductility with the exception of panels employing GFRP bars, which is to be expected.

Although the full flexural capacity of the deck panel was realized, specimens with E1 grout and 5.5-inch (140-mm) lap splice lengths exhibited splitting cracking within the grout material, which in other specimen types was related to lap splice.

CONCLUSIONS

The following conclusions can be made based on the key observations and findings of this study:

Test variables had varying influence on the behavior of the deck-level connections. Shear key geometry had little to no effect on the flexural performance of the deck-level connections tested in this study. Other parameters, such as precast concrete surface preparation and lap splice length, affected only certain aspects of the deck-level connection performance, such as cracking behavior and fatigue/ultimate behavior, respectively. The type of grout material used had a significant impact on all aspects of the deck-level connection performance. Thus, the selection of field-cast grout materials is one of the most critical design considerations for deck-level PBE connections.

Splitting cylinder and slant shear tests are not appropriate for evaluating the tensile bond resistance of grout-to-precast concrete joints. These tests produce somewhat complex stress states that result from local variations in material properties or precast concrete surface preparations, which can compromise results. The flexural beam tests, although more difficult to run successfully, provide a better alternative for evaluating the tensile bond of grouts to precast concrete surfaces.

Depending on the grout material selected for a deck-level connection, surface preparation of precast concrete deck panels can have a significant impact on the tensile bond resistance of the concrete-grout interface. The exposed aggregate surface preparation promotes the bonding conditions between the precast concrete components and cementitious grout connection materials.

Cementitious grouts are susceptible to premature failure under repeated loading as a result of the formation and propagation of cracks. Without confinement and/or fiber reinforcement, cracks cannot be arrested and will continue to grow with the number of load cycles. Both micro- and macro-scale cracks weaken the bond between the grout and load-carrying reinforcing bars, which may lead to premature performance degradation. However, the performance of these connections can be slightly enhanced by using lap splices with additional anchorage such as headed bars or U-bars.

Although epoxy and UHPC grout systems have higher initial cost, they could provide better value when constructability, long-term performance, and required maintenance are considered.

RECOMMENDATIONS

Careful thought must be given to the selection of field-cast grout materials for connecting PBES elements. Similarly, design details can play an important role in the behavior of connections. In order to maximize performance and minimize potential issues related to durability, exposed aggregate surface preparation should be provided on precast concrete deck panels surfaces that will be in contact with a cementitious field-cast grout within a connection region. Without compromising development of bars and connection strength, deck-level connections should be designed and detailed to minimize the distance between adjacent elements such that effects of

connection grout shrinkage/expansion can be minimized. Reinforcement detailing and lap splice lengths need to be considered in conjunction with the strength and materials characteristics of the intended field-cast grout systems to be used for connections.

ACKNOWLEDGMENTS

The research project discussed herein could not have been completed were it not for the dedicated support of the federal and contract staff associated with the FHWA Structural Concrete Research Program.

The publication of this report does not necessarily indicate approval or endorsement of the findings, opinions, conclusions, or recommendations either inferred or specifically expressed herein by the Federal Highway Administration or the United States Government.

REFERENCES

- AASHTO. 2010. *AASHTO LRFD Bridge Design Specifications*. 5th Edition. Washington, D.C.: American Association of State Highway and Transportation Officials.
- AASHTO. 2014. *AASHTO LRFD Bridge Design Specifications*. 6th edition. Washington, DC: American Association of State Highway and Transportation Officials.
- Abu-Tair, A. I., S. R. Rigden, and E. Burley. 1996. "Testing the Bond between Repair Materials and Concrete Substrate." *ACI Materials Journal* 93 (6): 553–58.
- ACI Committee 408. 2003. "Bond and Development of Straight Reinforcing Bars in Tension." 408R–03.
- ASTM A615 / A615M-16. 2016. *Standard Specification for Deformed and Plain Carbon-Steel Bars for Concrete Reinforcement*. West Conshohocken, PA: ASTM International.
- ASTM C78 / C78M-16. 2016. *Standard Test Method for Flexural Strength of Concrete (Using Simple Beam with Third-Point Loading)*. West Conshohocken, PA: ASTM International.
- ASTM C496 / C496M-11. 2004. *Standard Test Method for Splitting Tensile Strength of Cylindrical Concrete Specimens*. West Conshohocken, PA: ASTM International.
- ASTM C882 / C882M-13a. 2013. *Standard Test Method for Bond Strength of Epoxy-Resin Systems Used With Concrete By Slant Shear*. West Conshohocken, PA: ASTM International.
- ASTM C1581 / C1581M-09a. 2009. *Standard Test Method for Determining Age at Cracking and Induced Tensile Stress Characteristics of Mortar and Concrete under Restrained Shrinkage*. West Conshohocken, PA: ASTM International.
- ASTM C1856/C1586-17. 2017. *Standard Practice for Fabricating and Testing Specimens of Ultra-High Performance Concrete*. West Conshohocken, PA: ASTM International.
- Azizinamini, A., D. Darwin, R. Eligehausen, R. Paval, and S. K. Ghosh. 1999. "Proposed Modifications to ACI 318-95 Tension Development and Lap Splice for High-Strength Concrete." *ACI Structural Journal* 96 (6): 922–26.
- Badie, Sameh S., and Maher K. Tadros. 2008. *Full-Depth Precast Concrete Bridge Deck Panel Systems /: Sameh S. Badie and Maher K. Tadros*. NCHRP Report 584. Washington, D.C: Transportation Research Board.
- Bentz, Dale P, Pietro Lura, and John W Roberts. 2005. "Mixture Proportioning for Internal Curing." *Concrete International* 27 (2): 35–40.
- Bentz, Dale P, and W Jason Weiss. 2011. "Internal Curing: A 2010 State-of-the- Art Review." *National Institute of Standards and Technology (NIST) Report 7765*.
- Biswas, Mrinmay. 1986. "Precast Bridge Deck Design Systems." *PCI Journal* 31 (2): 40–94.
- Boresi, Arthur P., and K. P. Chong. 2000. *Elasticity in Engineering Mechanics*. 2nd ed. New York: Wiley.
- Culmo, Michael P. 2009. "Connection Details for Prefabricated Bridge Elements and Systems." Report No. FHWA-IF-09-010.
<http://www.fhwa.dot.gov/bridge/prefab/if09010/report.pdf>.
- De la Varga, I., Z. B. Haber, and B. A. Graybeal. 2018. "Enhancing Shrinkage Properties and Bond Performance of Prefabricated Bridge Deck Connection Grouts: Material and Component Testing." *Journal of Materials in Civil Engineering* 30 (4): 04018053.
[https://doi.org/10.1061/\(ASCE\)MT.1943-5533.0002235](https://doi.org/10.1061/(ASCE)MT.1943-5533.0002235).

- De la Varga, Igor, and Benjamin A Graybeal. 2015. "Dimensional Stability of Grout-Type Materials Used as Connections between Prefabricated Concrete Elements." *Journal of Materials in Civil Engineering* 1107 (9): 1–10. [https://doi.org/10.1061/\(ASCE\)MT.1943-5533.0001212](https://doi.org/10.1061/(ASCE)MT.1943-5533.0001212).
- De La Varga, Igor, and Benjamin A. Graybeal. 2016. "Dimensional Stability of Grout-Like Materials Used in Field-Cast Connections." FHWA-HRT-16-080.
- De La Varga, Igor, Zachary B. Haber, and Benjamin Graybeal. 2017. "Bond of Field-Cast Grouts to Precast Concrete Elements." FHWA-HRT-16-081.
- De La Varga, Igor, Jose F. Munoz, D. P. Bentz, P.E. Stutzman, and B. A. Graybeal. 2017. "Grout-Concrete Interface Bond Performance: Effect of the Interface Moisture on the Tensile Bond Strength and Grout Microstructure." *Cement and Concrete Composites*, submitted.
- Graybeal, Benjamin A. 2006. "Material Property Characterization of Ultra-High Performance Concrete, FHWA-HRT-06-103." August. Washington DC.
- Graybeal, Benjamin A. 2010. "Behavior of Field-Cast Ultra-High Performance Concrete Bridge Deck Connections Under Cyclic and Static Structural Loading." FHWA-HRT-11-023.
- . 2014. "Compression Testing of Ultra-High-Performance Concrete." *Advances in Civil Engineering Materials*, November, 20140027. <https://doi.org/10.1520/ACEM20140027>.
- Gulyas, Robert J., Gregory J. Wirthlin, and Jeffrey T. Champa. 1995. "Evaluation of Keyway Grout Test Methods for Precast Concrete Bridges." *PCI Journal*, no. January-February: 44–50.
- Haber, Z. B., and B. A. Graybeal. 2018. "Lap-Spliced Rebar Connections with UHPC Closures." *Journal of Bridge Engineering*.
- Harris, Devin K., Miguel A. Carbonell Muñoz, Amir Gheitasi, Theresa M. Ahlborn, and Sarah V. Rush. 2014. "The Challenges Related to Interface Bond Characterization of Ultra-High-Performance Concrete With Implications for Bridge Rehabilitation Practices." *Advances in Civil Engineering Materials* 4 (2): 20140034. <https://doi.org/10.1520/ACEM20140034>.
- Issa, Mohsen A., C. L. Ribeiro do Valle, H. A. Abdalla, and Mahmoud A. Issa. 2003. "Performance of Transverse Joint Grout Materials in Full-Depth Precast Concrete Bridge Deck Systems." *PCI Journal* 48 (4): 92–103.
- Issa, Mohsen A., A. A. Yousif, Mahmoud A. Issa, I. I. Kaspar, and S. Y. Khayyat. 1995. "Field Performance of Full Depth Precast Concrete Panels in Bridge Deck Rehabilitation." *PCI Journal* 40 (3): 82–108.
- Kropp, Peter, Edward Milinski, and Martin Gutzwiller. 1975. "Use of Precast-Prestressed Concrete for Bridge Decks: Final Report." FHWA/IN/JHRP-75/15, 1 (12) Pt 2. West Lafayette, IN: Purdue University. <https://doi.org/10.5703/1288284314556>.
- la Varga, Igor De, and Benjamin A. Graybeal. 2015. "Dimensional Stability of Grout-Type Materials Used as Connections between Prefabricated Concrete Elements." *Journal of Materials in Civil Engineering* 1107 (9): 1–10. [https://doi.org/10.1061/\(ASCE\)MT.1943-5533.0001212](https://doi.org/10.1061/(ASCE)MT.1943-5533.0001212).
- . 2016. "Dimensional Stability of Grout-Type Materials Used as Connections between Prefabricated Concrete Elements. FHWA-HRT-16-008." McLean, VA.
- Li, Lungui, Zhongguo (John) Ma, Mary E. Griffey, and Ralph G. Oesterle. 2010. "Improved Longitudinal Joint Details in Decked Bulb Tees for Accelerated Bridge Construction:

- Concept Development.” *Journal of Bridge Engineering* 15 (3): 327–36.
[https://doi.org/10.1061/\(ASCE\)BE.1943-5592.0000067](https://doi.org/10.1061/(ASCE)BE.1943-5592.0000067).
- M. Keith Thompson, Antonio Ledesma, James O. Jirsa, and John E. Breen. 2006. “Lap Splices Anchored by Headed Bars.” *ACI Structural Journal* 103 (2): 271–79.
- Martin, L. D., and A. E. Osborn. 1983. “Connections for Modular Precast Concrete Bridge Decks.” Final Report FHWA-RD-82-106.
- Momayez, A., M.R. Ehsani, A.A. Ramezaniapour, and H. Rajaie. 2005. “Comparison of Methods for Evaluating Bond Strength between Concrete Substrate and Repair Materials.” *Cement and Concrete Research* 35 (4): 748–57.
<https://doi.org/10.1016/j.cemconres.2004.05.027>.
- Nilson, Arthur H., David Darwin, and Charles W. Dolan. 2010. *Design of Concrete Structures*. 14th ed. Boston: McGraw-Hill Higher Education.
- RILEM Report 41. 2007. “Internal Curing of Concrete (Edited by K. Kovler and O. Jensen).”
- Sagan, V. E., P. Gergely, and R. N. White. 1991. “Behavior and Design of Noncontact Lap Splices Subjected to Repeated Inelastic Tensile Loading.” *ACI Structural Journal* 88 (4): 420–31.
- Santos, Pedro M.D., Eduardo N.B.S. Júlio, and Vítor D. Silva. 2007. “Correlation between Concrete-to-Concrete Bond Strength and the Roughness of the Substrate Surface.” *Construction and Building Materials* 21 (8): 1688–95.
<https://doi.org/10.1016/j.conbuildmat.2006.05.044>.
- Stanton, J. F., and Alan H. Mattock. 1986. *Load Distribution and Connection Design for Precast Stemmed Multibeam Bridge Superstructures*. National Cooperative Highway Research Program Report 287. Washington, D.C: Transportation Research Board, National Research Council.
- Sullivan, Sean R. 2007. “Construction and Behavior of Precast Bridge Deck Panel Systems.” Dissertation, Blacksburg, Virginia: Virginia Polytechnic Institute and State University.
- Swenty, Matthew K., and Benjamin A. Graybeal. 2013. “Material Characterization of Field-Cast Connection Grouts.” NTIS No. PB2013-130231. FHWA.
- Yuan, Jiqui, and Benjamin Graybeal. 2015. “Bond of Reinforcement in Ultra-High-Performance Concrete.” *ACI Structural Journal* 112 (6). <https://doi.org/10.14359/51687912>.
- Zhu, Peng, and Zhongguo John Ma. 2010. “Selection of Durable Closure Pour Materials for Accelerated Bridge Construction.” *Journal of Bridge Engineering* 15 (6): 695–704.
[https://doi.org/10.1061/\(ASCE\)BE.1943-5592.0000106](https://doi.org/10.1061/(ASCE)BE.1943-5592.0000106).
- Zhu, Peng, Zhongguo John Ma, Qi Cao, and Catherine E. French. 2012. “Fatigue Evaluation of Transverse U-Bar Joint Details for Accelerated Bridge Construction.” *Journal of Bridge Engineering* 17 (2): 191–200. [https://doi.org/10.1061/\(ASCE\)BE.1943-5592.0000257](https://doi.org/10.1061/(ASCE)BE.1943-5592.0000257).
- Zhu, Peng, Zhongguo John Ma, and Catherine E. French. 2012. “Fatigue Evaluation of Longitudinal U-Bar Joint Details for Accelerated Bridge Construction.” *Journal of Bridge Engineering* 17 (2): 201–10. [https://doi.org/10.1061/\(ASCE\)BE.1943-5592.0000255](https://doi.org/10.1061/(ASCE)BE.1943-5592.0000255).

This page was intentionally left blank

